Protein Condensates with Appropriate Material Properties Regulate Tumorigenesis

Wei Li[1,2], Jing Hu[1,2], Bi Shi[1], and Hao Jiang[1,3]

[1]Department of Biochemistry and Molecular Genetics, University of Alabama at Birmingham School of Medicine

[1]Department of Biochemistry and Molecular Genetics, University of Virginia School of Medicine

[2]These authors contributed equally

[3]Corresponding author and Lead Contact

Hao Jiang
Department of Biochemistry and Molecular Genetics
University of Virginia School of Medicine
PO Box 800733
1340 JPA, Pinn Hall Room 6017
Charlottesville, VA 22908
Phone: (434) 924-2112
Email: hj8d@virginia.edu

The authors have declared that no conflict of interest exists.

Keywords:
Phase separation; biomolecular condensation; material properties; gene regulation; RNA splicing; cancer

ABSTRACT

It remains unknown if material properties of biomolecular condensates regulate cancer. Here we show that AKAP95, a nuclear protein that regulates transcription and RNA splicing, plays an important role in tumorigenesis by promoting cancer cell growth and suppressing oncogene-induced senescence. We show that AKAP95 forms phase-separated and liquid-like condensates in vitro and in nucleus. Mutations of key residues to different amino acids perturb AKAP95 condensation in opposite directions. Importantly, the activity of AKAP95 in splice regulation is abolished by disruption of condensation, significantly impaired by hardening of condensates, and regained by substituting its condensation-mediating region with other condensation-mediating regions from irrelevant proteins. Moreover, the abilities of AKAP95 in regulating gene expression and promoting tumorigenesis require AKAP95 to form condensates with proper liquidity and dynamicity. These results thus link phase separation to tumorigenesis and uncover an important role of appropriate material properties of protein condensates in gene regulation and cancer.

INTRODUCTION

Phase separation or biomolecular condensation is now recognized as a fundamental principle in organizing cellular contents and biochemical reactions by driving the formation of many different membraneless micro-compartments in the cellular space (Courchaine et al., 2016; Hyman et al., 2014; Shin and Brangwynne, 2017). Phase separation often involves proteins with large intrinsically disordered regions (IDRs) and multivalent interactions of proteins and nucleic acids (Banani et al., 2017; Hyman et al., 2014; Shin and Brangwynne, 2017). Depending on the strength and stability of the underlying intermolecular interactions and range of molecular order, biomolecular condensates can adopt a broad and continuous spectrum of material properties, from highly dynamic and liquid-like droplets to less fluid gels with reduced dynamicity and solid amyloid aggregates (Alberti et al., 2019; Banani et al., 2017; Kato et al., 2012; Patel et al., 2015). It is increasingly evident that different proteins adopt appropriate material properties of the condensates to meet particular biological needs. A dynamic and liquid-like property is anticipated to be more compatible with active regulatory functions in biology, whereas a non-dynamic and solid-like property befits the functionalities of certain other assemblies either as bioreactive gels or to switch off bioreactions (Woodruff et al., 2018). Liquid droplets in vitro are often observed to gradually harden or mature over time to adopt a more solid-like state, with poorly understood molecular mechanisms (Banani et al., 2017). Importantly, pathogenic mutations have been shown to facilitate high-degree aggregation as the underlying mechanism for many degenerative diseases (Kim et al., 2013; Molliex et al., 2015; Patel et al., 2015; Ramaswami et al., 2013), underscoring the importance of understanding the role of material properties of biomolecular condensates in cellular processes. However, our understanding of a role of phase separation in other types of major disease, such as cancer, is surprisingly limited. Moreover, it is entirely unclear whether quantitative changes in the degree of fluidity and dynamicity of the biomolecular condensates can significantly impact the outcome of cancer.

Cancer arises from genetic alterations that almost always elicit major reprogramming of the cellular gene expression profiles at the levels of transcription (Bradner et al., 2017) and sometimes RNA splicing (David and Manley, 2010). These changes in gene expression are often the major driving force for tumorigenesis. Moreover, compared to normal cells, cancer cells can also become exceptionally dependent on the altered gene expression programs to meet the high demand of proliferation and combating tumor-suppressive responses (Luo et al., 2009).

Phase separation has been recently proposed to underlie the spatial and temporal regulation of gene expression (Hnisz et al., 2017). Transcription involves various levels of condensation of proteins including RNA polymerase II (Kwon et al., 2013; Lu et al., 2018), transcription factors (Boija et al., 2018; Chong et al., 2018), and coactivators (Sabari et al., 2018). Aggregation of a splicing regulator into amyloid-like structure was linked to RNA splice activation (Ying et al., 2017), and higher-order assemblies of splicing regulators are thought to expand their gene regulatory capacity in mammals (Gueroussov et al., 2017). The aggregation and phase separation property of FUS, EWSR1, and TAF15 (Kwon et al., 2013; Schwartz et al., 2015) are implicated in the oncogenic potentials of their translocated products through transcriptional regulation. In particular, the aggregation-capable domain in the EWS-FLIi fusion protein recruits chromatin-remodeling factors to establish oncogenic gene expression programs in Ewing sarcoma (Boulay et al., 2017). All of these studies associate the condensate state of gene modulators with their activities in transcription or splicing. However, since the condensate state is not one single physical state but has a gradient of varying physical properties, an important question remains unanswered whether the different levels of liquidity and molecular dynamics in the continuum of material properties functionally impact the biochemical outcomes of gene expression. More specifically, are regulatory proteins in hardened condensates still as active in regulating gene expression?

AKAP95 (also called AKAP8) (Eide et al., 1998) is a nuclear member of the A-kinase anchoring proteins family, which bind to protein kinase A and act to integrate signaling pathways in cells (Wong and Scott, 2004). In addition, AKAP95 joins HA95 and ZNF326 in the AKAP95 family that share the common AKAP95 subtype of the zinc finger domains (Castello et al., 2012). AKAP95 is implicated in human diseases including abnormal head growth and autism (Nebel et al., 2015), prenatal oral clefts (Cao and Li, 2016), and cancer (Chen et al., 2016; Liu et al., 2015; Qi et al., 2015). AKAP95 is known to associate with chromatin (Eide et al., 2002; Li et al., 2006) and nuclear matrix (Akileswaran et al., 2001), but its exact location in nucleus is unclear. AKAP95 has several different activities (Eide et al., 2003; Jungmann and Kiryukhina, 2005; Li et al., 2006), including mediation of chromatin condensation (Bomar et al., 2002; Collas et al., 1999) and recruitment of HDACs to mitotic chromosomes (Li et al., 2006).

We have previously identified AKAP95 as a novel factor that integrates regulation of transcription and RNA splicing (Hu et al., 2016; Jiang et al., 2013). Via its N-terminal (1-100 residues) region, AKAP95 binds to the DPY30 subunit of the MLL family H3K4 methyltransferase complexes and enhances the in vitro methylation activity of MLL2 complex on chromatin (Jiang et al., 2013).

AKAP95 overexpression strongly co-activates the expression of a chromatin reporter likely at the transcriptional level, and this effect requires both the 1-100 region and the zinc finger domains (ZFs) (Jiang et al., 2013). Using an unbiased proteomic approach, we later found that AKAP95, all through its N-terminal 1-100 region, mainly associates with many factors known to be involved in RNA processing and transcription including a subset of hnRNP proteins and RNA Polymerase II (Hu et al., 2016). We have then shown that AKAP95 is important for efficient splicing of a minigene reporter in cells, and is directly involved in splice regulation in a cell-free system. AKAP95 directly and preferentially binds to both ends of proximal intronic regions on pre-mRNAs in human transcriptome, and this binding requires its zinc finger domains. By selectively coordinating with hnRNP H/F and U physically and functionally, AKAP95 modulates alternative splicing of many transcripts in the human transcriptome. As AKAP95 can self-interact largely through its N-terminal 1-210 region, we proposed that AKAP95 may help bring splice junctions to close proximity (Hu et al., 2016). However, like most other protein factors known to regulate pre-mRNA splicing (Fu and Ares, 2014), the fundamental molecular properties that mediate the activity of AKAP95 in splice regulation are unclear.

Here we show that, while dispensable for normal cell growth, AKAP95 plays an important role for tumorigenesis through promoting cell proliferation and overcoming the senescence barrier to cancer by regulating gene expression, including pre-mRNA splicing. In searching for a fundamental property of AKAP95 in regulating splicing, we discovered that AKAP95 undergoes phase-separated condensation with liquid-like property in vitro and in cells. By mutagenesis of key amino acids and creating chimeric proteins, we show that the condensation ability is essential for AKAP95 in splice regulation. Surprisingly, we identified a condensation-enhancing mutation that also significantly impairs the splicing activity, and we then show that this mutation hardens condensates and reduces molecular dynamics in vitro and in cell nucleus. We provide evidence that perturbing the condensation propensity of AKAP95 and driving the material properties out of a proper window of liquidity and dynamicity have profound impact on its biochemical activities in regulating gene expression and biological activities in controlling tumorigenesis, thereby linking the physical properties of protein condensates to cancer control.

RESULTS

AKAP95 is associated with human cancers and regulates cancer cell growth

Consistent with significant enrichment of cell cycle-related transcripts in AKAP95 targets (Hu et al., 2016), AKAP95 was shown to be overexpressed in ovarian (Liu et al., 2015) and rectal cancer tissues (Qi et al., 2015) together with some cyclin genes. Our analyses show that *AKAP95* is frequently amplified across a large variety of human cancers (**Figure 1A**). In more detail, our analyses show that AKAP95 is often overexpressed at the mRNA level in cancers including triple negative breast cancer (TNBC) (**Figure 1B**) and uterine corpus endometrioid carcinoma (**Figure S1A**). Moreover, these alterations (mainly amplifications and mRNA upregulation) are significantly correlated with poorer survival of both types of cancer patients (**Figures 1B and S1A**). These results indicate an association of AKAP95 with human cancer.

We then sought a functional role of AKAP95 in cancer. Considering its association with TNBC, we achieved efficient knockdown (KD) of AKAP95 by two different AKAP95 shRNAs in MDA-MB-231 cells, a human TNBC cell line (**Figure 1C**). AKAP95 KD markedly inhibited their growth (**Figure 1C**). In addition, AKAP95 KD significantly reduced cell proliferation and increased apoptosis (**Figure S1B**). Moreover, after transplanted into immuno-deficient mice, the AKAP95-KD TNBC cells gave rise to tumors that were significantly smaller than those from the control cells (**Figure 1D**), indicating that AKAP95 is important for in vivo tumorigenesis. The requirement of AKAP95 in breast cancer cell growth is not limited to TNBC, as its KD also significantly reduced the growth of MCF-7 cells, a breast cancer cell line positive for estrogen receptors (**Figure S1C**). To rule out off-target effects, we also restored AKAP95 expression in control and AKAP95-KD TNBC cells (**Figure S1D**). We found that restoring AKAP95 expression rescued the growth of the KD cells, and extra expression of AKAP95 in control cells also significantly enhanced the growth (**Figure S1D**).

AKAP95 regulates gene expression, including direct regulation of RNA splicing, in cancer cells

As AKAP95 is known to regulate gene expression including RNA splicing, we performed RNA-seq to analyze the impact of AKAP95 KD and rescue on global gene expression (**Figure 1E and Table S1, tab 1),** as well as global alternative splicing (with the focus on alternative exon inclusion events) (**Figure 1G and Table S1, tab 2**), in TNBC cells. As shown by Gene Set Enrichment Analysis (GSEA), pathways in TGF-β signaling, G2M checkpoint, and E2F targets were significantly enriched in genes downregulated by KD, and pathways in inflammatory response and apoptosis were significantly enriched in genes upregulated by KD (**Figures 1F and S1E**). These results are consistent with the reduction in cell proliferation and increase in apoptosis upon

AKAP95 KD. Our global splicing analysis showed that AKAP95 KD induced change of thousands of alternative splicing events as indicated by changes in percent-spliced-in (PSI) values, including 809 events in reduction (PSI reduced) and 1273 events in increase (PSI increased) of exon inclusion (**Figure 1G and Table S1, tab 2**). Gene ontology analysis showed that the genes with increased or suppressed exon inclusion upon AKAP95 KD were both significantly enriched in pathways including DNA damage and repair, cell division, mitochondrion, and transcription, although the detailed ranking differed between these two clusters of genes (**Figure 1H**).

We then sought to focus on a few specific targets of AKAP95 in cancer cells. Prompted by both the global expression analyses and the reduction of cell proliferation upon AKAP95 KD, we examined the expression of a panel of cyclin genes, and found that *CCNA2* (encoding Cyclin A2) expression was selectively downregulated at mRNA and protein levels upon AKAP95 KD (**Figure S1F**). We then show that those TNBC patients with *AKAP95* overexpression also often overexpress *CCNA2* at the mRNA level, and *CCNA2* and *AKAP95* mRNA levels exhibit a quantitative correlation throughout the TNBC patient samples (**Figure S1G**). Depletion of CCNA2 significantly inhibited growth of TNBC cells (**Figure S1H**). Moreover, CCNA2 restoration in the AKAP95-KD TNBC cells significantly though partially rescued their growth (**Figure S1I**). These results suggest that AKAP95 promotes TNBC growth partially through promoting the expression of *CCNA2*.

Our RIP-seq results indicate that AKAP95 binds to intron 1 of *CCNA2* pre-mRNA in a zinc finger domain-dependent manner (**Figure S1J**), suggesting that AKAP95 may directly regulate the splicing of this intron. Indeed, mRNA-seq results indicated that, compared to the average junction level of all neighboring exons, the junction level of exons 1 and 2 was reduced upon AKAP95 KD (**Figure S1K**). Our analysis shows that the *CCNA2* transcript that retains intron 1 will generate a premature termination codon (**Figure S1K**), which is known to activate the nonsense-mediated decay (NMD) pathway, an RNA surveillance mechanism, and consequently degrade the transcript (Hug et al., 2016). Consistent with this hypothesis, we were able to directly detect accumulation of intron 1-retained *CCNA2* transcript following AKAP95 KD in cells when nonsense-mediated decay (NMD) was blocked by either cycloheximide or depletion of UPF1 or BTZ, key proteins in NMD (Hug et al., 2016) (**Figure S1L-S1N**). These results strongly suggest that AKAP95 directly facilitates the correct splicing of *CCNA2* to ensure its sufficient production that contributes to cancer cell growth.

We also studied how AKAP95 regulated expression of key components of the TGF-β signaling pathway, a well-known player in tumorigenesis (David and Massague, 2018) and the top enriched pathway downregulated by AKAP95 KD in TNBC cells (**Figures 1F and S1E**). A total of 16 genes in this pathway was found to be downregulated upon AKAP95 KD and then upregulated upon restoration of AKAP95 expression in the TNBC cells (**Figures S1O**). Detailed examination of their expression showed that SMAD6 was substantially downregulated by AKAP95 KD and rescued by AKAP95 re-expression (**Figures S1O**). TGF-β signaling pathway has both tumor-suppressing and tumor-promoting functions depending on cellular context (David and Massague, 2018). SMAD6 (Imamura et al., 1997) and SMAD7 negatively regulate the TGF-β signaling pathway (David and Massague, 2018) and have been reported to promote certain tumorigenesis (Jeon et al., 2008; Jiao et al., 2018). We found that AKAP95 bound to the intronic region between exons 1 and 2 of the *SMAD6* pre-mRNA (**Figure 1I**). Joining of exons 1 and 2, but not of exons 2 and 3, was abolished by AKAP95 KD and modestly rescued by the restored expression of AKAP95 (**Figure 1J**). As a translation termination codon is in the intronic region between exons 1 and 2 (**Figure 1J**), we reason that, similar to the *CCNA2* regulation by AKAP95, inefficient splicing of this intron upon AKAP95 KD may activate NMD to reduce *SMAD6* expression and contribute to the cancer cell growth arrest.

In addition to *CCNA2* and *SMAD6*, the direct regulation of splicing by AKAP95 can be shown on two other exemplary genes *RPUSD3* and *MMP1K*, where AKAP95 was found to strongly bind to both intronic regions flanking an exon (**Figure S1P**) that was more included upon AKAP95 KD and more excluded upon restoration of AKAP95 expression (**Figure S1Q**). Taken together, these results suggest that AKAP95 regulates cancer cell growth partially through controlling the splicing and expression of many target genes including *CCNA2* and *SMAD6*.

Akap95 is dispensable for normal cell growth but required for overcoming the senescence barrier to cancer cells

To better understand the role of AKAP95 in cancer, we generated an *Akap95* knockout (KO) mouse model using embryonic stem cells harboring an engineered *Akap95* Knockout-first allele (**Figure S2A**). The *Akap95*$^{-/-}$ mice were born with expected Mendelian ratio, and had no overt phenotypes for at least 1 year and half to date, indicating that Akap95 is not essential for normal mouse development or physiology. The detailed description of the physiology and tumorigenesis of these mice will be reported elsewhere. We studied primary mouse embryonic fibroblasts (MEFs) derived from wild type (WT), *Akap95*$^{+/-}$ (Het), and *Akap95*$^{-/-}$ (KO) embryos, and confirmed that Akap95 was lost at both genomic and protein levels in the KO MEFs (**Figure S2B**). The Het and KO MEFs showed the same growth rate in culture (**Figure 2A**) and very similar morphology (**Figures 2E and S2D**), indicating that Akap95 is dispensable for normal cell growth.

We then sought to examine the impact of Akap95 loss on transformation of primary MEFs by two potent oncogenes, *H-RAS*^{G12V} and c-*MYC* (*MYC*). We confirmed that the expression of neither oncogene was affected by Akap95 loss (**Figure 2B**). However, Akap95 loss in these oncogene-transduced MEFs significantly impeded their anchorage-independent colony formation ability in soft agar (**Figure 2C**) as well as their in vivo tumorigenicity upon transplant into immune-deficient animal recipients (**Figure 2D**), indicating a requirement of Akap95 for oncogene-induced transformation of normal cells to cancer cells.

To gain deeper and more focused understanding of the role of Akap95 in tumorigenesis, we transduced the MEFs with MYC alone, and showed that MYC expression was not significantly affected by Akap95 loss (**Figures 2E, top left**). The WT MEFs exhibited substantial change in morphology following MYC transduction, suggesting that they were well on the path to immortalization. In contrast, all of the KO MEFs showed morphology largely similar to that before MYC transduction, suggesting a possible block on their path to MYC-induced immortalization (**Figures 2E and S2D**).

We then performed RNA-seq analysis for the MYC-transduced Het and KO MEFs (**Figure 2F and Table S2**). As shown by gene ontology analysis (**Figure 2G**), in the MYC-transduced cells, nuclear pathways in cell proliferation and DNA damage repair are mostly enriched in genes downregulated upon Akap95 loss, while extracellular pathways in inflammatory response are mostly enriched in genes upregulated upon Akap95 loss. We further showed that the alteration of the global gene expression profile could be largely reverted by introduction of the human WT AKAP95 into the KO MEFs (**Figure S2E and Table S2, tab 2**). The upregulation of the secreted inflammatory molecules in the MYC-transduced KO MEFs very well fits the so called senescence-associated secretory phenotype (SASP) (Coppe et al., 2008; Kuilman and Peeper, 2009), which refers to the activation of a unique form of immune surveillance in senescent cells to regulate the tissue microenvironment and contribute to the elimination of malignant cells undergoing senescence in an organism. Indeed, our GSEA showed that, while pathways in E2F targets, G2M checkpoint, and MYC targets were among top genes significantly enriched in genes downregulated by Akap95 loss in the presence of MYC activation, pathways in inflammatory response, senescence (and SASP specifically), and apoptosis were significantly enriched in genes upregulated by Akap95 loss in the presence of MYC activation (**Figures 2H and S2C**). Moreover, compared to the WT and Het MEFs, the KO MEFs showed significantly elevated levels of SA-beta-galactose (**Figures 2E and S2D**), a well-established indicator of cellular senescence. We further showed that the increase of senescence was suppressed by introduction of the human WT AKAP95 into the KO MEFs, but not by expression of AKAP95 (101-692), which lacks the N-terminal region that binds to many regulatory factors for transcription and RNA-processing (**Figure 2I**). As cellular senescence is a potent barrier to tumorigenesis, these results indicate that Akap95 is required for removing the senescence barrier on the path towards oncogene-induced cellular transformation and tumorigenesis.

Through RT-qPCR, we showed that, in the Het MEFs, MYC transduction significantly upregulated the expression of *Akap95* and *Ccna2*. In the KO MEFs, however, MYC completely lost its activity in upregulating *Ccna2* (**Figure 2J**). Together with the significant enrichment of MYC targets in genes downregulated in the MYC-transduced KO MEFs compared to the MYC-transduced Het MEFs (**Figures 2H and S2C**), these results suggest that MYC promotes the expression of *Akap95* to functionally coordinate the expression of many important targets of MYC including *Ccna2*.

Also using our RNA-seq results, our global splicing analysis showed that, in the MYC-transduced cells, Akap95 loss resulted in 216 events in reduction and 253 events in increase of alternative exon inclusion (**Figure S2F and Table S2, tab 3**). these genes were also significantly enriched in pathways including DNA damage and repair, cell division, mitochondrion, and transcription (**Figure S2F**), very similar to the affected genes in the TNBC cells.

Together with our results from human cancers, these data demonstrate that, in the event of oncogenic assault (at least for MYC), the activity of AKAP95 in regulating gene expression is required for maintaining or promoting cell proliferation and meanwhile suppressing stress response such as cellular senescence, both sides crucial for making a successful cancer cell (**Figure 2K**).

AKAP95 forms liquid-like and phase-separated condensates in vitro

What is the molecular nature of AKAP95 that confers its biochemical activities in gene regulation and biological functions in promoting cancer cell growth and combating oncogene-induced senescence? The initial clue came from our observation of either endogenous AKAP95 or tagged

AKAP95 truncation mutants forming dimers that were resistant to the strongly denaturing condition of boiling and SDS-PAGE (**Figures 3A and S3A)**. We think this reflects an extraordinary propensity of AKAP95 in self-aggregation, and this property may shed light on its biochemical and biological activities.

AKAP95 is predicted to be intrinsically disordered throughout the protein except the N-terminal (1-100) and the two zinc finger domains (**Figure 3B**), and also has a prion-like domain (not predicted to be disordered) at the very N-terminal region (**Figure S3B**). The SDS-resistant dimerization did not require the prion-like domain in the 1-100 region or any of the zinc finger domains, and was sufficiently mediated by the 1-210 region of AKAP95 (**Figure S3A**). We fused AKAP95 N-terminal (1-340) and C-terminal (306-692) regions individually to maltose-binding protein (MBP) to enhance yield and solubility. A tobacco etch virus (TEV) protease cleavage sequence was inserted between MBP and AKAP95. After expression and purification from bacteria (**Figure S3C**), these fusion proteins appeared homogeneous and clear in solutions (**Figure 3C, left up**). Upon cleavage of the MBP tag, however, AKAP95 (1-340), but not (306-692), exhibited remarkable turbidity with elevated light absorbance at 600 nm (**Figure 3C, left bottom**), suggesting an aggregation property of 1-340. We then further divided 1-340 into 1-100, 101-210, and 211-340 sub-regions, and individually fused them to MBP. Upon MBP cleavage, only 101-210 exhibited remarkable turbidity and increase in OD600 (**Figure 3C, middle**). Moreover, deletion of 101-210 within the 1-340 region greatly reduced, though did not abolish, the ability to develop turbidity (**Figure 3C, right**). These results indicated that 101-210 is sufficient and largely necessary for the aggregation of AKAP95, and are consistent with this region mediating AKAP95 self-interaction (Hu et al., 2016).

AKAP95 (101-210) formed micron-sized droplets that had nearly spherical shape, freely moved in solution, fell onto glass coverslip, show marked increase in size in the presence of crowding agent, and occasionally experienced fusion (**Figures 3D-3F, and S3D, and Movie S1**). To confirm the identity of these droplets, we fluorescently label MBP-(101-210) by conjugation to Oregon Green and confirmed the fluorescent signal of these droplets (**Figures 3D** and shown later in **Figure 5C**), after finding out that GFP fusion often interferes with droplet formation of the purified fusion protein (data not shown). We showed that the droplet formation by 101-210 was promoted by increasing protein concentration and inhibited by increasing salt concentration (shown later in **Figure 6B**). Moreover, the pre-formed condensates in low salt condition were rapidly dissolved by elevated salt concentration and could re-form rapidly upon dilution to lower salt condition (even at equally diluted protein concentration) (**Figures 3D**), indicating their high reversibility and critical dependence on electrostatic interactions. The re-formed condensates upon salt dilution appeared to have undergone modest aggregation (**Figures 3D**). As measured by Fluorescence Recovery After Photobleaching (FRAP) assays, molecules in the droplets were mobile as they could rapidly though partially recover after photobleach (shown later in **Figure 6E**). We also demonstrated that the purified full-length AKAP95 was able to form liquid-like droplets in a physiological salt condition (**Figure 3G**). These results indicate that AKAP95 undergoes condensation in vitro and its 101-210 region confers the liquid-like property of AKAP95 condensates.

AKAP95 forms dynamic liquid-like droplets in cell nucleus and its dynamics is regulated by its binding factors

We next determined if AKAP95 forms liquid-like droplets in cells. By immunofluorescence assay, we showed the punctate distribution of endogenous AKAP95 in nuclei of human cancer cell lines as well as primary MEFs (**Figure 4A**). Following transfection into living cells, AKAP95-GFP fusion formed nuclear bodies that were mostly near spherical shape but could also be of various shapes (**Figure 4B and 4D**). These foci increased in size and decreased in number over time (**Figure 4B**), likely due in part to merging. Moreover, when cells were treated with a panel of different aliphatic alcohols, the endogenous AKAP95 foci were specifically and rapidly dissolved by 1,6-hexanediol but not other aliphatic alcohols (**Figure 4C**). As 1,6-hexanediol was shown to disrupt liquid-like assembly but not the solid-like fibers of FUS (Kroschwald et al., 2017), this result further supports a liquid-like property of the AKAP95 assembly in the cell nucleus.

We also characterized the AKAP95 (101-692) mutant, which misses the N-terminal region responsible for interacting with proteins factors in transcription and RNA processing, and the AKAP95 ($ZF^{C\text{-}S}$) mutant, which had the key Cysteine residues mutated to Serine in both zinc finger domains and thus loses ability in binding to RNAs (Hu et al., 2016). When expressed at the similar level as the WT (**Figure S4A**), both of these mutants also formed nuclear droplets (**Figure 4D**). Interestingly, the $ZF^{C\text{-}S}$ mutant foci appeared to be closer to a perfect spherical shape than the WT and 101-692 mutant, suggesting that RNAs tethered to the zinc fingers on AKAP95 somehow restrict the free distribution of AKAP95 molecules that otherwise would take up a spherical shape influenced by the cohesive forces of the surface layer. Moreover, while we did not observe rapid fusion of the WT foci in the nucleus, we occasionally observed fusion of the $ZF^{C\text{-}S}$ mutant foci in the nucleus over a time scale of tens of seconds (**Figure 4E and Movie S2**), further suggesting that RNA binding to the zinc finger domains restrains the mobility of the AKAP95 droplets in cells.

Upon photobleaching in the FRAP assays (**Figure 4F and 4G and Movie S3**), the fluorescence intensity of AKAP95 in the nucleus recovered with a characteristic half recovery time of 33.5 ± 1 s, indicating that AKAP95 rapidly exchanged into and out of the bodies. These results are consistent with a dynamic liquid-like property of the AKAP95 foci in the nucleus. Compared to the AKAP95 WT, both 101-692 and ZF^{C-S} mutants recovered significantly faster after photobleach without affecting the completeness of the recovery (**Figure 4G and Movie S3**). These results suggest that while association with protein factors (via the N-terminus) and with RNAs (via ZFs) are not essential for AKAP95 to phase separate in cells, they both slow down the molecular dynamics in the condensates and contribute to the longer residence time of AKAP95 in its nuclear bodies. The reduced half time of both mutants may contribute to their defective ability in gene regulation, in line with the correlation of a longer lifetime of RNA polymerase II cluster with increased mRNA synthesis (Cho et al., 2016). When fused to GFP and expressed at a similar level in cells (**Figure S5C**), the full-length AKAP95 formed foci in nucleus, but AKAP95 lacking 101-210 [Δ(101-210)] became largely diffuse in nucleus (**Figure 4H**). The same requirement of this region in both in vitro droplets and in vivo foci supports a similar nature of these assemblies in vitro and in vivo.

The exact localization of AKAP95 in nucleus is unclear. Considering its role in RNA splicing, we probed its localization relative to SRSF2, a splicing factor enriched in nuclear speckles (Spector and Lamond, 2011). Our immunofluorescence assay showed that AKAP95 substantially but incompletely overlapped with SRSF2 (**Figure S4B**), suggesting that AKAP95 is partially localized in nuclear speckles.

Tyrosine residues in 101-210 are required for AKAP95 phase separation

We then focused on 101-210, the major region mediating phase separation of AKAP95. Consistent with its intrinsic disorder, this region is enriched with amino acids with high flexibility and devoid of bulky amino acid residues (**Figures 5A** and **S5A**). Specifically, it is enriched with Arg (14 total), Gly (19), Phe (9), Asp (10), Ser (14), and Tyr (6), residues that are often enriched in other IDRs known to mediate phase separation. This region is also highly conserved between human and mouse, and variations are found in only 1/14 (1 out of 14) Arg (R to P), 2/10 Asp (both

D to E, conservative), 3/19 Gly (all G to S), but in 6/14 Ser residues. Phe and Tyr remain unchanged except for one case each of swapping (**Figure 5A**).

Considering the role of Tyr in several examples of aggregation or phase separation (Kwon et al., 2013; Pak et al., 2016; Wang et al., 2018), we mutated all six Tyr residues in the 101-210 region to Ala (YA), Ser (YS), or Phe (YF) residues and recombinantly expressed and purified them with similar quality (**Figure S5B**). We found that YA and YS, but not YF, abolished condensation, as shown by these four lines of evidence: **(i)** WT and YF, but not YA and YS, appeared turbid with elevated OD600 (YF > WT) upon MBP cleavage (**Figure 5B top and images**), **(ii)** WT and YF, but not YA and YS, were markedly depleted from supernatant phase after centrifugation (**Figure 5B bottom**), and **(iii)** Fluorescently labeled WT and YF, but not YA or YS, formed spherical and micrometer-sized droplets, and the YF droplets were less mobile on coverslip and appeared larger and/or brighter in fluorescence signals than the WT (**Figure 5C**). **(iv)** GFP fused to the full-length AKAP95 WT or YF, but not YA and YS, all expressed at the comparable level (**Figure S5C**), showed foci structures in the nucleus of cultured cells (**Figure 5D**). We also adjusted the expression level of each construct to the near endogenous level (**Figure S5D**), and showed that the full-length AKAP95 WT or YF was still able to form focal structures in the nucleus, though we saw increased portion of diffuse AKAP95 in the nucleus at this expression level compared to overexpression (**Figure S5E**). Importantly, YS and YA at this level of expression were also completely diffuse with no focal structure (**Figure S5E**). The same dependence on Tyr suggests that the AKAP95-GFP nuclear foci were not merely a result of overexpression.

Phase separation property is required for AKAP95 to regulate splicing

We then sought to determine if the 101-210 region is important for AKAP95's activity in regulating splicing using our established splice reporter assay that allows a convenient splicing readout (Hu et al., 2016). Unlike WT, AKAP95 Δ(101-210) overexpression at comparable levels failed to enhance the minigene splicing (**Figure S5F**). Deletion of 101-210 did not affect binding of AKAP95 to DDX5 or hnRNP M (**Figure S5G**), suggesting that it does not grossly disrupt the protein structure or interaction with key factors involved in splice regulation. Moreover, a more extensive truncation mutant, AKAP95 (387–692), is fully active in mediating chromatin condensation (Eide et al., 2002). These results suggest that 101-210, likely through its phase separation property, is important for AKAP95 to regulate minigene splicing.

We then sought to determine if the Tyr mutations that affect AKAP95 phase separation also affect its activity in splice regulation in our minigene splice reporter assay. AKAP95 KD significantly reduced the minigene splicing, and this could be rescued by restored expression of WT AKAP95 to a near endogenous level. However, AKAP95 mutants either lacking 101-210 or containing YA, or YS mutations within the 101-210 region all failed to show any rescue of the minigene splicing (**Figure 5E**). These results indicate that Tyr residues in 101-210 are crucial for AKAP95's activity in splice regulation, likely through their critical role in mediating AKAP95 phase separation.

We reasoned that if it is the phase separation property of the AKAP95 (102-210) that is crucial for this region to regulate splicing, we might be able to retain its splicing activity by replacing this region with a phase separation-capable region from an irrelevant protein. We thus generated four chimeric proteins in which the 101-210 region of AKAP95 was replaced by IDRs of comparable sizes from different proteins involved in cellular pathways largely unrelated to AKAP95 (**Figure 5F**). These IDRs were from human hnRNPA1 (186-320), yeast Pub1 (243-327), yeast Lsm4 (91-187), and yeast eIF4GII (13-97). Among these proteins, hnRNPA1, Pub1, and eIF4GII are known to be located in, and are involved in, stress granule assembly, while Lsm4 is known to play a role in P-body assembly in yeast (Lin et al., 2015). All of these IDRs have been previously characterized to undergo phase separation under appropriate conditions in vitro with varying physical properties (Lin et al., 2015). Among these IDRs, those of hnRNP A1 and eIF4GII formed liquid-like phase-separated droplets, while Lsm4 IDR tends to form fiber-like aggregates. Pub1 IDR forms phase separated-droplets when engineered to be coupled with an RNA-binding region and in the presence of RNA (Lin et al., 2015).

We first showed that all of these four chimeric proteins, when expressed at a level lower than the endogenous AKAP95 (**Figure S5H**), restored the punctate distribution in the cell nucleus that was lost upon deletion of 101-210 (**Figure 5G**). When tested for their ability in the splice reporter assay, these chimeric proteins that were expressed at sub-endogenous levels showed varying degree of ability in splice regulation (**Figure 5H**). AKAP95-hnRNPA1, -Pub1, and -Lsm4 chimeras all significantly rescued the reporter splicing, with AKAP95-hnRNPA1 showing almost the same splicing ability as AKAP95 WT. These results thus strongly support the functional role of the phase separation property in AKAP95's activity in splice regulation.

The appropriate material properties of AKAP95 condensates are important for splice regulation

As the YF mutations in 101-210 did not impair the condensation ability of 101-210 in vitro or foci formation of the full-length AKAP95 in the cell nucleus, we included the full-length AKAP95 with YF mutations within 101-210 in our splice reporter assays as a positive control. Surprisingly, this mutant also exhibited significantly reduced ability in minigene splicing compared to the WT, although it showed some improvement compared to the Δ(101-210), YA, or YS mutants (**Figure 5E**). We thus sought to further study the impact of the YF mutations on phase separation by using purified 101-210 (WT) and 101-210 (YF). We suspected that YF may condensate more strongly than WT, as we observed higher turbidity, less portion in the soluble fraction (**Figure 5B**) and larger or brighter droplets under microscope (**Figure 5C)** for 101-210 (YF) compared to 101-210 (WT). We then showed that, in kinetic assays, YF reached much higher maximum turbidity and also with faster rate than the WT (YF took less than half of the time compared to WT to reach half maximum level) (**Figure 6A**). We then determined the impact of protein and salt concentrations on their condensation. We found that, while the condensation of both protein fragments was promoted by increasing protein concentration and inhibited by increasing salt concentration, YF was able to condensate at a lower protein concentration and higher salt concentration than WT (**Figure 6B**). In 150 mM NaCl, the saturation concentration of WT was between 5-10 μM, whereas that of YF was between 0.5-2.5 μM (**Figure 6B**). Both of these results further strengthened the notion that YF has a higher propensity to condensate than WT.

Similar to 101-210 (WT) (**Figure 3D**), pre-formed 101-210 (YF) condensates in low salt condition were rapidly dissolved by elevated salt concentration and could re-form rapidly upon dilution to lower salt condition (**Figures S6A**), demonstrating the preserved high reversibility and dependence on electrostatic interactions. However, compared to 101-210 (WT), the re-formed 101-210 (YF) condensates upon salt dilution exhibited much more prominently aggregated morphology (**Figures S6A**). These results indicate that YF mutation does not fundamentally alter the molecular nature or driving force for the condensation, but may affect the material properties of the condensates. Also prompted by our observations that the YF droplets often appeared less mobile on coverslip, we further investigated the impact of YF mutation on the material properties of the condensates. We examined the 101-210 (WT) and 101-210 (YF) at the same concentration at varying time points after release from MBP fusion. 101-210 exhibited spherical droplet morphology at an early time point and maintained such morphology up to 2.5 hr. In contrast, the YF mutant exhibited near spherical morphology (larger than WT) at the early time point, but gradually developed into larger clusters with irregular morphology, suggesting a possible transition from a liquid-like state to a solid-like state (**Figure 6C**).

Hardened condensates are inevitably associated with reduced molecular mobility. We thus performed FRAP assays to study if the YF mutations render the AKAP95 condensates less dynamic. As condensates formed by 101-210 (YF) were larger than 101-210 (WT) and thus made it technically easier to achieve photobleach inside a condensate, we performed FRAP of fluorescently-labeled 101-210 (WT) or 101-210 (YF) that was spiked into the unlabeled 101-210 (YF) protein. We found that YF recovered at a much slower rate than WT so that it recovered to a significantly lower level than WT within our assay time (**Figure 6D**). This indicates a reduced mobility of the labeled YF molecules compared to WT in the same condensate matrix, and suggests that the molecular interactions between the labeled YF protein and the YF matrix are stronger than those between the labeled WT protein and the YF matrix.

We further performed FRAP of the fluorescently-labeled 101-210 (WT) in the droplets formed by either unlabeled 101-210 (WT) or unlabeled 101-210 (YF). We found that the labeled molecules recovered at a slower rate in the droplets formed by the YF than in the droplets by WT, though they were later able to reach the same recovery level (**Figure 6E**). These results suggest that different material properties of the polymer matrix affect the kinetics but not the final recovery level of the molecules inside matrix.

We then sought to study the impact of the YF mutations within 101-210 on the full-length AKAP95 in cells. FRAP assays showed that the fluorescent signal of YF-GFP foci recovered at a much slower rate than that of WT-GFP foci so that YF recovered to a significantly lower level than WT within our assay time (**Figure 6F**). This indicates that YF mutations within 101-210 significantly reduced the dynamics of the full-length AKAP95 in nucleus, and is fully consistent with the results of the purified protein fragments. Our results from both in vitro and in cells thus strongly suggest that YF mutation hardens the AKAP95 condensates and promotes a transition of the material property from a more liquid-like to a more solid-like state, and such transition is harmful for AKAP95's biological activity in splice regulation.

As protein aggregates can adopt highly ordered structure such as amyloid fibril or disordered and amorphous superstructure, we attempted to assess the structural feature of the AKAP95 YF mutant using thioflavin-T (ThT), a fluorescent dye that stains for amyloid fibril (Alberti et al., 2009). We found that, while the aggregates formed by the FUS protein showed substantial ThT staining, the aggregates formed by AKAP95 YF in the same condition did not show any ThT staining

(**Figure S6B**). While we cannot exclude the possibility that the lower extent/degree of AKAP95 YF aggregation (compared to the FUS in the same experiment) may not allow detectable ThT staining, these results suggest that purified AKAP95 YF may more likely adopt an amorphous aggregate structure rather than amyloid fibril.

AKAP95 condensation with appropriate material properties regulates tumorigenesis

We then sought to examine the impact of the Tyr mutations on the function of AKAP95 in gene expression and tumorigenesis, including its ability in promoting cancer cell growth and combating oncogene-induced senescence during cellular transformation.

We introduced constructs expressing AKAP95 WT or mutants containing YS or YF mutations in 101-210 into MDA-MB-231 cells that were depleted of AKAP95. These constructs were all expressed at a comparable level to each other, and also to the endogenous AKAP95 level in the control cells supplemented with empty vector (**Figure 7A**). We found that, compared to the empty vector control, re-introduction of AKAP95 WT significantly enhanced the colony formation ability of AKAP95-KD cells. In contrast, introduction of the YS mutant had no effect on the growth. Introduction of the YF mutant only modestly (and insignificantly) enhanced the colony formation ability compared to the empty vector, and the cells expressing the YF mutant formed significantly less colonies than those expressing the WT construct (**Figure 7B**). Similar effects were also seen on the growth of the AKAP95 KD cells. Introduction of the AKAP95 WT significantly enhanced the growth of the KD cells, but the YS mutant was completely inactive in promoting the growth, and the YF-expressing cells grew at a significantly slower rate than WT (**Figures 7C and S7A**).

We also examined expression of key genes involved in cell proliferation. We found that *SMAD6* expression was completely restored by re-introduction of AKAP95 WT into the KD cells. Introduction of the YS or YF mutant did not restore *SMAD6* expression, although YF slightly enhanced *SMAD6* expression (**Figure 7D**). We found a similar trend on *CCNA2* expression but our data did not show high consistency among biological repeats (**Figure S7B**). However, we did find that the splicing efficiency of the intronic region between exons 1 and 2 of the *CCNA2* pre-mRNA was significantly improved upon introduction of AKAP95 WT into the AKAP95-KD cells, but not at all by the YS mutant, and only weakly and insignificantly by the YF mutant (**Figure 7E**). Similarly, inclusion of the alternative exons in *RPUSD3* (**Figure 7F**) and *PPM1K* (**Figure S7C**) was both effectively rescued by introduction of WT, but not at all by YS, and only modestly by YF.

Compared to WT, YF showed significant and insignificant reduction in rescuing alternative splicing of *RPUSD3* and *PPM1K*, respectively.

We also introduced human AKAP95 WT or the YS or YF mutations into the MYC-transduced *Akap95* KO MEFs, and showed that these constructs were expressed at a comparable level to each other (**Figure 7G**). While introduction of WT significantly suppressed senescence of these MEFs, the YS and YF mutants both failed to suppress senescence (**Figure 7H**). As then shown by the global gene expression analysis (**Figure S7D and Table S2, tab 4**), compared to the vector control, introduction of the YS mutant resulted in minimal alterations of expression of genes that were affected by WT. On the other hand, introduction of the YF mutant elicited substantial alterations of many of those genes in a similar fashion to the alterations caused by WT, but the fold of alterations by YF appeared to be less and also a subset of genes did not show change in the way by WT. As we previously showed that genes promoting cell proliferation and survival were downregulated in the MYC-transduced KO MEFs and could be rescued by Introduction of human AKAP95 (**Figures 2F, 2G, S2C, S2E**), we performed RT-qPCR to examine the expression changes of several genes with established functions in these pathways and in promoting tumorigenesis. We found that these genes were significantly upregulated by introduction of AKAP95 WT, but not by YS or YF mutant (**Figure 7I**). We also found that the expression of certain SASP genes was suppressed by introduction of AKAP95 WT, but somewhat not as effectively by the YS or YF mutant (**Figure S7E**).

As then revealed by global splicing analysis (**Figure 7J and Table S2, tab 5**), introduction of WT resulted in 282 events in increase and 271 events in reduction of alternative exon inclusion. Similar to the effects on mRNA steady state levels, introduction of the YS mutant only minimally altered splicing events that were affected by WT, and the YF mutant substantially altered a large subset of splicing events that were affected by WT while leaving a subset of splicing events unaffected. This can be clearly seen on a few examples by the Sashimi plot showing the junction reads and the signal levels of the alternative exon, and further validated by RT-PCR of the isoforms that includes or skips the alternative exon (**Figures 7K, S7F, and S7G**). Introduction of WT into the MYC-transduced KO MEFs significantly increased the inclusion of the alternative exon on *Aamdc* (**Figure 7K**), *Zfp518b,* and *Numb* pre-mRNAs (**Figure S7F**) and significantly reduced the inclusion of the alternative exon on *Ttc21b* pre-mRNA (**Figure S7G**). Introduction of YS, however, did not elicit such changes. Introduction of YF showed varying degrees of effects on different genes, as it did not effect exon inclusion of *Numb*, very weakly and insignificantly effected *Aamdc* and *Ttc21b*, and significantly but modestly effected *Zfp518b*. Overall, the effects of YF on all of these genes were significantly lower than WT (**Figures 7K, S7F, and S7G**). These results on the splicing of endogenous genes are consistent with the effects of the mutants on the splice reporter.

Taken together, these results strongly suggest that the biological abilities of AKAP95 in promoting cancer cell growth and overcoming oncogene-induced senescence, and its biochemical activities in regulating gene expression and splicing, are critically dependent on its condensation into dynamic and liquid-like droplets, and is negatively affected by perturbation toward a more solid-like state.

DISCUSSION

Phase separation as a fundamental principle of cellular organization is associated with a wide variety of cellular processes and certain human diseases, mostly neurodegenerative disorders involving pathological protein aggregation. However, direct demonstration of a role of biomolecular condensation in other types of disease, such as cancer, has been rare. Our results allow us to propose a model for the role of AKAP95 phase separation in spatial regulation of gene expression that underlies tumorigenesis (**Figure S7H**). AKAP95 binds to many transcription and splicing regulators at its N-terminal region, and to RNAs at its zinc finger domains. Possibly coordinated by multivalent interactions with other proteins and RNAs, the 101-210 region of AKAP95 with correct amino acid composition drives its phase separation and assembly of non-membrane compartment with appropriate material properties in the cell nucleus. Such assemblies create a high local concentration of factors with proper dynamics, which optimize their enzymatic and non-enzymatic activities necessary for gene expression. These activities may include bridging splice junctions for efficient splicing and looping out intervening RNA sequences for alternative exon inclusion (or exclusion), and/or assembly and modifications of splicing factors to be dynamically supplied to active splicing elsewhere. In the event of oncogenic activation, the AKAP95 liquid-like condensates maintains a gene expression program that is essential for multiple aspects of tumorigenesis including promoting cell growth and suppressing apoptosis and senescence (**Figure 2K**). Our data link the biophysical properties of AKAP95 in condensates to its physiological function in tumorigenesis via its biochemical activities in gene regulation. Based on the largely shared structural features of many RNA-binding proteins (Castello et al., 2012), we think that this is likely a more generalizable model for many RNA-binding proteins involved in gene regulation.

Differential requirement of AKAP95 in normal versus tumor cells through regulation of gene expression

Consistent with a previous report on a gene-trap mouse model that produces a truncated Akap95 protein containing only the N-terminal 354 residues (Yang et al., 2006), here our *Akap95* KO mice and cells show that Akap95 is dispensable for normal animal development and primary cell growth. However, our work here has provided multiple lines of evidence that together indicate an important role of AKAP95 in tumorigenesis, though a more physiologically relevant tumor model will be instrumental to firmly demonstrate a role of AKAP95 in tumorigenesis. AKAP95 is required for the optimal proliferation and viability of cancer cell lines and their tumorigenicity in animals. It is also required for oncogenes to transform a normal cell to a cancer cell, at least partially via overcoming the oncogene-induced senescence, a potent barrier to cancer. The clinical relevance is shown by the frequent amplification and mRNA upregulation of AKAP95 in a wide variety of human cancers, as well as the correlation of the dysregulation of AKAP95 with patient prognosis. These findings corroborate previous reports on the association of *AKAP95* overexpression in clinical cancer samples (Chen et al., 2016; Liu et al., 2015; Qi et al., 2015). The differential requirement of AKAP95 in normal versus tumor cells suggests that AKAP95 may represent a novel target for cancer treatment with a potential therapeutic window.

Our findings are in line with the growing concept that as cancers cells rewire many pathways to cope with numerous cellular stresses not encountered by normal cells, they become exceptionally dependent on these pathways compared to normal cells (Bradner et al., 2017; Luo et al., 2009). MYC selectively amplifies the expression of numerous genes (Kress et al., 2015) and greatly enhances the burden on many cellular pathways including transcription and RNA splicing, and thus sensitizes the cells to even partial loss of components in these pathways (Hsu et al., 2015; Koh et al., 2015; Yang et al., 2018). We surmise that AKAP95 and other factors (including its paralog HA95) together regulate gene expression for cell growth and survival. In normal cells, loss of AKAP95 can be compensated by other related factors and does not produce a noticeable consequence. In cancer cells or in the process of becoming cancer cells, other factors are not sufficient to compensate the loss of AKAP95 due to the elevated demand on gene expression including splicing. Moreover, oncogene activation induces compensatory tumor-suppressive responses that restrains tumorigenesis. Here we show that *MYC* activation promotes the expression of *AKAP95* (**Figure 2J**) and requires AKAP95's activity to overcome the senescence barrier to tumorigenesis.

Prior to our reports of the roles of AKAP95 in regulation gene expression (Hu et al., 2016; Jiang et al., 2013), the best studied function of AKAP95 was its mediation of chromatin condensation (Bomar et al., 2002; Collas et al., 1999) among its other functions in the nucleus (Eide et al., 2003; Jungmann and Kiryukhina, 2005; Li et al., 2006). However, the activity of AKAP95 in mediating chromatin condensation (Eide et al., 2002) is unlikely to be the key mechanism for its role in tumorigenesis. This is because that the activity of AKAP95 in combating oncogene-induced senescence requires its N-terminal 1-100 region (**Figure 2I**), which is required for its activity in regulation of gene expression including splicing (Hu et al., 2016; Jiang et al., 2013) but not chromatin condensation (Eide et al., 2002). As our unbiased proteomic approach has shown that AKAP95 is mainly associated with proteins in RNA processing and transcription (Hu et al., 2016), we lean toward an explanation of regulation of tumorigenesis by AKAP95 mainly through control of gene expression, but do not exclude the contribution from other mechanisms.

Modulation of the material properties of the AKAP95 condensates

Our results suggest that the aromatic ring of Tyr is required for, and the hydroxy group of Tyr antagonizes (but does not eliminates), AKAP95 condensation. The abundant and conserved Arg residues further suggest that cation-π interactions between the positively charged Arg side chain and the aromatic side chain of Tyr may be a crucial force for AKAP95 condensation. The effect of YF mutation on AKAP95 is opposite to that on the FUS family proteins, where it weakens condensation (Wang et al., 2018). This suggests that the impact of the primary sequence and/or amino acid composition of proteins on phase separation is context-dependent, and the diverse regulation of biomolecular condensation (including material properties) by the same amino acids in different proteins may offer diverse regulation of biological functions. Our results suggest that it is important to maintain a balance of Phe and Tyr residues in a protein for achieving proper material state and dynamics, as they can have profound consequences on biochemical and cellular activities. In support of this notion, Phe and Tyr are highly conserved in the 101-210 region of AKAP95 between mouse and human, and the only alteration of Phe to Tyr (at 131) in this region in human AKAP95 is compensated by the reverse mutation of Tyr to Phe (at 170) (**Figure 5A**).

Prion-like domains are often linked to drive protein phase separation or aggregation (Wang et al., 2018). We here find that while AKAP95 has a prion-like domain at the very N-terminal region (**Figure S3B**), this region is not responsible for the condensation property of AKAP95. Rather, it is mainly responsible for binding to many protein factors in gene expression (Hu et al., 2016), and is also important for AKAP95 in regulation splicing (Hu et al., 2016) and combating oncogene-induced senescence (**Figure 2I**).

Essential role of phase separation for the activities of AKAP95 in regulating gene expression and tumorigenesis

It is a general challenge to unequivocally demonstrate a causal link of the phase separation property to a specific biological function. Here we provide several lines of evidence to support our conclusion that the phase separation property of AKAP95 underlies its activities in regulation of splicing and in tumorigenesis. **(i)** Deletion of, or YA or YS mutations in, AKAP95 (101-210), which disrupted the in vitro phase separation ability of 101-210 and the in vivo foci formation of the full-length AKAP95, also abolished the splicing activity of AKAP95 in both the splice reporter and endogenous alternative splicing, and also abolished the biological activities of AKAP95 in promoting cancer cell growth and clonogenicity and suppressing oncogene-induced senescence; **(ii)** Deletion of 101-210 does not affect the ability of AKAP95 in binding to other proteins in splice regulation; **(iii)** The splicing ability can be more or less regained by replacement of 101-210 of AKAP95 with condensation-competent IDRs from three proteins that are involved in cellular pathways irrelevant to AKAP95. Although AKAP95 is associated with many hnRNPs, the abundant hnRNP A1 is neither physically nor functionally (in splicing regulation) associated with AKAP95 (Hu et al., 2016), yet the hnRNP A1 IDR can fully replace the splicing activity of the AKAP95 IDR. The lack of or sub-optimal abilities in retaining splice regulation by the IDRs from yeast eIF4GII, Pub1, or Lsm4 can be due to several reasons, including their relatively low expression levels (for Pub1 and Lsm4, **Figure 5H, bottom**) and the possibility that the material properties mediated by these IDRs may not be in the appropriate range for splice regulation. Lsm4 IDR-chimera showed modest activity in splice reporter assay, but its activity was lower than the hnRNP A1 IDR-chimera and comparable to AKAP95 (YF) mutant. This is consistent with both Lsm4 IDR (Lin et al., 2015) and AKAP95 YF being prone to form less dynamic condensates. However, we have to be very cautious in interpreting the regulation of splicing (or other biological functions) by material properties of the chimera condensates, because this can be complicated by the detailed (including potentially unknown) properties of the different sequences of these IDRs from very distant species. As one example, although the eIF4GII IDR forms liquid-like droplets in vitro (Lin et al., 2015) and confers a punctate nuclear distribution of its associated AKAP95 chimera (**Figure 5G**), its corresponding AKAP95 chimera did not show consistent activity in our splice reporter assay (**Figure 5H**). This is likely because that the eIF4GII IDR itself, unlike the other three IDRs tested here, has intrinsic RNA-binding activity (Lin et al., 2015). Being part of a yeast protein involved in translation initiation, it most likely binds to RNA sequences or structures quite different from those mammalian RNA regions involved in intron splicing, and thus would conceivably interfere with binding to the correct RNA regions required for splice regulation in human cells.

Therefore, although one can never formally exclude the possibility that other activities that may associate with Tyr of AKAP95 (101-210) account for the observed biological effects, our results strongly suggest that the phase separation property of this region is important for AKAP95 in splice regulation and probably tumor control as well.

Regulation of biochemical and physiological activities by material properties of condensates

Material properties of biomolecular compartments have been proposed theoretically to impact reaction kinetics by affecting the local concentration and the interaction rate of enzyme and substrate (Banani et al., 2017). This notion can be relatively easily demonstrated in a simple reaction system in vitro, but it remains to be demonstrated whether this is a mechanism at work in the complex living systems. Here we show that both the optimal growth of cancer cells and the successful transformation to cancer cells by oncogenes require the AKAP95 molecules be in liquid-like condensates with a proper window of dynamics to be active in regulating gene expression including splicing. Specific mutations that abolish AKAP95 condensation renders AKAP95 completely lose its ability in regulating splicing, promoting cancer cell growth, and overcoming oncogene-induced senescence. This is conceivably a result of failure in concentrating splicing factors into local proximity. The effect of YF mutation, which preserves AKAP95 condensation, on splicing was initially surprising. We then show that this mutation alters both the condensation propensity and the material properties of the condensates in the other direction, i.e., enhanced condensation propensity and toward a hardened state with much reduced dynamics both as a purified protein and in cells, suggesting that the hardened compartment generated by the YF mutant negatively impacts the kinetics of the molecular interactions necessary for splicing reaction. As condensates are porous structures with the free volume between the condensed scaffold components as pores (Banani et al., 2017), the hardened YF condensates may restrict the rapid movement and interactions of other macromolecules such as other splicing modulators and RNA substrates, and thus slow down the kinetics of biochemical reactions inside. Such molecular restriction is not as detrimental to biochemical activities as the disruption of condensation caused by the YA or YS mutations, but is sufficient to generate significant biological effects on a subset of gene expression events and also on the growth of cancer cells and senescence state of oncogene-stressed cells. Alternatively but not mutually exclusively, the nuclear AKAP95 foci may provide a microenvironment for the assembly and modifications of functional splicing factors and as a dynamic supply for these factors needed for active splicing in other nuclear locations. In this alternative model, we can also appreciate the negative impact on the splicing factor assembly or availability by either a diffuse (YA and YS) or a rigid (YF) state of AKAP95. Regardless of the molecular implementations of AKAP95, the requirement of its condensate state with appropriate material properties in gene regulation and tumorigenesis is substantiated by our studies. While previous studies (Boija et al., 2018; Chong et al., 2018; Gueroussov et al., 2017; Sabari et al., 2018; Ying et al., 2017) are forming the concept that gene regulation is activated by condensation of the key regulators, our work adds a major modification to this concept to highlight that, instead of two simple states (diffuse or condensate) that act as an on/off switch for activity, a gene regulator can be in a continuous gradient of varying material states, in which only a proper window confers biological activity (**Figure 7L**).

Many questions remain open that warrant further studies. We do not yet know the precise material states of either the WT or the YF mutant of AKAP95 in vitro or in the cell nucleus. The imperfect spherical shape, incomplete recovery after FRAP, and the incomplete and relatively slow rate of condensate fusion all suggest that the WT AKAP95, while definitely possessing liquid-like properties, is probably somewhere between a highly viscous liquid and a hydrogel state. The YF mutant condensates are not really in a solid state, but clearly shifting toward that direction from the state of the WT condensates. The situation is further complicated by numerous nuclear factors in cells. Therefore, an important question is what quantitative changes in the physical properties of the condensates are required to elicit the changes in the biochemical and biological outcomes, not only for AKAP95 but also potentially for other proteins that regulate biochemical reactions? The potential role of RNAs in tuning various properties of AKAP95 condensation and biological activities is unclear. Nuclear RNAs can act as buffer for protein condensation but specific structures of RNAs can promote the assembly of condensates (Langdon et al., 2018; Maharana et al., 2018). RNA binding at the zinc finger domains is clearly not essential for AKAP95 condensation in vitro and in cells. Loss of RNA binding at the zinc finger domains of AKAP95 actually results in nuclear condensates with rounder morphology (**Figure 4D**) and faster dynamics (**Figure 4E** and **4G**), suggesting a role of nuclear AKAP95 zinc finger-interacting RNAs in enhancing AKAP95 condensation or shifting the material state of the condensates from a more fluid state toward a less fluid state. It is also intriguing how the phenolic hydroxy group on Tyr appears to have very different impact on condensation of AKAP95 from the FUS family proteins. While multiple studies suggest that AKAP95 associates with chromatin (Eide et al., 2002; Li et al., 2006) and nuclear matrix (Akileswaran et al., 2001), it remains unclear if the phase separation property of AKAP95 is involved in the chromatin association. The role and mechanisms of AKAP95 phase separation in regulating the transcription process are also very vague. It also remains to be explored how signaling pathways may modulate the activities of AKAP95 in controlling gene expression and tumorigenesis through impacting its condensate properties.

In summary, our studies reveal the importance of controlling the propensity and material properties of biomolecular condensates in regulation of gene expression and biological processes that are controlled by gene expression (which are numerous and include tumorigenesis), as perturbing such properties in either direction can produce profound biological consequences. Our findings also raise the novel possibility that certain cancers may be inhibited by chemicals or approaches that perturb the material properties of the condensates of key players in either direction, i.e., disrupting or hardening the condensation out of its normal window of liquidity and dynamicity (**Figure 7L**).

MATERIALS AND METHODS

STAR METHODS

KEY RESOURCES TABLE

REAGENT or RESOURCE	SOURCE	IDENTIFIER
Antibodies		
Rabbit polyclonal anti-AKAP95	Santa Cruz Biotechnology	Cat#sc-10766; RRID:AB_2226060
Rabbit polyclonal anti-AKAP95	Bethyl Laboratories	Cat#A301-062A RRID:AB_2258195 (Used only in Figure S5H as the other anti-AKAP95 antibody is discontinued)

Mouse monoclonal anti-GAPDH	EMD Millipore	Cat#MAB374; RRID:AB_2107445
AlexaFluor 555 conjugated goat anti-rabbit IgG	Thermo Fisher Scientific	Cat#A-21428; RRID:AB_141784
Mouse anti-SRSF2 antibody	Abcam	Cat#Ab11826; RRID:AB_298608
Rabbit polyclonal anti-cyclin A	Santa Cruz Biotechnology	Cat#sc-751; RRID:AB_631329
Rabbit polyclonal anti-DDX5	Santa Cruz Biotechnology	Cat#sc-32858; RRID:AB_2261540
Mouse monoclonal anti-hnRNP M	Santa Cruz Biotechnology	Cat#sc-20002; RRID:AB_627739
Rabbit polyclonal anti-RNA Pol II (RPB1)	Santa Cruz Biotechnology	Cat#sc-899; RRID:AB_632359
AlexaFluor 555 conjugated goat anti-mouse IgG	Thermo Fisher Scientific	Cat# A-21422; RRID:AB_141822
Chemicals, Peptides, and recombinant proteins		
Amylose resin	New England Biolabs	Cat#E8021L
Polyethylenimine	Sigma-Aldrich	Cat#408727
Lipofectamine 2000	Thermo Fisher Scientific	Cat#11668027
PEG6000	EMD Millipore	Cat#528877
Crystal violet	Sigma-Aldrich	Cat#C0775
1,6-Hexanediol	Sigma-Aldrich	Cat#240117
2,5-Hexanediol	Sigma-Aldrich	Cat#H11904
1,5-Pentanediol	Sigma-Aldrich	Cat#76892
1,4-Butanediol	Sigma-Aldrich	Cat#406198
Thioflavin T	Sigma-Aldrich	Cat#T3516
Oregon Green™ 488 Carboxylic Acid	Thermo Fisher Scientific	Cat#O6147
Bio-Spin® P-6 Gel Columns	BioRad	Cat#7326002
ProTEV protease	Promega	Cat# V6102
Anti-flag M2 affinity Gel	Sigma-Aldrich	Cat#A2220
Protease inhibitor cocktail	Roche	Cat# 4693159001
Critical commercial assays		
Senescence cells histochemical staining kit	Sigma-Aldrich	Cat#CS0030
FITC-BrdU Flow kit	BD Biosciences	Cat# 559619
FITC Annexin V Apoptosis Detection Kit with 7-AAD	BioLegend	Cat# 640922
Experimental Models: Cell lines		
MDA-MB-231	Lizhong Wang Lab, UAB	N/A
MCF7	ATCC	HTB-22
HeLa	ATCC	CCL-2
HEK 293	Hu et al., 2016	N/A
293T	Hu et al., 2016	N/A
Flp-In T-REx 293	Thermo Fisher Scientific	N/A

Experimental Models: Organisms/Strains		
NSG mouse	The Jackson Laboratory	Cat#005557
Akap95 KO mouse	This paper	N/A
Recombinant DNA		
pMD2.G	Addgene	Cat#12259
pSPAX2	Addgene	Cat#12260
pEco	Clontech	Cat#631530
pBabe-puro Ras V12	Addgene	Cat#1768
pWZL Blast Myc	Addgene	Cat#10674
pCDH-MSCV-MCS-EF1α-GFP+Puro	System Biosciences	Cat# CD713B-1
pLKO.1-AKAP95 sh#1 (Puro^R)	Hu et al., 2016	N/A
pLKO.1-AKAP95 sh#2 (Puro^R)	Hu et al., 2016	N/A
pLKO.1-AKAP95 sh#1 (BSD^R)	This paper	N/A
pLKO.1-CCNA2 sh#1 (Puro^R)	This paper	N/A
pLKO.1-CCNA2 sh#2 (Puro^R)	This paper	N/A
pTripZ- AKAP95-HA	This paper	N/A
pTripZ-AKAP95 (full-length, with YF in 101-210)-HA	This paper	N/A
pTripZ-AKAP95 (full-length, with YS in 101-210)-HA	This paper	N/A
pTripZ-AKAP95 (101-692)	This paper	N/A
pCDH-Flag-HA-AKAP95	This paper	N/A
pCDH-Flag-HA-AKAP95 (full-length, with YF in 101-210)	This paper	N/A
pCDH-Flag-HA- AKAP95 (full-length, with YS in 101-210)	This paper	N/A
pcDNA5-Flag-HA-AKAP95	This paper	N/A
pcDNA5-Flag-HA-AKAP95 (aa101-210, YF)	This paper	N/A
pcDNA5-Flag-HA-AKAP95 (full-length, with YS in 101-210)	This paper	N/A
pcDNA5-Flag-HA-AKAP95 (full-length, with YA in 101-210)	This paper	N/A
pcDNA5-Flag-HA-AKAP95 (Δ101-210)	This paper	N/A
pcDNA5-Flag-HA-AKAP95-GFP	This paper	N/A
pcDNA5-Flag-HA-AKAP95 (full-length, with YF in 101-210)-GFP	This paper	N/A
pcDNA5-Flag-HA-AKAP95 (full-length, with YS in 101-210)-GFP	This paper	N/A
pcDNA5-Flag-HA-AKAP95 (full-length, with YA in 101-210)-GFP	This paper	N/A
pcDNA5-Flag-HA-AKAP95 (Δ101-210)-GFP	This paper	N/A
pET28-MBP-TEV	Addgene	Cat#69929
pET28-MBP-TEV-AKAP95	This paper	N/A

pET28-MBP-TEV-AKAP95 aa1-340	This paper	N/A
pET28-MBP-TEV-AKAP95 aa306-692	This paper	N/A
pET28-MBP-TEV-AKAP95 aa1-100	This paper	N/A
pET28-MBP-TEV-AKAP95 aa101-210	This paper	N/A
pET28-MBP-TEV-AKAP95 aa211-340	This paper	N/A
pET28-MBP-TEV-AKAP95 aa1-340 (Δ101-210)	This paper	N/A
pET28-MBP-TEV-AKAP95 aa101-210 YF	This paper	N/A
pET28-MBP-TEV-AKAP95 aa101-210 YS	This paper	N/A
pET28-MBP-TEV-AKAP95 aa101-210 YA	This paper	N/A
Primers for PCR, siRNAs and shRNAs, see Table S3	This paper	N/A
Software and Algorithms		
cBioPortal		http://www.cbioportal.org/
ImageJ	NIH	http://imagej.nih.gov/ij/
SPSS	IBM	https://www.ibm.com/analytics/spss-statistics-software
RStudio	RStudio	http://www.rstudio.com/
ZEN 2012	Zeiss	http://www.zeiss.com/microscopy/en_us/downloads/zen.html
FRAPanalyser		http://actinsim.uni.lu/eng/Downloads
IUPred		http://iupred.elte.hu/
PLAAC		http://plaac.wi.mit.edu/
Composition Profiler		http://www.cprofiler.org/cgi-bin/profiler.cgi
ExPASy ProtParam		https://web.expasy.org/protparam/
Metascape		http://metascape.org/gp/index.html#/main/step1
MISO	Katz et al. 2010	http://genes.mit.edu/burgelab/miso/
FlowJo		https://www.flowjo.com/
Tophat version v2.1.1		https://ccb.jhu.edu/software/tophat/index.shtml
HTseq v0.10.0		https://htseq.readthedocs.io/en/release_0.10.0/
DESeq2 v3.8		https://www.bioconductor.org/packages/release/bioc/html/DESeq2.html

DAVID v6.8		https://david.ncifcrf.gov/
GSEA		http://software.broadinstitute.org/gsea/index.jsp

CONTACT FOR REAGENT AND RESOURCE SHARING

Further information and requests for reagents may be directed to, and will be fulfilled by the Lead Contact, Hao Jiang (hj8d@virginia.edu).

EXPERIMENTAL MODEL AND SUBJECT DETAILS

Animals

All animal procedures were approved by the Institutional Animal Care and Use Committee at the University of Alabama at Birmingham. All mice were maintained under specific pathogen–free conditions and housed in individually ventilated cages. Immune-deficient NSG (NOD.Cg-Prkdcscid Il2rgtm1Wjl/SzJ) mice were purchased from The Jackson Laboratory. To generate the *Akap95* KO mice, embryonic stem cells on C57BL/6 background that harbor an Akap8$^{tm1a(EUCOMM)Hmgu}$ (Knockout-first, thus null "-") allele were purchased from EUCOMM (Helmholtz Zentrum München, Germany), and were injected into blastocysts to generate chimeras at the University of Alabama at Birmingham Transgenic Mouse Facility. *Akap95*$^{+/-}$ mice with germline transmitted *Akap95*-targeted allele (−) allele were selected for further crossing to generate WT, *Akap95*$^{+/-}$ *and Akap95*$^{-/-}$ mice.

Cells

Primary mouse embryonic fibroblasts (MEFs) isolation, culture, growth assays, transformation, soft agar colony formation, and in vivo tumorigenesis assays were performed as previously described (Yang et al., 2018). Briefly, MEFs were harvested from E13.5 embryos from cross of *Akap95*$^{+/-}$ female and male mice. Early passages of MEFs were frozen in the liquid nitrogen, and cultured in DMEM plus 10% FBS at use. Flp-In T-REx 293 cells stably expressing AKAP95 WT or mutants were generated using the Flp-In system (Thermo Fisher Scientific) according to the manufacturer's instructions. Protein expression was induced with doxycycline for 48 hrs. MDA-MB-231 cells were a kind gift from Lizhong Wang (University of Alabama at Birmingham). HeLa, MDA-MB-231, MCF7, HEK 293, 239T, Flp-In T-REx 293 cells were cultured in DMEM (Thermo Fisher Scientific) supplemented with 10% fetal bovine serum (Thermo Fisher Scientific).

METHOD DETAILS

Constructs

Human *AKAP95* cDNA in pcDNA5/FRT/TO (pc5, Invitrogen) with an N-terminal Flag-HA-(FH-) tag was previously described (Jiang et al., 2013). Truncation mutants of AKAP95 were generated by PCR cloning. In particular, the FH-AKAP95 Δ(101-210) construct was generated with a BamHI site replacing the 101-210 region. Tyrosine mutants of the 101-210 region in AKAP95 were synthesized (Biomatik USA, LLC, Delaware, USA). The full length AKAP95 mutants were achieved through in-fusion PCR cloning. To generate AKAP95 chimeras, human hnRNPA1 (186-320), yeast Pub1 (243-327), yeast Lsm4 (91-187), and yeast eIF4GII (13-97) sequences were cloned from the cDNAs of human HEK 293 cells and yeast Saccharomyces cerevisiae, respectively, and inserted at the BamHI site in the FH-AKAP95 Δ(101-210) construct to generate the AKAP95 chimeras. For rescue constructs, AKAP95 WT and full-length AKAP95 mutants that have indicated tyrosine mutations within 101-210 were cloned into pTripZ (Dharmacon) between AgeI and MluI sites (replacing the tRFP and mir sequences in the vector) for doxycycline-inducible expression, and also cloned into pCDH-MSCV-MCS-EF1α-GFP+Puro lentiviral vector (System Biosciences, Cat# CD713B-1, Palo Alto, CA) for constitutive expression. For protein expression as MBP-fusion, AKAP95 or its variants and FUS were cloned into pET28-MBP-TEV vector (Addgene: #69929) downstream of the TEV cleavage site. The sequences of all plasmids were confirmed by Sanger sequencing.

Virus package and concentration

Lentiviral vectors were packed with psPAX2 and pMD2.G in 293T cells with polyethylenimine (PEI) transfection reagent. Retroviral vectors pBabe-puro Ras V12 (Addgene #1768) and pWZL-Blast-myc (Addgene #10674) were packed with pEco (Clontech) in 293T cells. The viral solutions were 30-fold concentrated by PEG6000 precipitation, then aliquot and stored at -80°C.

Gene knockdown, cell growth, and colony formation assay

AKAP95 KD was performed by either lentivirus-mediated shRNA or transient transfection of siRNA as described (Hu et al., 2016). Detailed information for shRNAs and siRNAs is in Table S3. MDA-MB-231 cells infected with pLKO-based shRNA lentivirus were selected under 20 μg/ml blasticidin for 3 days. For rescue assays, cells were infected with pCDH-based lentivirus and selected in 2 μg/ml puromycin for 3 days, and further infected with pLKO-based shRNA lentiviruses for KD. For cell growth assays, 5 × 10^4 cells/well seeded in 6-well plates were cultured in DMEM plus 10% FBS without antibiotics, cell number was counted manually at 5 days of culture or at indicated time points for multiple-time points assays, and cells were fixed with 4% formaldehyde and stained with 0.1% crystal violet solution 5 days after culture. For colony formation assay, 3,000 cells/well in 6-well plates were cultured without antibiotics, and cells were fixed with 4% formaldehyde and stained with 0.1% crystal violet solution and quantified after10-day culture.

Cell proliferation assay and apoptosis assay

Cell proliferation (by BrdU incorporation) and apoptosis (by Annexin V staining) assays were performed as previously described (Yang et al., 2014). For cell proliferation assay, control and AKAP95-KD MDA-MB-231 cells were incubated with BrdU at a final concentration of 10 μM in cell culture medium for 45 min. Cells were harvested and then processed with BrdU staining using the FITC-BrdU Flow kit (BD Pharmingen) following the manufacturer's instructions. For apoptosis assay, cells were harvested and washed twice with cold PBS containing 3% heat-inactivated FBS. Cells were then incubated with FITC-Annexin V (BioLegend) and 7-amino-actinomycin D (7-AAD) for 15 minutes in binding buffer (10 mM HEPES, 140 mM NaCl and 2.5mM $CaCl_2$) at room temperature in dark. The stained cells were analyzed immediately by flow cytometry on LSRFortessa (Becton Dickinson). Data were analyzed using the FlowJo software.

MEF transformation assay and senescence assay

MEFs in early passage (less than four passages) were infected with $H\text{-}RAS^{G12V}$ and c-MYC viral particles followed by selection in puromycin (2 μg/ml) and blasticidin (10 μg/mL). Soft agar colony formation assays were performed by plating transformed MEFs in a 6-well plate at 2,500 cells/well. MEFs were cultured in a layer of MEF culture medium in 0.35% agar over a base layer composed of culture media in 0.5% agar and fed every 4 days. Colonies were formed over the course of 3 to 4 weeks. For MYC-induced senescence assay, MEFs were infected with c-MYC retrovirus and selected against 10 μg/mL blasticidin for 3 days. Four to 5 days post selection, 10^5 cells/well were seeded in 6-well plate. Twenty-four hrs later, the cells were washed twice with PBS, fixed and stained for β-galactosidase activity at pH = 6 using Senescence Cells Histochemical Staining Kit (Sigma, Cat#CS0030). For rescue assays, MYC-transduced $Akap95^{-/-}$ MEF were infected with AKAP95- or mutant-expressing pTripZ lentiviruses and selected under 2 μg/ml puromycin for 3 days. After selection, cells were cultured under 100 ng/mL doxycycline for 4-5 days and then stained for β-galactosidase activity.

Allogeneic and xenogeneic transplantation

Transformed MEF cells and MDA-MB-231 cells were washed and re-suspended in PBS. Subcutaneous injection of 2 × 10^6 control and AKAP95-KD MDA-MB-231 cells in 100 μl PBS were administered into left and right flanks of 8-week-old female NSG mice (NOD.Cg-*Prkdc*^{scid} *Il2rg*^{tm1Wjl}/SzJ, Jackson Laboratory, stock No. 005557), respectively. The same amount of transformed WT and *Akap95*$^{-/-}$ MEF were inoculated into left and right flanks of 8-week-old male NSG mice in the same way. Tumor size was measured in the 2 longest dimensions using a Vernier caliper. Tumor volume (V) was calculated with the formula $V = D1(D2)^2/2$, where D1 is the long dimension and D2 is the short dimension. Four weeks after transplantation, mice were humanely sacrificed for collecting tumors. The tumors were also weighed.

Analyses for protein disorder, domain, and amino acid composition

The prion-like domain was identified using the PLAAC (http://plaac.wi.mit.edu/) with the core length set to be 30 and the background set to be homo sapiens. Disordered regions were identified using IUPred (http://iupred.elte.hu/). Amino acid composition was analyzed by Composition Profiler (http://www.cprofiler.org/cgi-bin/profiler.cgi) by using SwissProt 51 Dataset as the background sample.

Co-immunoprecipitation assay

Co-immunoprecipitation assays were performed as described (Hu et al., 2016). Briefly, 293T cells were transfected with indicated constructs. Twenty-four hrs later, cells were lysed in BC300 [50mM Tris (pH 7.4), 300mM KCl, 20% glycerol, 0.2 mM EDTA] with 0.1% NP40, 1mM DTT, and protease inhibitor cocktail (Roche, Cat# 4693159001). Lysates were incubated with the anti-Flag M2 antibody (Sigma, A2220) and washed by the lysis buffer. Bead-bound proteins were resolved by SDS-PAGE and detected by immunoblotting using indicated antibodies.

Protein expression and purification

The pET28-MBP-TEV-based constructs were transformed into BL21 Star (DE3) (Thermo Fisher Scientific, Cat# C601003) *E. coli*. Bacteria culture at OD600 of 0.6 were induced with 0.4 mM of Isopropyl β-D-1-thiogalactopyranoside (IPTG) for 5 hours at 25°C to express MBP-fusion proteins. The pET28-MBP-TEV vector itself was used to express MBP control, which was MBP and a small peptide (sequence GSLSTGCY) after cleavage by TEV protease. Bacterial cells were resuspended in BC500 [50 mM Tris (pH 7.4), 500 mM KCl, 20% glycerol, 0.2 mM EDTA], 0.1%

NP40, protease inhibitor cocktail (Roche, Cat# 4693159001), 1mM DTT, and lysed by sonication. After centrifugation, the supernatant was incubated with pre-equilibrated Amylose resin (New England BioLabs, Cat# E8021) in batch for three times. The resin was pooled, washed with the lysis buffer 4 times with one additional wash in BC0, and eluted in multiple fractions in 10 mM Maltose in BC0 buffer. Purified proteins were examined by SDS-PAGE followed by coomassie blue staining. Protein concentration was determined by Nanodrop measurement for OD_{280} and calculation using extinction coefficient provided by ExPASy ProtParam (https://web.expasy.org/protparam/).

In vitro phase separation assay

For in vitro phase separation assays, the MBP-tag was cleaved off the fusion proteins by ProTEV Plus (Promega, Cat# V6102). Sometimes, AKAP95 (101-210) and its YF mutant were fluorescently labeled with Oregon green 488 carboxylic acid succinimidyl ester following manufacturer's instructions. Briefly, the protein solution was first replaced with 0.1 M sodium bicarbonate buffer by dialysis. 20 µl of 10 mg/ml fluorophore were added into 2 mg protein and incubated at 4 °C in dark overnight. The protein was purified on a Bio-Spin® P-6 Gel Columns (BioRad) desalting column equilibrated in BC-0 buffer to separate labeled protein from excess fluorophore and then stored at -80 °C. The calculated labeling efficiency was 1 in 2 molecules for both proteins.

Phase separation was assessed by 4 ways: (1) visual observation of the turbidity. (2) Measurement of the optical density at wavelength of 600 nm (OD600) or 450 nm (OD450) for turbidity by Nanodrop. The kinetics of turbidity development was determined by OD450 measurement in 96-well plate on a Synergy HTX plate reader (BioTek). Readings were taken once every 10 seconds and analyzed by the Gen5 Data Analysis Software (BioTek). (3) Separation of the condensates from the aqueous phase by centrifugation at 5000 rpm for 10 min, followed by SDS-PAGE and Coomassie blue staining of the supernatant and mixed samples. (4) Microscopy-based method. 30 min after TEV protease treatment, the protein solution was added into a homemade flow chamber comprised of a glass slide sandwiched by a coverslip with one layer of double-sided tape as a spacer. Images were taken on Zeiss LSM780 confocal microscope with 60X oil lens.

For in vitro fibril formation assay and Thioflavin-T staining, MBP-FUS and MBP-AKAP95 (101-210) YF mutant were treated with ProTEV protease for 2 hrs. The protein solution was then added into a solution of 20 μM ThT for incubation for 5 min. After that, 1-2 μL of the protein solution were loaded into the homemade flow chamber for imaging on Zeiss LSM780 confocal microscope.

Immunofluorescence and live cell imaging

HeLa, MDA-MB-231, and MEF cells were washed with PBS and fixed with ice cold methanol for 15 min. The fixed cells were incubated with 1:250 rabbit anti-AKAP95 antibodies overnight at 4°C, and developed with 1: 300 AlexaFluor 555 conjugated goat anti-rabbit secondary antibody for 1 hr at room temperature. For melting of AKAP95 nuclear bodies by aliphatic alcohols, HeLa cells were exposed to 8% aliphatic alcohols for 5 min before fixation. For AKAP95 colocalization with SRSF2, HeLa cells were transfected with pcDNA5-flag-HA-AKAP95-GFP 24 hrs before fixation. Cells were then incubated with mouse anti-SRSF2 (SC-35) antibodies followed by AlexaFluor 555 conjugated goat anti-mouse secondary antibody. The slides were further counterstained with DAPI. All immunostaining images were acquired on Nikon A1 confocal microscope with 60X oil lens. Intensities of AKAP95 and SRSF2 signals were analyzed by ImageJ. For live cell imaging, HeLa cells transiently transfected with indicated constructs and Flp-In T-REx 293 stable cells were cultured in 35 mm glass-bottom dishes (MatTek), and used for imaging on Zeiss LSM780 confocal microscope supported with a Chamlide TC temperature, humidity and CO_2 chamber. Images were collected by either 40X or 60X oil lens.

Fluorescence recovery after photo-bleaching (FRAP) assays

Hela cells were cultured and transfected as described above. FRAP assays were performed on Zeiss LSM780 confocal microscope at 37°C. GFP signal was bleached using 40% of maximum laser power of a 488-nm laser for approximately 8 s. Puncta with diameters 1-2 um were assayed. The recovery was recorded at the rate of 2 s/frame for 2 min. The FRAP data were analyzed by FRAPanalyzer. The fluorescence intensity difference between pre-bleaching and at time 0 (the time point right after photo-bleaching) were normalized to 100%. For assessing protein condensate dynamics in vitro, Oregon-green 488 labeled proteins were added into unlabeled proteins at a molar ratio of 1: 150. The mixed proteins were treated with ProTEV protease to remove the MBP tag. FRAP assays were performed at 30 minutes after protease treatment, and round areas with diameter 1 μm were bleached with 100% of maximum laser power of a 488-nm laser for approximately 8 sec. The recovery was recorded at the rate of 2 sec/frame for 2-6 min.

Splicing reporter assay

The double reporter splicing assay was performed on pTN24 reporter plasmid (Nasim and Eperon, 2006) as described (Hu et al., 2016). Briefly, HEK 293 cells were transfected with relevant plasmids or siRNA using Lipofectamine 2000 reagent (Thermo Fisher Scientific), and harvested 48 h after transfection. Beta-galactosidase and luciferase activities were measured using Dual-Light System (Applied Biosystems).

RT-PCR and RT-qPCR, and genome-wide expression and splicing analyses

RT-PCR and RT-qPCR to examine relative mRNA levels and alternative splicing, respectively, were performed as previously described (Hu et al., 2016). For RT-PCR, briefly, alternative splicing on selected targets was determined by PCR, and mRNA levels were determined by qPCR, both following RNA isolation and reverse-transcription. Primers are listed in Table S3.

Total RNA quality was assessed with an Agilent 2100 Bioanalyzer. Samples with RNA integrity number greater than 9 were further processed to library preparation and sequencing. For RNA-seq, 2 rounds of polyA+ selection were performed and followed by conversion of mRNA to cDNA. Illumina sequencing adapters and barcodes were then added to the cDNA via PCR amplification. Indexed libraries were then normalized and pooled. 2 x 150 pair-end sequencing was performed using the HiSeq2500 (Illumina) with recommended protocol. 40-60 million reads per sample were mapped to human or mouse reference genome (hg19 and mm9, respectively) using Tophat version v2.0.4. Transcript assembly was performed using HTseq v0.10.0. Assembled RNA-seq count files were imported into RStudio software for analysis of differential expression with DESeq2 v3.8 package. Differential expressed genes with mean count across all groups greater than 10 were chosen for visualization with values scaled by row using RStudio. Gene ontology analysis and Pathway analysis was conducted with DAVID v6.8 and GSEA (Broad Institute, Cambridge, MA, USA) software packages. All GSEA was carried out by using the Hallmark gene sets from the Molecular Signature Database (MsigDB) except that the “Senescence_up” gene set, a collection of genes upregulated in cells undergoing senescence, was curated from (Fridman and Tainsky, 2008), and the SASP gene set was curated from (Coppe et al., 2008).

Alternative splicing isoforms were analyzed with MISO software (Katz et al., 2010) with its version 2.0 annotation of all known AS events according to the online documentation (https://miso.readthedocs.io/en/fastmiso/). Briefly, accepted alignments from Tophat2 output within each sample were imported to MISO software with command miso –run with paired-end option included. Next, pairwise comparisons between samples were performed using compare_miso - compare-samples to detect differentially expressed isoforms. Five different type of alternative splicing events were analyzed: skipped exons (SE), alternative 3'/5'splice sites (A3SS, A5SS), mutually exclusive exons (MXE) and retained introns (RI). As SE was found to be the major type in all analyses, we chose to focus on SE for our detailed analyses in splicing heat maps. MISO outputs were filtered according to the percent-spliced in values to quantify isoform expression.

QUANTIFICATION AND STATISTICAL ANALYSIS

Statistical parameters including the definitions and exact values of n (e.g., number of experiments, number of cells, number of colonies, etc), distributions and deviations are reported in the Figures and corresponding Figure Legends. All data were expressed as average ± SD; n.s., not significant, $*P < 0.05$, $**P< 0.01$ and $***P < 0.001$ using one-way ANOVA with Tukey's post hoc test (for multi-sample groups), 2-tailed unpaired Student's t-test (for two-sample comparison and certain pair-wise comparisons to a specific sample in a multiple sample group), or log-rank test (for survival analysis), as indicated in Figure Legends. Statistical analysis was performed by in SPSS (IBM) or Excel. A P value of less than 0.05 was considered significant.

DATA AND SOFTWARE AVAILABILITY

The RNA-seq data have been deposited in Gene Expression Omnibus database with the accession number GSE122308.

ACKNOWLEDGEMENTS

We thank Lizhong Wang for providing the MDA-MB-231 cells, and Ying Gai Tusing for technical assistance with mice work. This work was supported by Start-up funds from the University of Alabama at Birmingham and the University of Virginia. H.J. is a recipient of the American Society of Hematology Scholar Award, the American Cancer Society Research Scholar Award, and the Leukemia and Lymphoma Society Scholar Award.

AUTHOR CONTRIBUTIONS

H.J. conceived the project. W.L., J.H. and H.J. designed the experiments. W.L. and J.H. conducted the experiments and analyzed the results. B.S. conducted bioinformatic analyses. H.J. analyzed the results and wrote the paper.

DECLARATION OF INTERESTS

The authors declare no competing interests.

FIGURE LEGENDS

Figure 1. AKAP95 regulates cancer cell growth and gene expression.

(A) Frequent amplification of *AKAP95* in human cancers. From cBioPortal (http://www.cbioportal.org/).

(B) Overexpression of *AKAP95* in breast cancer tissues of 82 TNBC patient samples. From cBioPortal. In the top graph, each small box represents a patient sample, and 21% of these patient samples have indicated types of alterations of AKAP95. The graph at the bottom shows the Disease-free survival curves of patients with or without AKAP95 alterations.

(C) MDA-MB-231 cells, a TNBC cell line, were virally infected to stably express scramble control shRNA or two different shRNAs against *AKAP95* followed with cell growth and colony formation assays. Top, immunoblotting of total cell lysates with indicated antibodies. Middle, representative images of indicated cell colonies stained with crystal violet. Bottom, numbers of cells in growth assays were quantified and presented in the bar graph as average ± SD from three independent experiments.

(D) Tumors from xenograft of control or AKAP95-KD MDA-MB-231 cells in immune-deficient NSG mice. Tumor volume was measured at the indicated days post transplantation, and presented in the graph (bottom) as average ± SD (n = 9).

(E-H) Analyses of the RNA-seq results from MDA-MB-231 cells that were virally infected to stably express control shRNA or AKAP95 shRNA #1 (KD, against 3'UTR) as well as the indicated empty vector or AKAP95-expressing construct.

(E) Heat map showing relative expression levels (mRNA steady state levels) of genes that were down- or up-regulated in the indicated cells. The complete gene list with detailed information is in Table S1, tab 1.

(F) GSEA for the indicated gene sets comparing gene expression profiles of control and AKAP95-KD cells. Plots above and below the broken line show gene sets significantly enriched in genes up- and down-regulated by AKAP95 KD, respectively.

(G) Heat map showing relative alternative splicing of genes and clustered by increase or decrease in percent-spliced-in (PSI) values in the indicated cells. The complete gene list with detailed information is in Table S1, tab 2.

(H) Gene ontology analysis for the indicated gene clusters from the heat map in (G). Top (in blue) and bottom (in red) show gene functions significantly enriched in genes with increase or decrease in PSI by AKAP95 KD, respectively.

(I and J) AKAP95 binds to and directly promotes the splicing of *SMAD6* pre-mRNA. **(I)** RNA immunoprecipitation-sequencing (RIP-seq) profiles for *SMAD6* based on our previous work (Hu et al., 2016). In blue are the Anti-FLAG RIP-seq profiles from parental 293 cells (control) or 293 cells stably expressing the FLAG-HA-tagged (FH-) AKAP95 wild type or mutants as indicated. In red are the anti-AKAP95 RIP-seq profiles from control 293 cells or 293 cells with stable AKAP95 KD. In black are the sequencing profiles of total input RNAs from the indicated cells. All profiles have the same Y-axis scale so that they are directly comparable.

(J) mRNA-seq profiles for *SMAD6* in MDA-MB-231 cells that stably expressed control shRNA or AKAP95 shRNA #1 (KD) as well as the indicated empty vector or AKAP95-expressing construct. The numbers of exon junction reads are indicated. The red asterisk at the gene diagram indicates a stop codon 216 bp downstream of exon 1. Y-axis maximum values are 30, 28, 27 (RPM) for control, KD+vec, and KD+AKAP95 tracks, respectively. Note the RIP-seq and mRNA-seq are exactly aligned for the gene, and the reads for the junction of exons 1 and 2 is reduced from 13 to 0 upon AKAP95 KD and modestly rescued back to 3 upon AKAP95 expression, without affecting the junction reads of exons 2 and 3. All profiles were obtained using Integrative Genomics Viewer (IGV).

**P < 0.01, ***P < 0.001, by log-rank test for (B), or Student's t-test in (C) and (D).

See also Figure S1 and Table S1.

Figure 2. Akap95 is dispensable for normal cell growth but required for transformation and overcoming oncogene-induced cellular senescence.

(A) Growth curves of cultured MEFs derived from six *Akap95*$^{+/-}$ (Het) embryos and six *Akap95*$^{-/-}$ (KO) embryos from two litters. Not significant between the two genotypes at any time point.

(B-D) *Akap95* Het and KO MEFs were transduced with HRAS^{G12V} and MYC viruses.

(B) The relative mRNA levels of *HRAS* and *MYC* were determined by RT-qPCR and normalized to *Actb*, and plotted as average ± SD from MEFs of two different embryos for each genotype.

(C) MEFs were used for soft agar colony formation assay. Left, representative images of the colonies. Right, colony numbers were quantified and plotted as average ± SD from 6 experiments using MEFs of two different embryos for each genotype (3 experiments for each embryo).

(D) Six mice received transduced Het MEFs on one flank and the same number of transduced KO MEFs on the other flank. Four weeks after injection, tumors were collected for picture (left) and weighing. The tumor weights are plotted, where each dot represents a tumor from an animal.

(E-J) MEFs derived from 3 KO and 3 Akap95-expressing (containing 1 WT and 2 Het) embryos were transduced with MYC virus. Untransduced and transduced MEFs were used for various assays.

(E) Right, representative images of cells before (normal) and after MYC transduction are shown. Representative images of SA-beta-galactosidase activity assay after MYC transduction are shown at the bottom. The relative mRNA levels of *MYC* after MYC transduction were determined by RT-qPCR and normalized to *Actb* (left top), and the percentage of SA-beta-gal positive cells was quantified (left bottom), both as average ± SD from MEFs derived from 3 KO and 3 Akap95-expressing embryos. Images of more MEFs are shown in Figure S2E.

(F) Heat map showing relative expression levels of genes and clustered by down- or up-regulation in MYC-transduced KO MEFs compared to Het MEFs from two embryos for each. The complete gene list with detailed information is in Table S2, tab 1.

(G) Gene ontology analysis for the indicated gene clusters from the heat map in (G). Top (in blue) and bottom (in red) show gene functions significantly enriched in genes down- and up-regulated by in the MYC-transduced KO MEFs compared to MYC-transduced Het MEFs, respectively.

(H) GSEA for the indicated gene sets comparing gene expression of control and AKAP95-KD cells. Plots above and below the broken line show gene sets significantly enriched in genes down- and up-regulated in the MYC-transduced KO MEFs compared to MYC-transduced Het MEFs, respectively.

(I) MYC-transduced KO MEFs were virally infected to stably express empty vector (vec) or HA-tagged human AKAP95 WT or 101-692 truncation. Total cell lysates were used for immunoblotting with indicated antibodies (top left). Het MEF lysate was loaded for comparison. Percentages of SA-beta-gal positive cells was quantified and presented (top right) as average ± SD from MEFs derived from 2 Het and 2 KO embryos. Representative images of SA-beta-galactosidase activity assay are shown at bottom.

(J) Relative mRNA levels of *Akap95* and *Ccna2* before and after MYC transduction as determined by RT-qPCR and normalized to *Actb*, and plotted as average ± SD from MEFs derived from 3 KO and 2 Het embryos.

(K) A diagram summarizing regulation of tumorigenesis by AKAP95 through gene expression control.

$^{*}P < 0.05$, $^{**}P < 0.01$, $^{***}P < 0.001$, by Student's t test for all except by one-way ANOVA followed by Tukey's post hoc test for (J).

See also Figure S2 and Table S2.

Figure 3. AKAP95 undergoes phase separation with liquid-like properties in vitro.

(A) Immunoblotting by α-AKAP95 of HeLa cell nuclear extract and AKAP95 immunoprecipitation from the extract. Samples were boiled and resolved by SDS-PAGE. Blue and red asterisks indicate monomer and dimer, respectively.

(B) Disorder plot of human AKAP95 by IUPred (http://iupred.elte.hu/).

(C) Turbidity, as shown by pictures and OD600, of MBP (none) and MBP fused to AKAP95 truncations at indicated protein concentrations, all in 30 mM NaCl, before (TEV 0 min) and after TEV protease treatment for indicated time.

(D) Representative images of DIC (top) and fluorescence microscopy (bottom) for MBP-AKAP95 (101-210) at 20 µM protein and spiked with Oregon-green-labeled same protein at a molar ratio of 10:1, after treatment with TEV protease for 30 min. The system had 75 mM NaCl in the beginning, and then was adjusted to 150 mM and 300 mM NaCl as indicated by addition of appropriate volume of 5 M NaCl. At the end, equal volume of H_2O was added to the system so that the concentrations of all components including protein and salt were diluted to half (i.e. 150 mM NaCl). Images were taken 5 min after salt adjustment.

(E) Phase contrast images of 50 µM MBP fused to AKAP95 (101-210) in 30 mM NaCl in the absence and presence of 10% of PEG6000 after treatment with TEV protease for 30 min. A reaction containing no AKAP95 (101-210) protein was used as control.

(F) Fusion of two droplets formed by 50 µM MBP fused to AKAP95 (101-210) in 30 mM NaCl and 10% of PEG6000 after treatment with TEV protease for 30 min. Also see Movie S1.

(G) Representative images from differential interference contrast (DIC) (top) and fluorescence microscopy (bottom) of 6.25 µM MBP and MBP fused to full-length AKAP95 in 150 mM NaCl, spiked with Oregon-green-labeled AKAP95 (101-210) at a molar ratio of 150:1, after treatment with TEV protease for 30 min.

See also Figure S3 and Movie S1.

Figure 4. AKAP95 forms dynamic foci in cell nucleus.

(A) Immunostaining of endogenous AKAP95 (red) and DNA (DAPI, blue) in indicated cancer cell lines and primary MEFs from WT and *Akap95* KO embryos.

(B) HeLa cells were transfected with AKAP95-GFP, and two nuclei were imaged at different time points. Time 0 was 24 hr after transfection. Note the growth and merge of the foci, especially those in the red circle.

(C) Immunostaining of endogenous AKAP95 (red) and DNA (DAPI, blue) in HeLa cells untreated (control) or treated with indicated aliphatic alcohol.

(D) Confocal microscopy images of AKAP95 WT or indicated mutants fused to GFP in nuclei following transfection into HeLa cells. These images are from FRAP assays for (F) and (G) and red arrows point to the representative foci that were photobleached in FRAP.

(E) Rapid fusion of AKAP95 (ZF^{C-S})-GFP foci in a HeLa cell nucleus. The white oval and arrow show two different fusion events. These images are from movie S2.

(F and G) FRAP assays. Shown are confocal microscopy images at indicated time points (0 was photobleach) for AKAP95 WT (F), and FRAP recovery curves for WT or indicated mutants as average of 8-12 foci from 8-12 distinct cells ± SD (G). The characteristic half recovery time for each was indicated. Also see Movie S3.

(H) Fluorescence microscopy images of HeLa cells transiently expressing AKAP95 WT or ∆(101-210 fused to GFP.

See also Figure S4 and Movies S2 and S3.

Figure 5. AKAP95 condensation requires Tyrosine in 101-210 and regulates splicing.

(A) Alignment of human and mouse AKAP95 (101-210). Middle row shows identical residues (by letter) and conservative mutations (by “+”). Tyr (Y) is in red font, and Phe (F) is in blue and tall font. Boxes show the Tyr and Phe swapping between human and mouse.

(B) MBP alone (none) or MBP-AKAP95 (101-210) WT, YA, YF, or YS mutations, all at 50 μM protein and in 30 mM NaCl, were treated with TEV protease for 30’ at room temperature. Turbidity of each reaction was shown in pictures, and also by OD600 and plotted in the bar graph as average ± SD from 4 independent assays. Samples were then taken after mixing (indicated as “mixed”) and from supernatant after centrifugation, resolved on a SDS-PAGE gel followed by coomassie blue staining. Compare the abundance of 101-210 in the supernatant fraction after centrifugation relative to the total (as in “mixed”) across all samples, while the cleaved MBP serves as a control.

(C) Representative images of DIC (top) and fluorescence microscopy (bottom) for MBP-AKAP95 (101-210) WT, YA, YS, and YS, all at 50 μM protein and in 30 mM NaCl, and spiked with Oregon-green-labeled (101-210) WT at a molar ratio of 150:1, after treatment with TEV protease for 30 min.

(D) Fluorescence microscopy images of HeLa cells transfected with (top) and Flp-In T-Rex 293 cell lines expressing (bottom) GFP fusions with full-length AKAP95 WT or mutants. YA, YS, YF were full-length constructs in which all Tyr residues in 101-210 were mutated to Ala, Ser, and Phe, respectively.

(E and H) HEK 293 cells co-transfected with indicated siRNAs and plasmids were subject to splice reporter assay (top) and immunoblotting with α-AKAP95 or Ponceau S staining (bottom). The Y axis indicates relative splicing efficiency. A non-targeting siRNA was used as control. Δ = Δ(101-210). Average ± SD from 8 [except 5 for Δ(101-210)] independent transfections are plotted in (E) and 6 independent transfections in (H). WT was included in two copies in each transfection in (E) for corroboration.

(F) Schematic of AKAP95 chimeras, in which the 101-210 region was replaced with IDRs from 4 different proteins shown in the table (bottom).

(G) Representative fluorescence microscopy images of 293T cells transfected with indicated AKAP95 chimeras fused to GFP at the C-terminus.

$^{**}P < 0.01$, $^{***}P < 0.001$ by Student's t test for (B) and by one-way ANOVA followed by Tukey's post hoc test for (E) and (H).

See also Figure S5.

Figure 6. YF mutation enhances AKAP95 condensation propensity and shifts condensates towards a more solid-like state.

(A) MBP-fused to AKAP95 (101-210) WT, YS, and YF all at 50 µM of protein and in 150 mM NaCl were subject to the TEV protease-mediated cleavage. Turbidity at different time point after protease addition was monitored by OD450 using a plate reader. Broken lines show half of the maximum turbidity and the time ($\tau_{1/2}$) it took to reach that level for WT and YF. Plotted were average ± SD of readings after subtraction of that of 50 µM MBP at each time point (which was constant at around 0.07-0.08) from 3 independent assays.

(B) Representative fluorescence microscopy images of Oregon-green-labeled AKAP95 (101-210) WT and YF at increasing concentrations of protein and NaCl after treatment with TEV protease for 30 min. Throughout this figure, Oregon-green-labeled proteins are indicated by a superscripted "OG".

(C) Representative fluorescence microscopy images of AKAP95 (101-210) WT and YF at 50 µM protein and in 30 mM NaCl, both spiked with Oregon-green-labeled (101-210) WT at a molar ratio of 150:1, after treatment with TEV protease for indicated time.

(D) FRAP of Oregon-green-labeled AKAP95 (101-210) WT or YF that were spiked at a molar ratio of 1: 150 into unlabeled AKAP95 (101-210) YF droplets. Left panels are representative fluorescence microscopy images of droplets at indicated time points. Middle panels show FRAP recovery curves as an average of 7-8 droplets ± SD. Right panel shows average recovery of 7-8 droplets ± SD at the final time point on the recovery curves.

(E) FRAP of Oregon-green-labeled AKAP95 (101-210) WT that was spiked at a molar ratio of 1: 150 into unlabeled AKAP95 (101-210) WT or YF droplets. Shown are recovery curves as an average of 12-14 droplets ± SD. The characteristic half recovery time for each was indicated on top. Note that although we did not directly compare dynamics of the labeled 101-210 (WT) and 101-210 (YF) in their own matrix in the same FRAP assay, it is clear from (D) and (E) that the following dynamicity comparison is true: WT-WT^{OG} > YF-WT^{OG} > YF-YF^{OG}.

(F) FRAP of Full-length AKAP95 WT and YF fused to GFP in nuclei following transfection into HeLa cells. Left panels are representative fluorescence microscopy images of foci in one nucleus at indicated time points. The photobleached focus was boxed with white broken line and also amplified in the box on the top left corner. Middle panel shows FRAP recovery curves as average of 9-10 foci from 9-10 distinct cells ± SD. The characteristic half recovery time for each was indicated on top. Right panel shows average recovery of 9-10 from 9-10 distinct cells ± SD at the final time point on the recovery curves.

**P < 0.01, ***P < 0.001 by Student’s t test.

See also Figure S6.

Figure 7. Regulation of tumorigenesis and gene expression by AKAP95 requires its condensation with appropriate material properties.

(A-F) MDA-MB-231 cells were virally infected to stably express control or AKAP95 shRNA #1 (KD, against 3’UTR) as well as indicated constructs including empty vector (vec) and FLAG-HA-tagged full-length AKAP95 WT or mutants with YS or YF mutations in 101-210.

(A) Immunoblotting of total cell lysates with indicated antibodies.

(B) Colony formation assays. Left, the number of colonies were quantified and plotted as average ± SD from 3 biological repeats. Right, representative images of cells stained with crystal violet.

(C) Growth curves of cells in culture. Assays were performed in a total of 5 independent experiments. Plotted are average ± SD from 3 experiments. The other 2 experiments were counted at different days and are plotted and shown in Figure S7A. Statistical analysis are between indicated sample and KD rescued with WT (KD-WT).

(D) Relative mRNA level of *SMAD6* as determined by RT-qPCR and normalized to *GAPDH*, and plotted as average ± SD from 3 biological repeats.

(E) RT-PCR assays for the splicing of the first intron of *CCNA2* pre-mRNA in indicated cells. Following quantification of band intensities by the ImageJ program, the ratio of the PCR product for intron 1-retained transcript to that for intron 1-spliced transcript was calculated and plotted as average ± SD from 3 biological repeats. No signal was detected in any samples when the reverse transcriptase was omitted (data not shown).

(F) RT-PCR assays for the inclusion of the alternative exon on RPUSD3 in indicated cells. Following quantification of band intensities by the ImageJ program, the ratio of the PCR product for exon-included transcript to that for exon-skipped transcript was calculated and shown as 'Inc/skp' on the Y axis. Average ± SD from 3 biological repeats are plotted.

(G-K) MYC-transduced *Akap95* KO MEFs were virally infected with empty vector (vec) or constructs expressing HA-tagged full-length human AKAP95 WT or mutants with YS or YF mutations in 101-210.

(G) Immunoblotting of total cell lysates with indicated antibodies. Two different biological repeats (I and II) are shown, where the mutant expression was modestly higher (in repeat I) or lower (in repeat II) than the WT, and both repeats had similar biological effects. RNA Polymerase II subunit Rpb1 (Pol II) and Gapdh were blotted as loading controls. There is a feint band at the bottom of the AKAP95 blots in all lanes, possibly representing a cross-reactive species.

(H) Left bar graph, percentage of SA-beta-gal positive cells is presented as average ± SD from MEFs derived from two different embryos each. Right images, representative results of SA-beta-galactosidase staining of the stably infected MEFs.

(I) Relative mRNA level of indicated genes as determined by RT-qPCR and normalized to *Gapdh*, and plotted as average ± SD from 3 experiments using MEFs derived from two different embryos each. All these genes are known to be involved in cell proliferation and related functions as indicated at the bottom. For each gene: * $P<0.05$ or ** $P<0.01$ between vec and WT, WT and YS, WT and YF, except for Plk1, for which $P<0.01$ between vec and WT, WT and YF, but not significant between WT and YS.

(J) Heat map showing relative alternative splicing of genes with increase or decrease in PSI in MYC-transduced KO MEFs (from two embryos for each) stably expressing indicated constructs. The complete gene list with detailed information is in Table S2, tab 5.

(K) Sashimi plot showing an example of alternative splicing that was rescued by introduction of AKAP95 WT, but not but the YS or YF mutant. The numbers of exon junction reads and PSI are indicated. Also shown are RT-PCR assays for the inclusion of the alternative exon and the associated quantification. Average ± SD from 2 biological repeats are plotted.

(L) A diagram showing the impact of the different material properties of the AKAP95 WT and mutants on the activities in gene regulation and tumorigenesis. The box with broken line shows the proper window of the material properties of AKAP95 that supports tumorigenesis.

*P<0.05, **P<0.01, and ***P<0.001 by Student's t-test for (C) and by one-way ANOVA followed by Tukey's post hoc test for all other analyses.

See also Figure S7 and Table S2.

Supplemental Figure Legends

Figure S1. AKAP95 regulates cancer cell growth partially through splice control of key genes. Related to Figure 1.

(A) Alteration of AKAP95 (AKAP8) and its correlation with survival in a total of 232 Uterine corpus endometrioid carcinoma patients/samples. From cBioPortal. In the top graph, each small box represents a patient/sample, and 15% of these patients/samples have indicated types of alterations of AKAP95. The graph at the bottom shows the Disease-free survival curves of patients with or without AKAP95 alterations.

(B) Assays for cell proliferation by BrdU incorporation (top) and apoptosis by Annexin V staining (bottom) for control and AKAP95-KD MDA-MB-231 cells. Representative images of flow cytometry results are shown (left), and percentages of cells positive for BrdU (top plot) or Annexin V (bottom plot) are quantified and shown as average ± SD from 3 independent KD assays.

(C) AKAP95 KD inhibited colony formation of MCF7 cells, an estrogen-receptor-positive breast cancer cell line. MCF7 cells were virally infected to stably express scramble control shRNA or two different shRNAs against AKAP95. Bottom, representative images of indicated cell colonies stained with crystal violet. Top, cell numbers were quantified and presented in the bar graph as average ± SD from three independent experiments.

(D) MDA-MB-231 cells were virally infected to stably express scramble (control) or AKAP95 shRNA #1 (KD) as well as indicated constructs including empty vector (vec) and HA-tagged AKAP95. Left, immunoblotting of total cell lysates with indicated antibodies. Middle, Representative images of these cells seeded at high (5×10^4 cells/well in 6-well plate, top) and low (400 cells/well in 24-well plate, bottom) densities and stained with crystal violet. Right, cell numbers were quantified (seeded at high densities) and plotted as average ± SD from three independent experiments.

(E) Top 10 gene sets enriched in genes down- (left) and up- (right) regulated by AKAP95 KD in MDA-MB-231 cells. NES, normalized enrichment score.

(F) AKAP95 KD selectively reduced *CCNA2* expression in MDA-MB-231 cells. Left, relative mRNA levels of indicated cyclins were determined by RT-qPCR and normalized to *GAPDH*, and presented as average ± SD from 3 biological repeats. Right, total cell lysates were used in immunoblotting with antibody for Cyclin (unspecific for Cyclin A1/A2) and Ponceau S staining.

(G) Co-overexpression of *AKAP95* and *CCNA2* in breast cancer tissues of 82 TNBC patients. Top, In the top graph, each small box represents a patient/sample (same sample at each vertical position for both genes), and 12% of these patients/samples have indicated types of alterations of *CCNA2*. The graph at the bottom shows a quantitative correlation of *AKAP95* and *CCNA2* mRNA levels in the TNBC patients. Both from cBioPortal.

(H) CCNA2 is important for MDA-MB-231 cell growth. Cells were virally infected to stably express scramble control shRNA or two different shRNAs against *CCNA2*. Top, immunoblotting of total cell lysates with indicated antibodies. Middle, colony numbers were quantified and presented in a bar graph as average ± SD from three independent experiments. Bottom, representative images of indicated cells stained with crystal violet.

(I) Growth of AKAP95-KD cancer cells was partially rescued by CCNA2 restoration. MDA-MB-231 cells stably expressing scramble (control) or AKAP95 shRNA were transiently transfected with empty vector (vec) or *CCNA2*-expressing construct. Top, immunoblotting of total cell lysates with indicated antibodies. Middle, cell numbers were quantified and plotted as average ± SD from 2 experiments. Bottom, representative images of indicated cells stained with crystal violet.

(J) RIP-seq profiles showing AKAP95 binding to *CCNA2* pre-mRNA. Track information is the same as in Figure 1I. Red arrows show AKAP95-binding sites at intron 1.

(K) AKAP95 KD preferentially reduces junction of exons 1-2. Top, mRNA-seq profiles (by IGV) for *CCNA2* in control 293 cells or 293 cells of AKAP95 KD by two different shRNAs that we previously performed (Hu et al., 2016). The numbers of exon junction reads are indicated. The red asterisk at the gene diagram indicates a stop codon (TAG, also shown in the sequence below) 57 bp downstream of exon 1 in the intron. Note the RIP-seq in (J) and mRNA-seq here are exactly aligned. The number of reads for the junction between exons 1 and 2, and for the average neighboring exons, as well as their ratios are shown in the tables below for 293 cells and also for MDA-MB-231 cells. Note that the existence of the intron 1-retaining pre-mRNA is the reason for the reduced ratio of exon 1-2 over average, and that the samples were from cells without treatment of NMD-blocking reagents and thus some of these aberrant pre-mRNA molecules were probably already decayed.

(L) Total RNAs were used for RT-PCR for intron 1 region in control and AKAP95-KD MDA-MB-231 cells treated with or without cycloheximide (known to block NMD) for 6 hours. PCR products were resolved on an agarose gel. No signal was detected when reverse transcriptase was omitted (data not shown).

(M and N) Same assay as in L except the cells were transfected with control siRNA, or siRNAs for UPF1 or BTZ, and not treated with cycloheximide. (M) Left, mRNA levels of *UPF* in UPF1-KD samples and *BTZ* in BTZ-KD samples, respectively, each relative to the control samples, as determined by RT-qPCR and normalized to *GAPDH*; Right, relative ratios of the signal for the intron 1- retaining transcript over the intron 1-spliced transcript were quantified. Both plots show average ± SD from 2 experiments. (N) Representative results showing the PCR products resolved on an agarose gel. No signal was detected when reverse transcriptase was omitted (- RT). The asterisk next to the gel indicates an unknown amplification product that occasionally appeared in our reactions.

(O) Relative expression level of TGF-β pathway genes based on RNA-seq reads from control and AKAP95-KD MDA-MB-231 cells expressing vector or AKAP95. The Venn diagram shows numbers of TGF-β pathway genes (from GSEA) downregulated by AKAP95 KD and upregulated by rescue with AKAP95 expression, and the 16 overlapped genes in both categories are selected to show their relative expression in the plot. *SMAD6* gene was in red box as a gene substantially downregulated by KD and upregulated by the rescue.

(P) RIP-seq profiles showing AKAP95 binding to *RPUSD3* and *PPM1K* pre-mRNAs. Track information is the same as in (J). Red circles on the gene diagrams indicate the alternatively included exons (corresponding to the middle exon in the gene diagrams in (Q), and red boxes show AKAP95 binding at the introns flanking these exons.

(Q) Sashimi plots showing that the alternative splicing of *RPUSD3* and *PPM1K* pre-mRNAs was affected by AKAP95 KD and rescued by restored expression of AKAP95. The numbers of exon junction reads and PSI are indicated.

*P < 0.05, **P < 0.01, ***P < 0.001, by log-rank test for (A) and by one-way ANOVA followed by Tukey's post hoc test for (M) and by Student's t-test for all other analyses.

Figure S2. Akap95 is required for transformation and overcoming oncogene-induced cellular senescence. Related to Figure 2.

(A) Schematic of the "Knockout-first" *Akap95* (also called *Akap8*) allele. This allele is a null allele ("-") without any further recombination.

(B) MEFs were derived from mouse embryos. Images of six embryos from the same litter were shown at the top, sequentially followed with the genotyping results by genomic PCR, Ponceau S staining and α-AKAP95 immunoblotting of the total lysates of the MEFs derived from each embryo, and the concluded genotype at the bottom.

(C) Top 10 gene sets enriched in genes down- (left) and up- (right) regulated in the MYC-transduced KO MEFs compared to the MYC-transduced Het MEFs.

(D) MEFs from all 6 littermate embryos with indicated genotypes were transduced with MYC virus. Shown are representative images of cells before (top row) and after MYC transduction (middle row), and SA-beta-galactosidase staining after MYC transduction (bottom).

(E) Rescue of the gene expression profile by introduction of human AKAP95 into the MYC-transduced KO MEFs as shown by immunoblotting with indicated antibodies (left) and heat map (right) showing relative expression levels of genes that were down- or up-regulated in the indicated cells. The complete gene list with detailed information is in Table S2, tab 2.

(F) Heat map showing relative alternative splicing of genes clustered by increase or decrease in PSI in MYC-transduced Het and KO MEFs from two embryos for each. The complete gene list with detailed information is in Table S2, tab 3. Right, Sashimi plots showing alternative splicing changes for each gene cluster from the heat map using two examples, Asb7 for cluster 1, and Xpo4 for cluster 2. Bottom, gene ontology analysis for each gene cluster in the heat map.

Figure S3. AKAP95 phase separation in vitro. Related to Figure 3.

(A) 293T cells were transfected with either empty vector (vec), or indicated AKAP95 construct with FLAG-HA-tag. Following α-Flag IP, the pulldown proteins were boiled and resolved by SDS-PAGE and detected by immunoblotting with α-HA. Shown are images of high and low exposure as indicated. Blue and red asterisks indicate monomer and dimer, respectively. The doubling of molecular weight of the species with red asterisk for every construct with varying size indicates that they are true dimers instead of cross-reactive proteins.

(B) Identification of 1-100 as a probable prion subsequence on AKAP95. By the PLAAC program (http://plaac.wi.mit.edu/), using homo sapiens as background and core length of 30.

(C) Purified MBP and MBP fused to AKAP95 truncations as indicated (amino acid number) or full-length AKAP95 (1-692) were resolved on SDS-PAGE and stained with Coomassie blue.

(D) Another event of fusion of two droplets formed by 50 μM MBP-AKAP95 (101-210) in 30 mM NaCl and 10% of PEG6000 after treatment with TEV protease for 30 min. Also see Movie S1.

Figure S4. AKAP95 partially localizes in nuclear speckles. Related to Figure 4.

(A) Immunoblotting with indicated antibodies using total lysates of 293 cells expressing indicated AKAP95-GFP fusion constructs. Parental 293 cell lysate was used as control.

(B) Fluorescence microscopy images of HeLa cells transiently expressing AKAP95-GFP. DAPI was used to stain the nucleus, and nuclear speckles are identified by an α-SRSF2 antibody. Right, quantification of the signal intensity of indicated molecules across the dotted lines shown in the images. 10 units = 1 μm. Quantification by Image J.

Figure S5. AKAP95 condensation requires Tyrosine in 101-210 and regulates splicing. Related to Figure 5.

(A) Analysis of amino acid enrichment for AKAP95 (101-210). Flexibility (left) and bulkiness (right) of each amino acid is also indicated by color. By Composition Profiler (http://www.cprofiler.org/cgi-bin/profiler.cgi), using SwissProt 51 Dataset as the background sample.

(B) Purified MBP fused to AKAP95 (101-210) WT, YS, YA, and YF mutants were resolved on SDS-PAGE and stained with Coomassie blue.

(C) Total lysates from Flp-In T-Rex 293 cell lines induced to express full-length AKAP95 WT or mutants fused to GFP were used for Immunoblotting using indicated α-AKAP95 (top) or GAPDH (bottom). YA, YS, YF were full-length constructs in which all Tyr residues in 101-210 were mutated to Ala, Ser, and Phe, respectively.

(D and E) Indicated full-length AKAP95 WT or mutants fused to GFP were induced by various concentrations of doxycycline on Flp-In T-Rex 293 cell lines. Immunoblotting of total cell lysates with indicated antibodies (D). The doxycycline concentrations in red font activated the transgene at the near endogenous level, and were selected for treating cells and fluorescence microscopy assays of fixed cells in (E). Two different GFP images for each construct are shown and DAPI images are also shown for the GFP image on top (E). Note that the foci can be seen much more clearly on a computer screen than on a printout.

(F) HEK 293 cells were transfected with splice reporter and indicated plasmids, followed by splice reporter assay. The normalized splicing efficiency is shown as average ± SD of 2 independent transfections. Top, immunoblotting of total lysates. Blue arrow shows endogenous AKAP95.

(G) 293T cells transiently expressing indicated constructs with FLAG-HA-tag were used for α-FLAG IP and immunoblotting with indicated antibodies and Ponceau S staining.

(H) Immunoblotting of 293T cells transfected with empty vector or indicated FLAG-HA-tagged AKAP95 chimeras fused to GFP. Bottom, blotted with anti-GAPDH. Top, blotted with anti-AKAP95 antibody (A301-062A from Bethyl Laboratories). As this antibody recognizes an epitope in a region between residue 575 and 625 of human AKAP95, its reactivity is unlikely affected by the replacement of the 101-210 in the AKAP95 chimeras.

*$P < 0.05$, by Student's t-test.

Figure S6. AKAP95 YF condensation in vitro. Related to Figure 6.

(A) Top, representative images of fluorescence microscopy for 10 μM Oregon-green-labeled MBP-AKAP95 (101-210) YF after treatment with TEV protease for 30 min. The system had 30 mM NaCl in the beginning, and then was adjusted to 150 mM and 300 mM NaCl as indicated by addition of appropriate volume of 5 M NaCl. Bottom, representative images of DIC (upper) and fluorescence microscopy (lower) for MBP-AKAP95 (101-210) YF at 20 μM protein and spiked with

Oregon-green-labeled same protein at a molar ratio of 10:1, after treatment with TEV protease for 30 min. The system had 30 mM NaCl in the beginning, and then was adjusted to 75 mM, 150 mM, and 300 mM NaCl as indicated by addition of appropriate volume of 5 M NaCl. At the end, equal volume of H_2O was added to the system so that the concentrations of all components including protein and salt were diluted to half (i.e. 150 mM NaCl). Images were taken 5 min after salt adjustment. The bottom assays were performed side by side with (101-210) WT in Figure 3D. **(B)** Bright field (top) and fluorescence (bottom) microscopy images of ThT-stained FUS (full-length) and AKAP95 (101-210) YF proteins, both at 50 µM of protein and in 30 mM NaCl, 120 min after TEV protease treatment. Note that the AKAP95 in the red circle aggregated to a comparable level to FUS, but still showed no ThT staining.

Figure S7. Regulation of tumorigenesis and gene expression by AKAP95 requires its condensation with appropriate material properties. Related to Figure 7.

(A-C) MDA-MB-231 cells were virally infected to stably express scramble (control) or AKAP95 shRNA #1 (KD, against 3’UTR) as well as indicated constructs including empty vector (vec) and FLAG-HA-tagged full-length AKAP95 WT or mutants with with YS or YF mutations in 101-210.

(A) Growth curves of cells in culture. Assays were performed in a total of 5 independent experiments. Plotted are average ± SD from 2 experiments. The other 3 experiments were counted at different days and are plotted and shown in Figure 7C. Statistical analysis are between indicated sample with KD-WT.

(B) Relative mRNA level of *CCNA2* as determined by RT-qPCR and normalized to *GAPDH*, and plotted for each of the 2 biological repeats individually.

(C) RT-PCR assays for the inclusion of the alternative exon on *PPM1K* in indicated cells. Following quantification of band intensities by the ImageJ program, the ratio of the PCR product for exon-included transcript to that for exon-skipped transcript was calculated and shown as ‘Inc/skp’ on the Y axis. Average ± SD from 3 biological repeats are plotted.

(D-G) MYC-transduced *Akap95* KO MEFs were virally infected to stably express indicated rescue constructs including empty vector (vec) and HA-tagged full-length human AKAP95 WT or mutants with YS or YF mutations in 101-210.

(D) Heat map showing relative expression levels of genes that were down- or up-regulated in MYC-transduced KO MEFs (from two embryos for each) stably expressing indicated rescue constructs. The complete gene list with detailed information is in Table S2, tab 4.

(E) Relative mRNA levels of indicated SASP genes as determined by RNA-seq reads from 2 biological repeats (KO1 and KO2).

(F and G) Sashimi plots showing example genes for which the alternative exon inclusion was promoted (F) or suppressed (G) by introduction of AKAP95 WT, but not as effectively by the YS or YF mutant. The numbers of exon junction reads and PSI are indicated. Also shown are RT-PCR assays for the inclusion of the alternative exon and the associated quantification. Average ± SD from 2 biological repeats are plotted.

(H) A model for how AKAP95 condensates may regulate gene expression for tumorigenesis. See text for details.

*P<0.05, **P<0.01, and ***P<0.001 by Student's t-test for (A) and by one-way ANOVA followed by Tukey's post hoc test for all other analyses.

Supplemental Table Legends

Table S1. Changes of gene expression and alternative splicing by AKAP95 KD and rescue in TNBC cells

This table contains 2 tabs as explained below:

Tab 1. Gene expression changes by AKAP95 KD and rescue in TNBC cells.

By expression analyses of the RNA-seq results from MDA-MB-231 cells that were virally infected to stably express scramble control shRNA or AKAP95 shRNA (KD) as well as vector or AKAP95 construct. Shown are steps to transform the expression values to generate heat map as described in Materials and Methods.

Tab 2. Changes of gene alternative splicing by AKAP95 KD and rescue in TNBC cells.

By splicing analyses of the RNA-seq results from MDA-MB-231 cells that were virally infected to stably express scramble control shRNA or AKAP95 shRNA (KD) as well as vector or AKAP95 construct.

Table S2. Changes of gene expression and alternative splicing by *Akap95* KO and rescue in MYC-transduced MEFs

This table contains 5 tabs as explained below:

Tab 1. Gene expression changes by *Akap95* KO in MYC-transduced MEFs.

By expression analyses of the RNA-seq results from MYC-transduced *Akap95* Het and KO MEFs derived from 2 embryos for each. Shown are steps to transform the expression values to generate heat map as described in Materials and Methods.

Tab 2. Gene expression changes by *Akap95* KO and rescue in MYC-transduced MEFs.

By expression analyses of the RNA-seq results from MYC-transduced *Akap95* Het, and KO MEFs, and KO MEFs that were introduced with vector or AKAP95 WT.

Tab 3. Changes of gene alternative splicing by *Akap95* KO in MYC-transduced MEFs.

By splicing analyses of the RNA-seq results from MYC-transduced *Akap95* Het and KO MEFs derived from 2 embryos for each.

Tab 4. Gene expression changes by AKAP95 expression in MYC-transduced *Akap95* KO MEFs.

By expression analyses of the RNA-seq results from MYC-transduced *Akap95* KO MEFs (from 2 embryos) that were introduced with vector, AKAP95 WT, YS, or YF mutant.

Tab 5. Changes of gene alternative splicing by AKAP95 expression in MYC-transduced *Akap95* KO MEFs.

By splicing analyses of the RNA-seq results from MYC-transduced *Akap95* KO MEFs (from 2 embryos) that were introduced with vector, AKAP95 WT, YS, or YF mutant.

Table S3. Information for Primers, shRNAs, and siRNAs

Supplemental Movie Legends

Movie S1. AKAP95 droplets in vitro are highly dynamic and can fuse, Related to Figure 3.

Purified MBP-AKAP95 (101-210) formed droplets at 50 µM, in 30 mM NaCl and 10% of PEG6000 after treatment with TEV protease for 30 min. The yellow triangle points to a fusion event of two droplets. Played at 134x speed.

Movie S2. Rapid fusion of AKAP95 foci in the cell nucleus, Related to Figure 4.

Full-length AKAP95 ($ZF^{C\text{-}S}$)-GFP foci in a HeLa cell nucleus following transfection. The arrows point to two different fusion events. Played at 20x speed.

Movies S3. FRAP assays for intracellular AKAP95, Related to Figure 4.

Representative FRAP assays for AKAP95 WT, 101-692, and $ZF^{C\text{-}S}$, all fused to GFP and transfected into HeLa cells. Played at 20x speed.

REFERENCES

Akileswaran, L., Taraska, J.W., Sayer, J.A., Gettemy, J.M., and Coghlan, V.M. (2001). A-kinase-anchoring protein AKAP95 is targeted to the nuclear matrix and associates with p68 RNA helicase. J Biol Chem *276*, 17448-17454.

Alberti, S., Gladfelter, A., and Mittag, T. (2019). Considerations and Challenges in Studying Liquid-Liquid Phase Separation and Biomolecular Condensates. Cell *176*, 419-434.

Alberti, S., Halfmann, R., King, O., Kapila, A., and Lindquist, S. (2009). A systematic survey identifies prions and illuminates sequence features of prionogenic proteins. Cell *137*, 146-158.

Banani, S.F., Lee, H.O., Hyman, A.A., and Rosen, M.K. (2017). Biomolecular condensates: organizers of cellular biochemistry. Nature reviews Molecular cell biology *18*, 285-298.

Boija, A., Klein, I.A., Sabari, B.R., Dall'Agnese, A., Coffey, E.L., Zamudio, A.V., Li, C.H., Shrinivas, K., Manteiga, J.C., Hannett, N.M.*, et al.* (2018). Transcription Factors Activate Genes through the Phase-Separation Capacity of Their Activation Domains. Cell *175*, 1842-1855.e1816.

Bomar, J., Moreira, P., Balise, J.J., and Collas, P. (2002). Differential regulation of maternal and paternal chromosome condensation in mitotic zygotes. J Cell Sci *115*, 2931-2940.

Boulay, G., Sandoval, G.J., Riggi, N., Iyer, S., Buisson, R., Naigles, B., Awad, M.E., Rengarajan, S., Volorio, A., McBride, M.J.*, et al.* (2017). Cancer-Specific Retargeting of BAF Complexes by a Prion-like Domain. Cell *171*, 163-178.e119.

Bradner, J.E., Hnisz, D., and Young, R.A. (2017). Transcriptional Addiction in Cancer. Cell *168*, 629-643.

Cao, Y., and Li, Z. (2016). Contribution of genomic copy-number variations in prenatal oral clefts: a multicenter cohort study. Genetics in medicine : official journal of the American College of Medical Genetics *18*, 1052-1055.

Castello, A., Fischer, B., Eichelbaum, K., Horos, R., Beckmann, B.M., Strein, C., Davey, N.E., Humphreys, D.T., Preiss, T., Steinmetz, L.M.*, et al.* (2012). Insights into RNA biology from an atlas of mammalian mRNA-binding proteins. Cell *149*, 1393-1406.

Chen, X., Kong, X., Zhuang, W., Teng, B., Yu, X., Hua, S., Wang, S., Liang, F., Ma, D., Zhang, S.*, et al.* (2016). Dynamic changes in protein interaction between AKAP95 and Cx43 during cell cycle progression of A549 cells. Scientific reports *6*, 21224.

Cho, W.K., Jayanth, N., English, B.P., Inoue, T., Andrews, J.O., Conway, W., Grimm, J.B., Spille, J.H., Lavis, L.D., Lionnet, T.*, et al.* (2016). RNA Polymerase II cluster dynamics predict mRNA output in living cells. eLife *5:e13617*.

Chong, S., Dugast-Darzacq, C., Liu, Z., Dong, P., Dailey, G.M., Cattoglio, C., Heckert, A., Banala, S., Lavis, L., Darzacq, X.*, et al.* (2018). Imaging dynamic and selective low-complexity domain interactions that control gene transcription. Science (New York, NY) *361*.

Collas, P., Le Guellec, K., and Tasken, K. (1999). The A-kinase-anchoring protein AKAP95 is a multivalent protein with a key role in chromatin condensation at mitosis. J Cell Biol *147*, 1167-1180.

Coppe, J.P., Patil, C.K., Rodier, F., Sun, Y., Munoz, D.P., Goldstein, J., Nelson, P.S., Desprez, P.Y., and Campisi, J. (2008). Senescence-associated secretory phenotypes reveal cellnonautonomous functions of oncogenic RAS and the p53 tumor suppressor. PLoS biology *6*, 2853-2868.

Courchaine, E.M., Lu, A., and Neugebauer, K.M. (2016). Droplet organelles? The EMBO journal *35*, 1603-1612.

David, C.J., and Manley, J.L. (2010). Alternative pre-mRNA splicing regulation in cancer: pathways and programs unhinged. Genes & development *24*, 2343-2364.

David, C.J., and Massague, J. (2018). Contextual determinants of TGFbeta action in development, immunity and cancer. Nature reviews Molecular cell biology *19*, 419-435.

Eide, T., Carlson, C., Tasken, K.A., Hirano, T., Tasken, K., and Collas, P. (2002). Distinct but overlapping domains of AKAP95 are implicated in chromosome condensation and condensin targeting. EMBO Rep *3*, 426-432.

Eide, T., Coghlan, V., Orstavik, S., Holsve, C., Solberg, R., Skalhegg, B.S., Lamb, N.J., Langeberg, L., Fernandez, A., Scott, J.D.*, et al.* (1998). Molecular cloning, chromosomal localization, and cell cycle-dependent subcellular distribution of the A-kinase anchoring protein, AKAP95. Exp Cell Res *238*, 305-316.

Eide, T., Tasken, K.A., Carlson, C., Williams, G., Jahnsen, T., Tasken, K., and Collas, P. (2003). Protein kinase A-anchoring protein AKAP95 interacts with MCM2, a regulator of DNA replication. J Biol Chem *278*, 26750-26756.

Fridman, A.L., and Tainsky, M.A. (2008). Critical pathways in cellular senescence and immortalization revealed by gene expression profiling. Oncogene *27*, 5975-5987.

Fu, X.D., and Ares, M., Jr. (2014). Context-dependent control of alternative splicing by RNA-binding proteins. Nature reviews Genetics *15*, 689-701.

Gueroussov, S., Weatheritt, R.J., O'Hanlon, D., Lin, Z.Y., Narula, A., Gingras, A.C., and Blencowe, B.J. (2017). Regulatory Expansion in Mammals of Multivalent hnRNP Assemblies that Globally Control Alternative Splicing. Cell *170*, 324-339.e323.

Hnisz, D., Shrinivas, K., Young, R.A., Chakraborty, A.K., and Sharp, P.A. (2017). A Phase Separation Model for Transcriptional Control. Cell *169*, 13-23.

Hsu, T.Y., Simon, L.M., Neill, N.J., Marcotte, R., Sayad, A., Bland, C.S., Echeverria, G.V., Sun, T., Kurley, S.J., Tyagi, S.*, et al.* (2015). The spliceosome is a therapeutic vulnerability in MYC-driven cancer. Nature *525*, 384-388.

Hu, J., Khodadadi-Jamayran, A., Mao, M., Shah, K., Yang, Z., Nasim, M.T., Wang, Z., and Jiang, H. (2016). AKAP95 regulates splicing through scaffolding RNAs and RNA processing factors. Nature communications *7*, 13347.

Hug, N., Longman, D., and Caceres, J.F. (2016). Mechanism and regulation of the nonsense-mediated decay pathway. Nucleic acids research *44*, 1483-1495.

Hyman, A.A., Weber, C.A., and Julicher, F. (2014). Liquid-liquid phase separation in biology. Annual review of cell and developmental biology *30*, 39-58.

Imamura, T., Takase, M., Nishihara, A., Oeda, E., Hanai, J., Kawabata, M., and Miyazono, K. (1997). Smad6 inhibits signalling by the TGF-beta superfamily. Nature *389*, 622-626.

Jeon, H.S., Dracheva, T., Yang, S.H., Meerzaman, D., Fukuoka, J., Shakoori, A., Shilo, K., Travis, W.D., and Jen, J. (2008). SMAD6 contributes to patient survival in non-small cell lung cancer and its knockdown reestablishes TGF-beta homeostasis in lung cancer cells. Cancer Res *68*, 9686-9692.

Jiang, H., Lu, X., Shimada, M., Dou, Y., Tang, Z., and Roeder, R.G. (2013). Regulation of transcription by the MLL2 complex and MLL complex-associated AKAP95. Nature structural & molecular biology *20*, 1156-1163.

Jiao, J., Zhang, R., Li, Z., Yin, Y., Fang, X., Ding, X., Cai, Y., Yang, S., Mu, H., Zong, D.*, et al.* (2018). Nuclear Smad6 promotes gliomagenesis by negatively regulating PIAS3-mediated STAT3 inhibition. Nature communications *9*, 2504.

Jungmann, R.A., and Kiryukhina, O. (2005). Cyclic AMP and AKAP-mediated targeting of protein kinase A regulates lactate dehydrogenase subunit A mRNA stability. J Biol Chem *280*, 25170-25177.

Kato, M., Han, T.W., Xie, S., Shi, K., Du, X., Wu, L.C., Mirzaei, H., Goldsmith, E.J., Longgood, J., Pei, J.*, et al.* (2012). Cell-free formation of RNA granules: low complexity sequence domains form dynamic fibers within hydrogels. Cell *149*, 753-767.

Katz, Y., Wang, E.T., Airoldi, E.M., and Burge, C.B. (2010). Analysis and design of RNA sequencing experiments for identifying isoform regulation. Nature methods *7*, 1009-1015.

Kim, H.J., Kim, N.C., Wang, Y.D., Scarborough, E.A., Moore, J., Diaz, Z., MacLea, K.S., Freibaum, B., Li, S., Molliex, A.*, et al.* (2013). Mutations in prion-like domains in hnRNPA2B1 and hnRNPA1 cause multisystem proteinopathy and ALS. Nature *495*, 467-473.

Koh, C.M., Bezzi, M., Low, D.H., Ang, W.X., Teo, S.X., Gay, F.P., Al-Haddawi, M., Tan, S.Y., Osato, M., Sabo, A.*, et al.* (2015). MYC regulates the core pre-mRNA splicing machinery as an essential step in lymphomagenesis. Nature *523*, 96-100.

Kress, T.R., Sabo, A., and Amati, B. (2015). MYC: connecting selective transcriptional control to global RNA production. Nature reviews Cancer *15*, 593-607.

Kroschwald, S., Maharana, S., and Simon, A. (2017). Hexanediol: A chemical probe to investigate the material properties of membrane-less compartments. Matters *10.19185/matters.201702000010*.

Kuilman, T., and Peeper, D.S. (2009). Senescence-messaging secretome: SMS-ing cellular stress. Nature reviews Cancer *9*, 81-94.

Kwon, I., Kato, M., Xiang, S., Wu, L., Theodoropoulos, P., Mirzaei, H., Han, T., Xie, S., Corden, J.L., and McKnight, S.L. (2013). Phosphorylation-regulated binding of RNA polymerase II to fibrous polymers of low-complexity domains. Cell *155*, 1049-1060.

Langdon, E.M., Qiu, Y., Ghanbari Niaki, A., McLaughlin, G.A., Weidmann, C.A., Gerbich, T.M., Smith, J.A., Crutchley, J.M., Termini, C.M., Weeks, K.M.*, et al.* (2018). mRNA structure determines specificity of a polyQ-driven phase separation. Science (New York, NY) *360*, 922-927.

Li, Y., Kao, G.D., Garcia, B.A., Shabanowitz, J., Hunt, D.F., Qin, J., Phelan, C., and Lazar, M.A. (2006). A novel histone deacetylase pathway regulates mitosis by modulating Aurora B kinase activity. Genes Dev *20*, 2566-2579.

Lin, Y., Protter, D.S., Rosen, M.K., and Parker, R. (2015). Formation and Maturation of Phase-Separated Liquid Droplets by RNA-Binding Proteins. Molecular cell *60*, 208-219.

Liu, W., Hua, S., Dai, Y., Yuan, Y., Yang, J., Deng, J., Huo, Y., Chen, X., Teng, B., Yu, X.*, et al.* (2015). Roles of Cx43 and AKAP95 in ovarian cancer tissues in G1/S phase. International journal of clinical and experimental pathology *8*, 14315-14324.

Lu, H., Yu, D., Hansen, A.S., Ganguly, S., Liu, R., Heckert, A., Darzacq, X., and Zhou, Q. (2018). Phase-separation mechanism for C-terminal hyperphosphorylation of RNA polymerase II. Nature *558*, 318-323.

Luo, J., Solimini, N.L., and Elledge, S.J. (2009). Principles of cancer therapy: oncogene and non-oncogene addiction. Cell *136*, 823-837.

Maharana, S., Wang, J., Papadopoulos, D.K., Richter, D., Pozniakovsky, A., Poser, I., Bickle, M., Rizk, S., Guillen-Boixet, J., Franzmann, T.M.*, et al.* (2018). RNA buffers the phase separation behavior of prion-like RNA binding proteins. Science (New York, NY) *360*, 918-921.

Molliex, A., Temirov, J., Lee, J., Coughlin, M., Kanagaraj, A.P., Kim, H.J., Mittag, T., and Taylor, J.P. (2015). Phase separation by low complexity domains promotes stress granule assembly and drives pathological fibrillization. Cell *163*, 123-133.

Nasim, M.T., and Eperon, I.C. (2006). A double-reporter splicing assay for determining splicing efficiency in mammalian cells. Nature protocols *1*, 1022-1028.

Nebel, R.A., Kirschen, J., Cai, J., Woo, Y.J., Cherian, K., and Abrahams, B.S. (2015). Reciprocal Relationship between Head Size, an Autism Endophenotype, and Gene Dosage at 19p13.12 Points to AKAP8 and AKAP8L. PLoS One *10*, e0129270.

Pak, C.W., Kosno, M., Holehouse, A.S., Padrick, S.B., Mittal, A., Ali, R., Yunus, A.A., Liu, D.R., Pappu, R.V., and Rosen, M.K. (2016). Sequence Determinants of Intracellular Phase Separation by Complex Coacervation of a Disordered Protein. Molecular cell *63*, 72-85.

Patel, A., Lee, H.O., Jawerth, L., Maharana, S., Jahnel, M., Hein, M.Y., Stoynov, S., Mahamid, J., Saha, S., Franzmann, T.M.*, et al.* (2015). A Liquid-to-Solid Phase Transition of the ALS Protein FUS Accelerated by Disease Mutation. Cell *162*, 1066-1077.

Qi, F., Yuan, Y., Zhi, X., Huang, Q., Chen, Y., Zhuang, W., Zhang, D., Teng, B., Kong, X., and Zhang, Y. (2015). Synergistic effects of AKAP95, Cyclin D1, Cyclin E1, and Cx43 in the development of rectal cancer. International journal of clinical and experimental pathology *8*, 1666-1673.

Ramaswami, M., Taylor, J.P., and Parker, R. (2013). Altered ribostasis: RNA-protein granules in degenerative disorders. Cell *154*, 727-736.

Sabari, B.R., Dall'Agnese, A., Boija, A., Klein, I.A., Coffey, E.L., Shrinivas, K., Abraham, B.J., Hannett, N.M., Zamudio, A.V., Manteiga, J.C.*, et al.* (2018). Coactivator condensation at super-enhancers links phase separation and gene control. Science (New York, NY) *361*.

Schwartz, J.C., Cech, T.R., and Parker, R.R. (2015). Biochemical Properties and Biological Functions of FET Proteins. Annual review of biochemistry *84*, 355-379.

Shin, Y., and Brangwynne, C.P. (2017). Liquid phase condensation in cell physiology and disease. Science (New York, NY) *357*.

Spector, D.L., and Lamond, A.I. (2011). Nuclear speckles. Cold Spring Harbor perspectives in biology *3*.

Wang, J., Choi, J.M., Holehouse, A.S., Lee, H.O., Zhang, X., Jahnel, M., Maharana, S., Lemaitre, R., Pozniakovsky, A., Drechsel, D.*, et al.* (2018). A Molecular Grammar Governing the Driving Forces for Phase Separation of Prion-like RNA Binding Proteins. Cell *174*, 688-699.e616.

Wong, W., and Scott, J.D. (2004). AKAP signalling complexes: focal points in space and time. Nat Rev Mol Cell Biol *5*, 959-970.

Woodruff, J.B., Hyman, A.A., and Boke, E. (2018). Organization and Function of Non-dynamic Biomolecular Condensates. Trends in biochemical sciences *43*, 81-94.

Yang, Y., Mahaffey, C.L., Berube, N., and Frankel, W.N. (2006). Interaction between fidgetin and protein kinase A-anchoring protein AKAP95 is critical for palatogenesis in the mouse. J Biol Chem *281*, 22352-22359.

Yang, Z., Augustin, J., Chang, C., Hu, J., Shah, K., Chang, C.W., Townes, T., and Jiang, H. (2014). The DPY30 subunit in SET1/MLL complexes regulates the proliferation and differentiation of hematopoietic progenitor cells. Blood *124*, 2025-2033.

Yang, Z., Shah, K., Busby, T., Giles, K., Khodadadi-Jamayran, A., Li, W., and Jiang, H. (2018). Hijacking a key chromatin modulator creates epigenetic vulnerability for MYC-driven cancer. The Journal of clinical investigation *128*, 3605-3618.

Ying, Y., Wang, X.J., Vuong, C.K., Lin, C.H., Damianov, A., and Black, D.L. (2017). Splicing Activation by Rbfox Requires Self-Aggregation through Its Tyrosine-Rich Domain. Cell *170*, 312-323.e310.

Figure 1

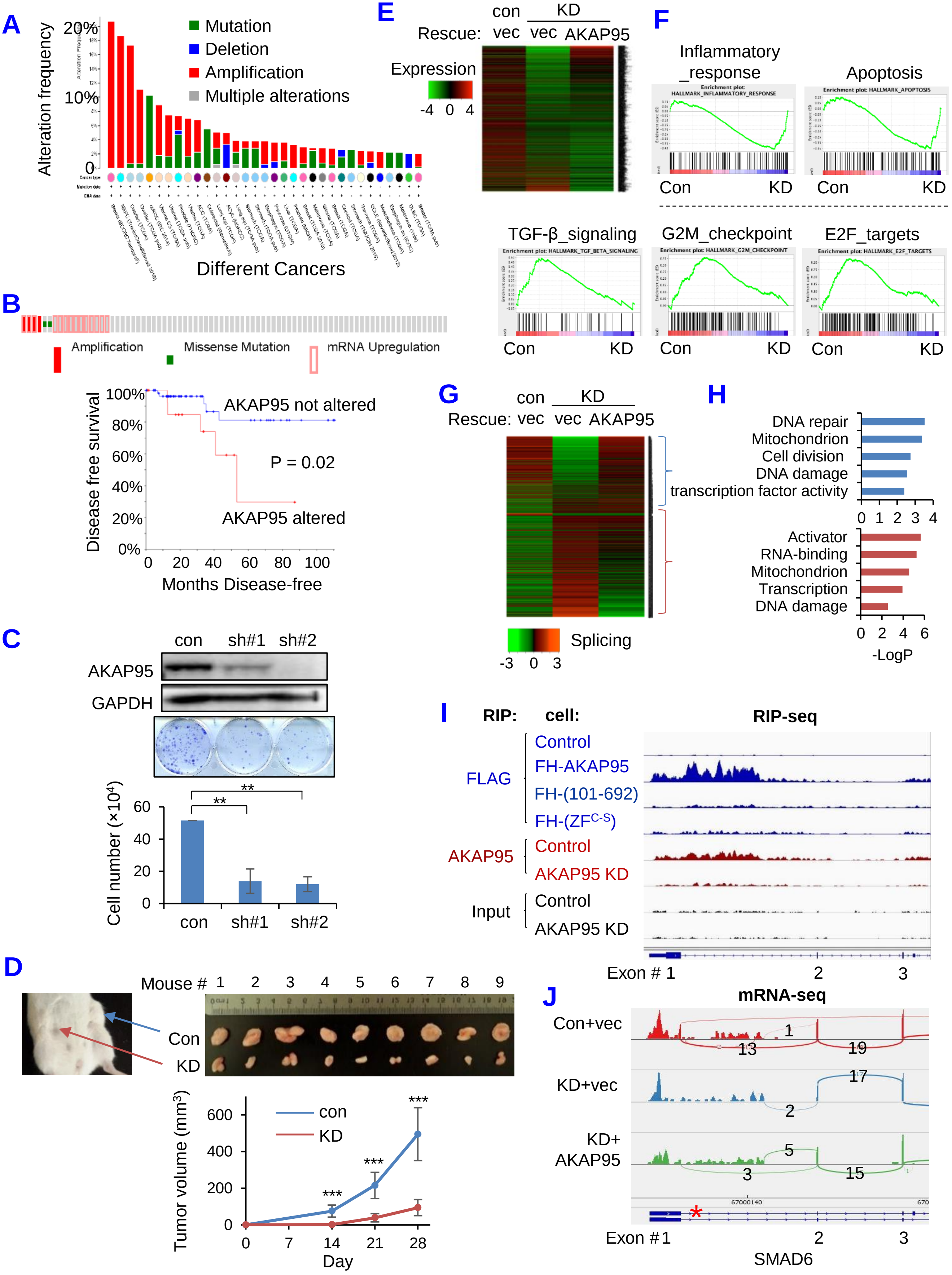
A
Alteration frequency
20%
10%
0
Mutation
Deletion
Amplification
Multiple alterations
Different Cancers
B
Amplification
Missense Mutation
mRNA Upregulation
Disease free survival
100%
80%
60%
40%
20%
0%
AKAP95 not altered
P = 0.02
AKAP95 altered
0 20 40 60 80 100
Months Disease-free
C
con sh#1 sh#2
AKAP95
GAPDH
Cell number (×10⁴)
60
40
20
0
**
**
con sh#1 sh#2
D
Mouse # 1 2 3 4 5 6 7 8 9
Con
KD
Tumor volume (mm³)
600
400
200
0
con
KD
***
***
***
0 7 14 21 28
Day
E
con
KD
Rescue: vec vec AKAP95
Expression
-4 0 4
F
Inflammatory_response
Apoptosis
Con KD
Con KD
TGF-β_signaling
G2M_checkpoint
E2F_targets
Con KD
Con KD
Con KD
G
con
KD
Rescue: vec vec AKAP95
Splicing
-3 0 3
H
DNA repair
Mitochondrion
Cell division
DNA damage
transcription factor activity
0 1 2 3 4
Activator
RNA-binding
Mitochondrion
Transcription
DNA damage
0 2 4 6
-LogP
I
RIP: cell:
RIP-seq
FLAG
Control
FH-AKAP95
FH-(101-692)
FH-(ZF^C-S)
AKAP95
Control
AKAP95 KD
Input
Control
AKAP95 KD
Exon # 1 2 3
J
mRNA-seq
Con+vec
1
13
19
KD+vec
17
2
KD+ AKAP95
5
3
15
67000140
*
Exon #1 2 3
SMAD6

Figure 2

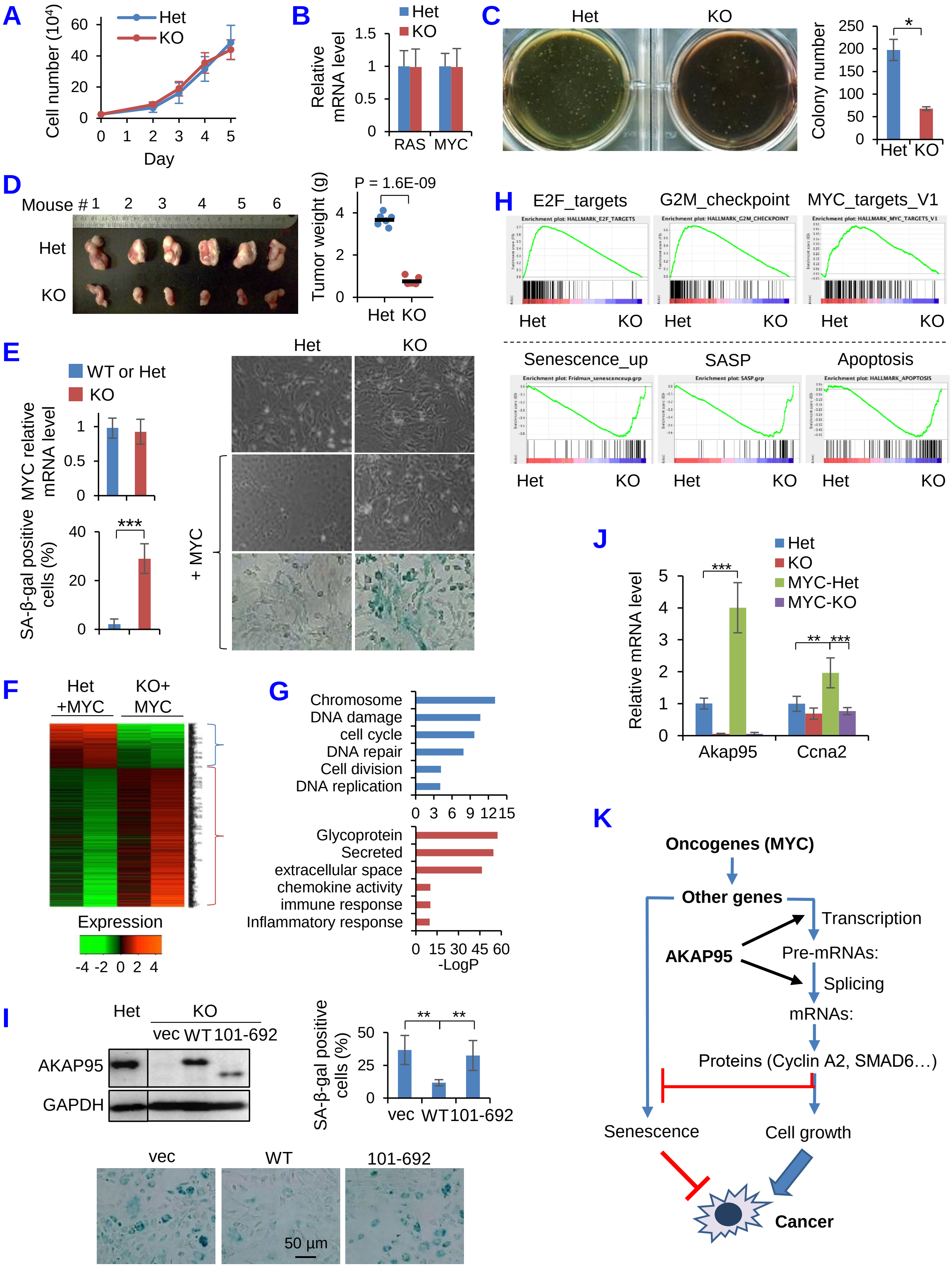
A
Cell number (10^4)
60
40
20
0
Het
KO
0 1 2 3 4 5
Day
B
Het
KO
Relative mRNA level
1.5
1
0.5
0
RAS
MYC
C
Het
KO
Colony number
250
200
150
100
50
0
*
Het KO
D
Mouse # 1 2 3 4 5 6
Het
KO
Tumor weight (g)
P = 1.6E-09
4
2
0
Het KO
E
WT or Het
KO
MYC relative mRNA level
1
0.5
0
SA-β-gal positive cells (%)
40
20
0
***
Het
KO
+ MYC
F
Het +MYC
KO+ MYC
Expression
-4 -2 0 2 4
G
Chromosome
DNA damage
cell cycle
DNA repair
Cell division
DNA replication
0 3 6 9 12 15
Glycoprotein
Secreted
extracellular space
chemokine activity
immune response
Inflammatory response
0 15 30 45 60
-LogP
H
E2F_targets
G2M_checkpoint
MYC_targets_V1
Enrichment plot: HALLMARK_E2F_TARGETS
Enrichment plot: HALLMARK_G2M_CHECKPOINT
Enrichment plot: HALLMARK_MYC_TARGETS_V1
Het KO
Het KO
Het KO
Senescence_up
SASP
Apoptosis
Enrichment plot: Fridman_senescenceup.grp
Enrichment plot: SASP.grp
Enrichment plot: HALLMARK_APOPTOSIS
Het KO
Het KO
Het KO
I
Het
KO
vec
WT
101-692
AKAP95
GAPDH
SA-β-gal positive cells (%)
50
25
0
**
**
vec
WT
101-692
vec
WT
101-692
50 µm
J
Het
KO
MYC-Het
MYC-KO
Relative mRNA level
5
4
3
2
1
0
***
**
***
Akap95
Ccna2
K
Oncogenes (MYC)
Other genes
Transcription
AKAP95
Pre-mRNAs:
Splicing
mRNAs:
Proteins (Cyclin A2, SMAD6…)
Senescence
Cell growth
Cancer

Figure 3

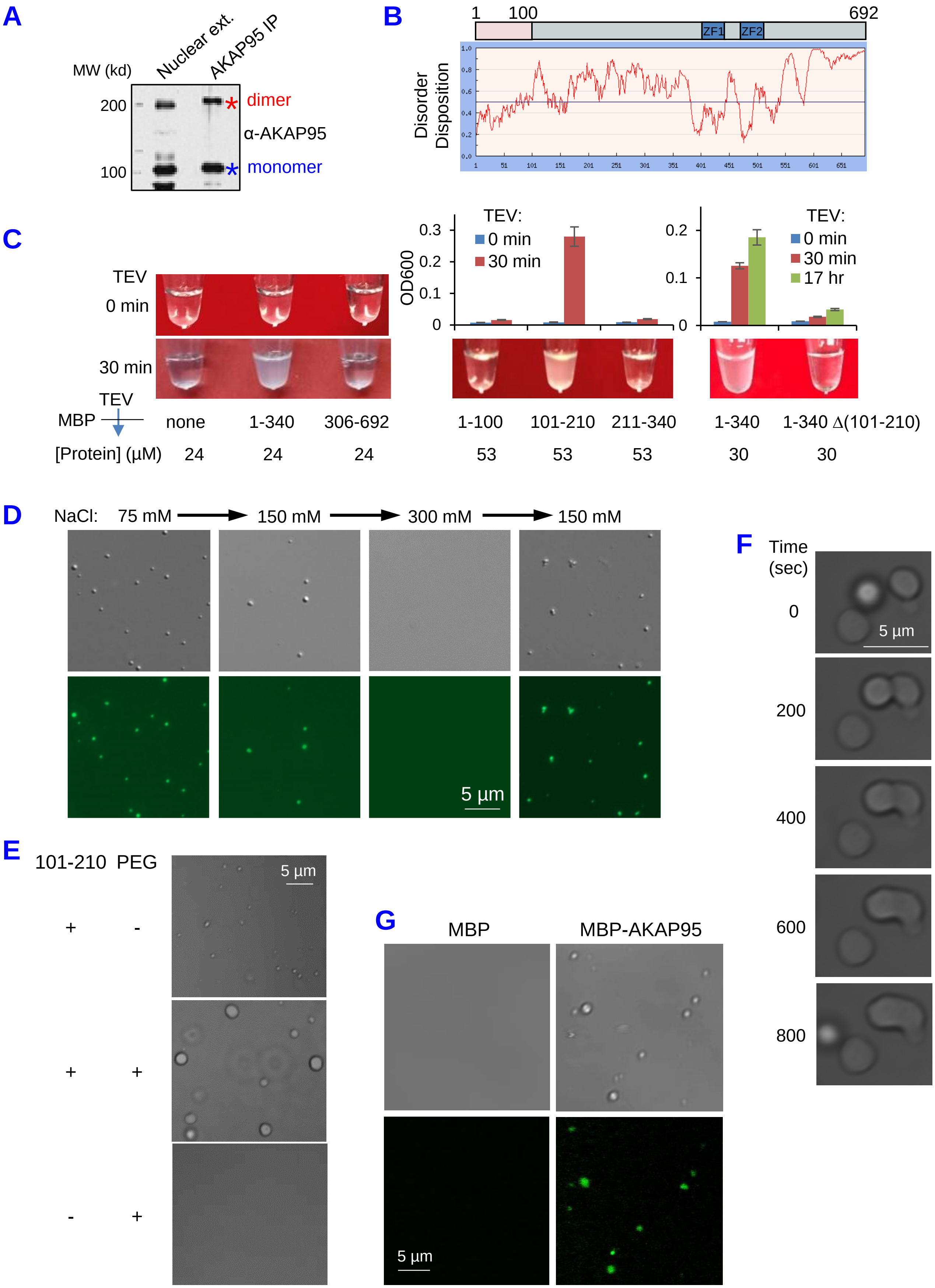
A
MW (kd)
Nuclear ext.
AKAP95 IP
200
100
* dimer
α-AKAP95
* monomer
B
1
100
692
ZF1
ZF2
Disorder Disposition
1.0
0.8
0.6
0.4
0.2
0.0
1
51
101
151
201
251
301
351
401
451
501
551
601
651
C
TEV
0 min
30 min
TEV
MBP
none
1-340
306-692
[Protein] (μM)
24
24
24
OD600
0.3
0.2
0.1
0
TEV:
🟦 0 min
🟥 30 min
1-100
101-210
211-340
53
53
53
0.2
0.1
0
TEV:
🟦 0 min
🟥 30 min
🟩 17 hr
1-340
1-340 Δ(101-210)
30
30
D
NaCl: 75 mM → 150 mM → 300 mM → 150 mM
5 μm
E
101-210 PEG
+ -
+ +
- +
5 μm
F
Time (sec)
0
200
400
600
800
5 μm
G
MBP
MBP-AKAP95
5 μm

Figure 4

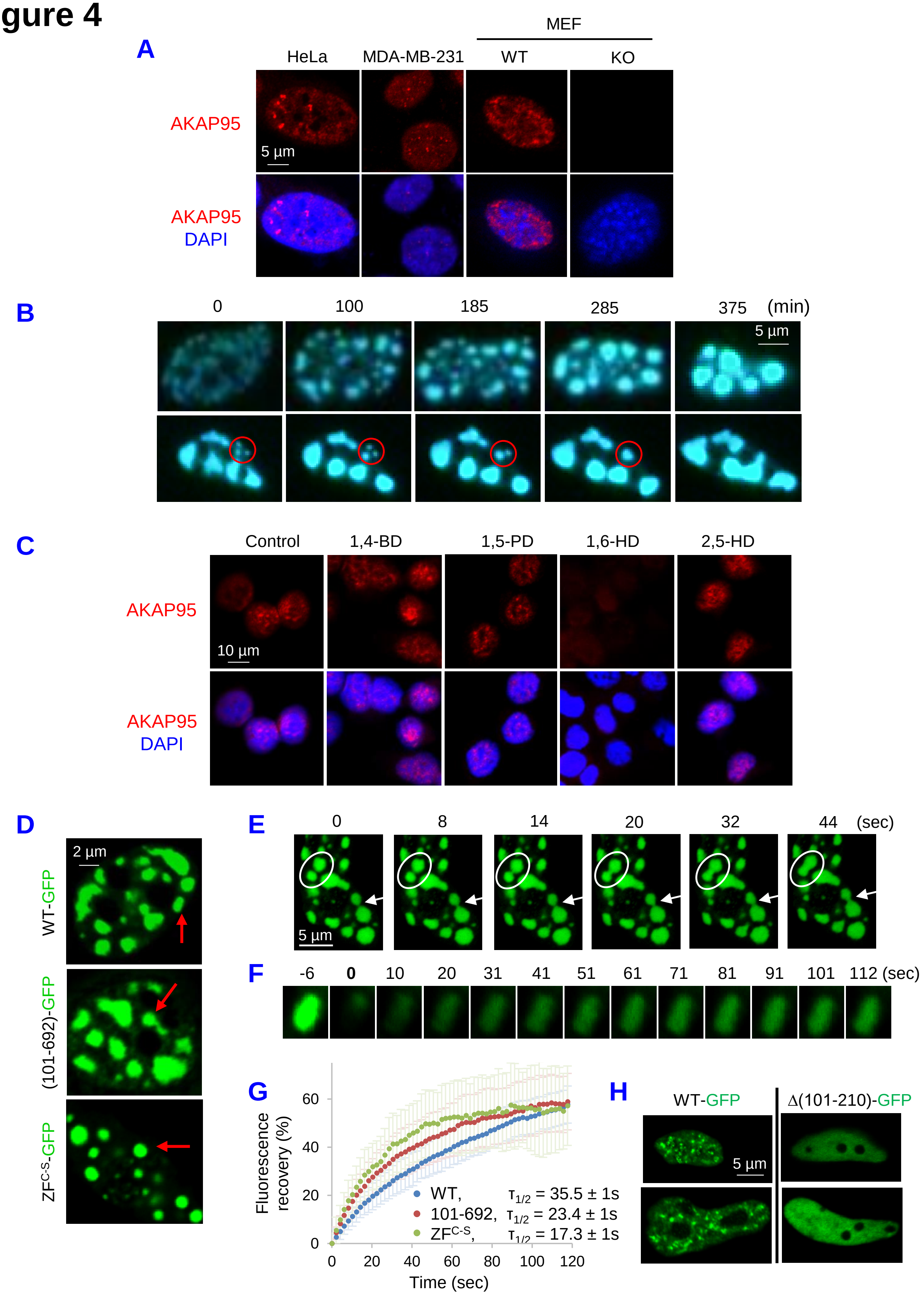
A
MEF
HeLa
MDA-MB-231
WT
KO
AKAP95
AKAP95
DAPI
5 µm
B
0
100
185
285
375 (min)
5 µm
C
Control
1,4-BD
1,5-PD
1,6-HD
2,5-HD
AKAP95
AKAP95
DAPI
10 µm
D
WT-GFP
(101-692)-GFP
ZF^{C-S}-GFP
2 µm
E
0
8
14
20
32
44 (sec)
5 µm
F
-6
0
10
20
31
41
51
61
71
81
91
101
112 (sec)
G
Fluorescence recovery (%)
Time (sec)
0
20
40
60
0
20
40
60
80
100
120
● WT, $\tau_{1/2}$ = 35.5 ± 1s
● 101-692, $\tau_{1/2}$ = 23.4 ± 1s
● ZF^{C-S}, $\tau_{1/2}$ = 17.3 ± 1s
H
WT-GFP
Δ(101-210)-GFP
5 µm

Figure 5

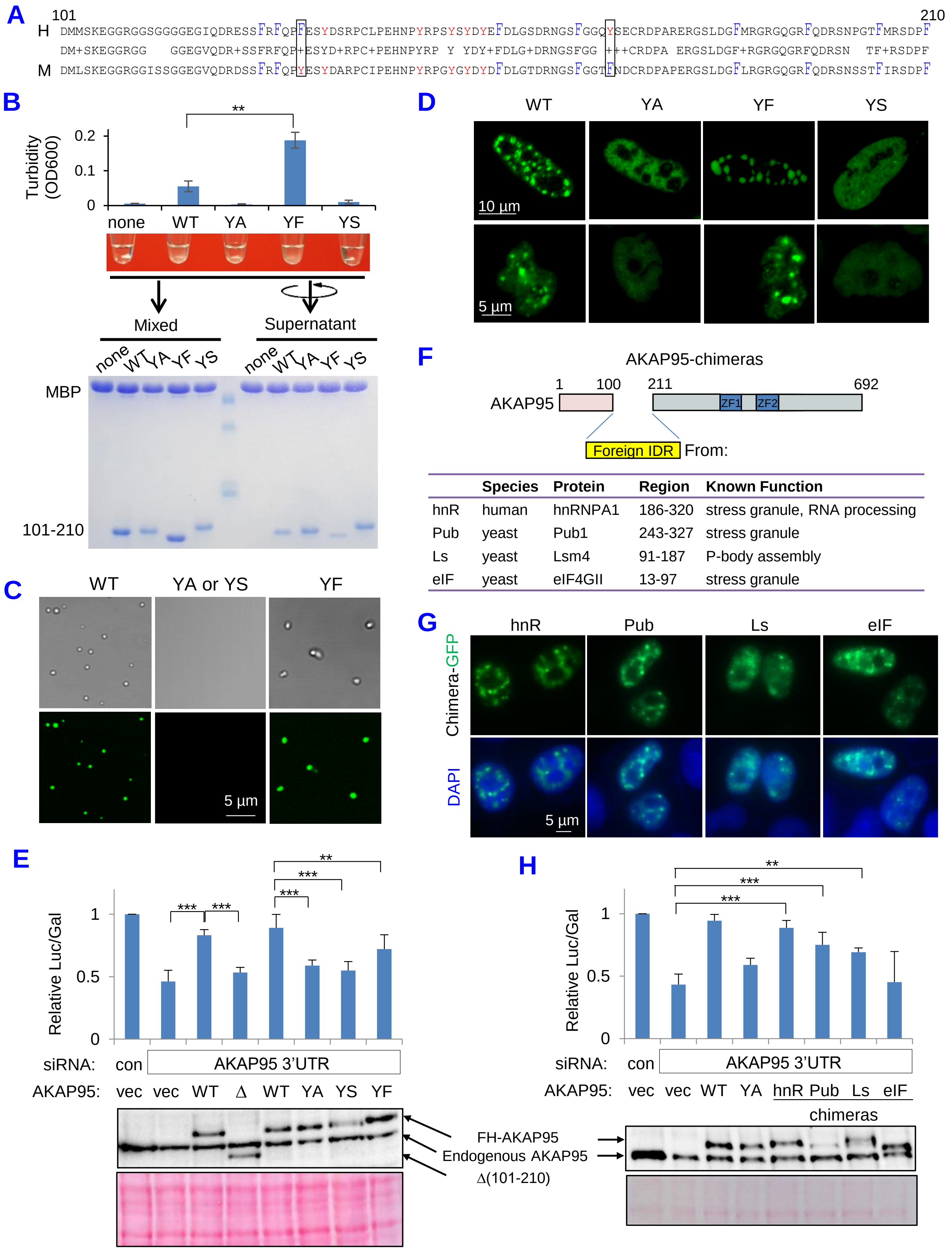

```
     101                                                                                                            210
H  DMMSKEGGRGGSGGGGEGIQDRESSFRFQPFESYDSRPCLPEHNPYRPSYSYDYEFDLGSDRNGSFGGQYSECRDPARERGSLDGFMRGRGQGRFQDRSNPGTFMRSDPF
   DM+SKEGGRGG   GGEGVQDR+SSFRFQP+ESYD+RPC+PEHNPYRP Y YDY+FDLG+DRNGSFGG +++CRDPA ERGSLDGF+RGRGQGRFQDRSN  TF+RSDPF
M  DMLSKEGGRGGISSGGEGVQDRDSSFRFQPYESYDARPCIPEHNPYRPGYGYDYDFDLGTDRNGSFGGTFNDCRDPAPERGSLDGFLRGRGQGRFQDRSNSSTFIRSDPF
```

	Species	Protein	Region	Known Function
hnR	human	hnRNPA1	186-320	stress granule, RNA processing
Pub	yeast	Pub1	243-327	stress granule
Ls	yeast	Lsm4	91-187	P-body assembly
eIF	yeast	eIF4GII	13-97	stress granule

Figure 6

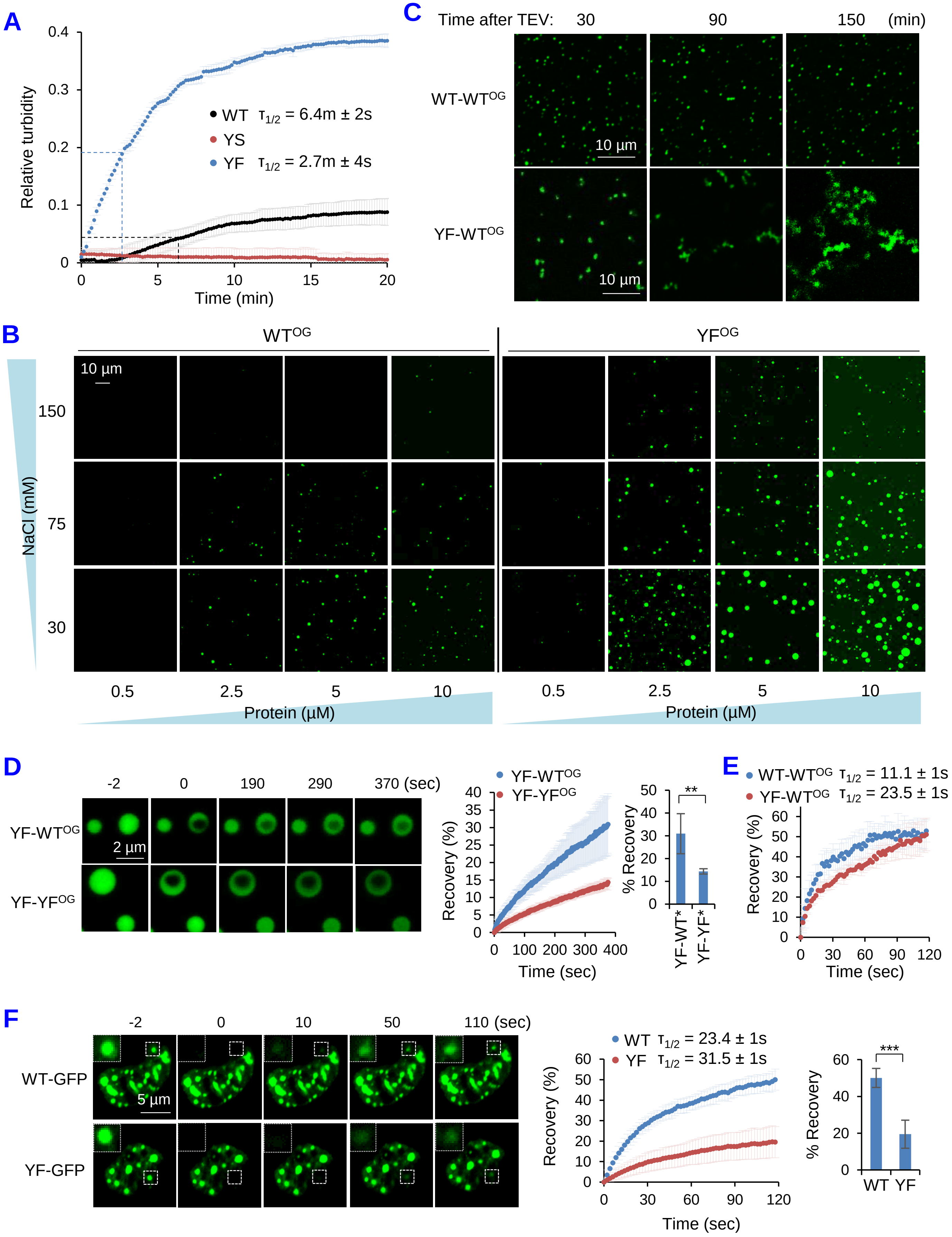
A
0.4
0.3
0.2
0.1
0
Relative turbidity
WT $\tau_{1/2}$ = 6.4m ± 2s
YS
YF $\tau_{1/2}$ = 2.7m ± 4s
0
5
10
15
20
Time (min)
C
Time after TEV: 30 90 150 (min)
WT-WT^{OG}
YF-WT^{OG}
10 µm
10 µm
B
WT^{OG}
YF^{OG}
10 µm
150
75
30
NaCl (mM)
0.5
2.5
5
10
Protein (µM)
0.5
2.5
5
10
Protein (µM)
D
-2
0
190
290
370 (sec)
YF-WT^{OG}
YF-YF^{OG}
2 µm
YF-WT^{OG}
YF-YF^{OG}
40
35
30
25
20
15
10
5
0
Recovery (%)
0
100
200
300
400
Time (sec)
50
40
30
20
10
0
% Recovery
**
YF-WT*
YF-YF*
E
WT-WT^{OG} $\tau_{1/2}$ = 11.1 ± 1s
YF-WT^{OG} $\tau_{1/2}$ = 23.5 ± 1s
60
50
40
30
20
10
0
Recovery (%)
0
30
60
90
120
Time (sec)
F
-2
0
10
50
110 (sec)
WT-GFP
YF-GFP
5 µm
WT $\tau_{1/2}$ = 23.4 ± 1s
YF $\tau_{1/2}$ = 31.5 ± 1s
60
50
40
30
20
10
0
Recovery (%)
0
30
60
90
120
Time (sec)
60
40
20
0
% Recovery
***
WT
YF

Figure 7

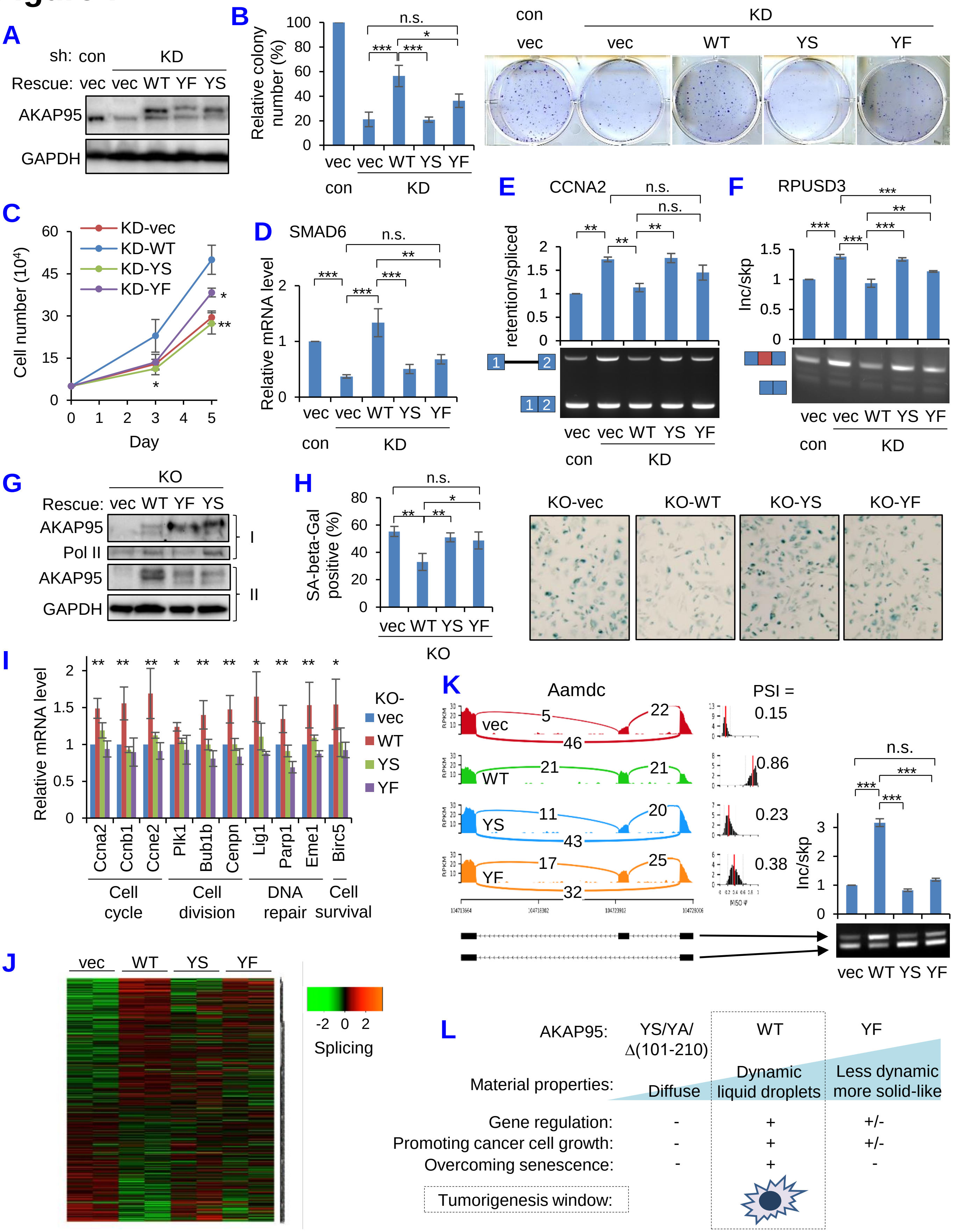
A
sh: con KD
Rescue: vec vec WT YF YS
AKAP95
GAPDH
B
Relative colony number (%)
100 80 60 40 20 0
n.s.
*
***
***
vec vec WT YS YF
con KD
con KD
vec vec WT YS YF
C
60 45 30 15 0
Cell number (10^4)
KD-vec
KD-WT
KD-YS
KD-YF
*
**
*
0 1 2 3 4 5
Day
D
SMAD6
n.s.
**
***
***
***
Relative mRNA level
2 1 0
vec vec WT YS YF
con KD
E
CCNA2
n.s.
n.s.
**
**
**
retention/spliced
2 1.5 1 0.5 0
1 2
1 2
vec vec WT YS YF
con KD
F
RPUSD3
***
**
***
***
***
Inc/skp
1.5 1 0.5 0
vec vec WT YS YF
con KD
G
KO
Rescue: vec WT YF YS
AKAP95
Pol II
AKAP95
GAPDH
I
II
H
n.s.
*
**
**
SA-beta-Gal positive (%)
80 60 40 20 0
vec WT YS YF
KO
KO-vec KO-WT KO-YS KO-YF
I
Relative mRNA level
2 1.5 1 0.5 0
** ** ** * ** ** * ** ** *
Ccna2 Ccnb1 Ccne2 Plk1 Bub1b Cenpn Lig1 Parp1 Eme1 Birc5
Cell cycle
Cell division
DNA repair
Cell survival
KO-
vec
WT
YS
YF
J
vec WT YS YF
-2 0 2
Splicing
K
Aamdc
PSI =
vec 5 22 46 0.15
WT 21 21 0.86
YS 11 20 43 0.23
YF 17 25 32 0.38
RPKM
MISO Ψ
n.s.
***
***
***
Inc/skp
3 2 1 0
vec WT YS YF
L
AKAP95: YS/YA/Δ(101-210) WT YF
Material properties: Diffuse | Dynamic liquid droplets | Less dynamic more solid-like
Gene regulation: - + +/-
Promoting cancer cell growth: - + +/-
Overcoming senescence: - + -
Tumorigenesis window:

Figure S1

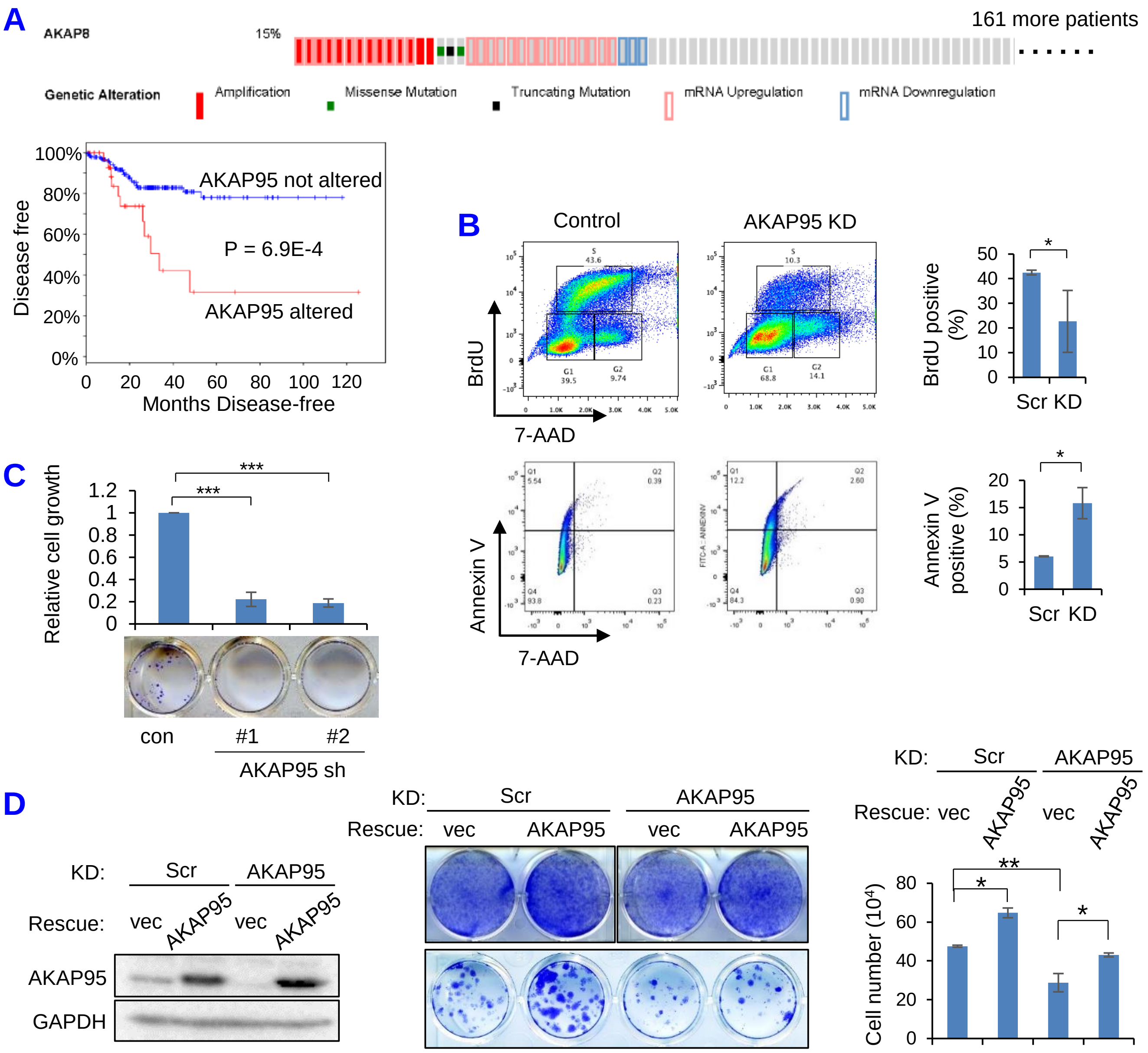

E

Enriched in genes down by KD

	GS follow link to MSigDB	NES	NOM p-val	FDR q-val
1	TGF_BETA_SIGNALING	1.71	0.002	0.041
2	G2M_CHECKPOINT	1.53	0.004	0.115
3	E2F_TARGETS	1.38	0.016	0.261
4	KRAS_SIGNALING_UP	1.36	0.022	0.229
5	IL2_STAT5_SIGNALING	1.36	0.019	0.186
6	HYPOXIA	1.33	0.024	0.196
7	HEDGEHOG_SIGNALING	1.29	0.140	0.227
8	GLYCOLYSIS	1.20	0.106	0.380
9	NOTCH_SIGNALING	1.13	0.292	0.538
10	ANDROGEN_RESPONSE	1.05	0.343	0.767

Enriched in genes up by KD

	GS follow link to MSigDB	NES	NOM p-val	FDR q-val
1	INFLAMMATORY_RESPONSE	-1.69	0.002	0.059
2	TNFA_SIGNALING_VIA_NFKB	-1.64	0.000	0.051
3	COMPLEMENT	-1.61	0.002	0.045
4	UV_RESPONSE_UP	-1.59	0.002	0.039
5	APOPTOSIS	-1.43	0.008	0.113
6	APICAL_SURFACE	-1.41	0.067	0.117
7	EPITHELIAL_MESENCHYMAL_TRANSITION	-1.40	0.006	0.109
8	P53_PATHWAY	-1.38	0.011	0.112
9	SPERMATOGENESIS	-1.37	0.056	0.111
10	COAGULATION	-1.33	0.059	0.136

Figure S1, continued 1

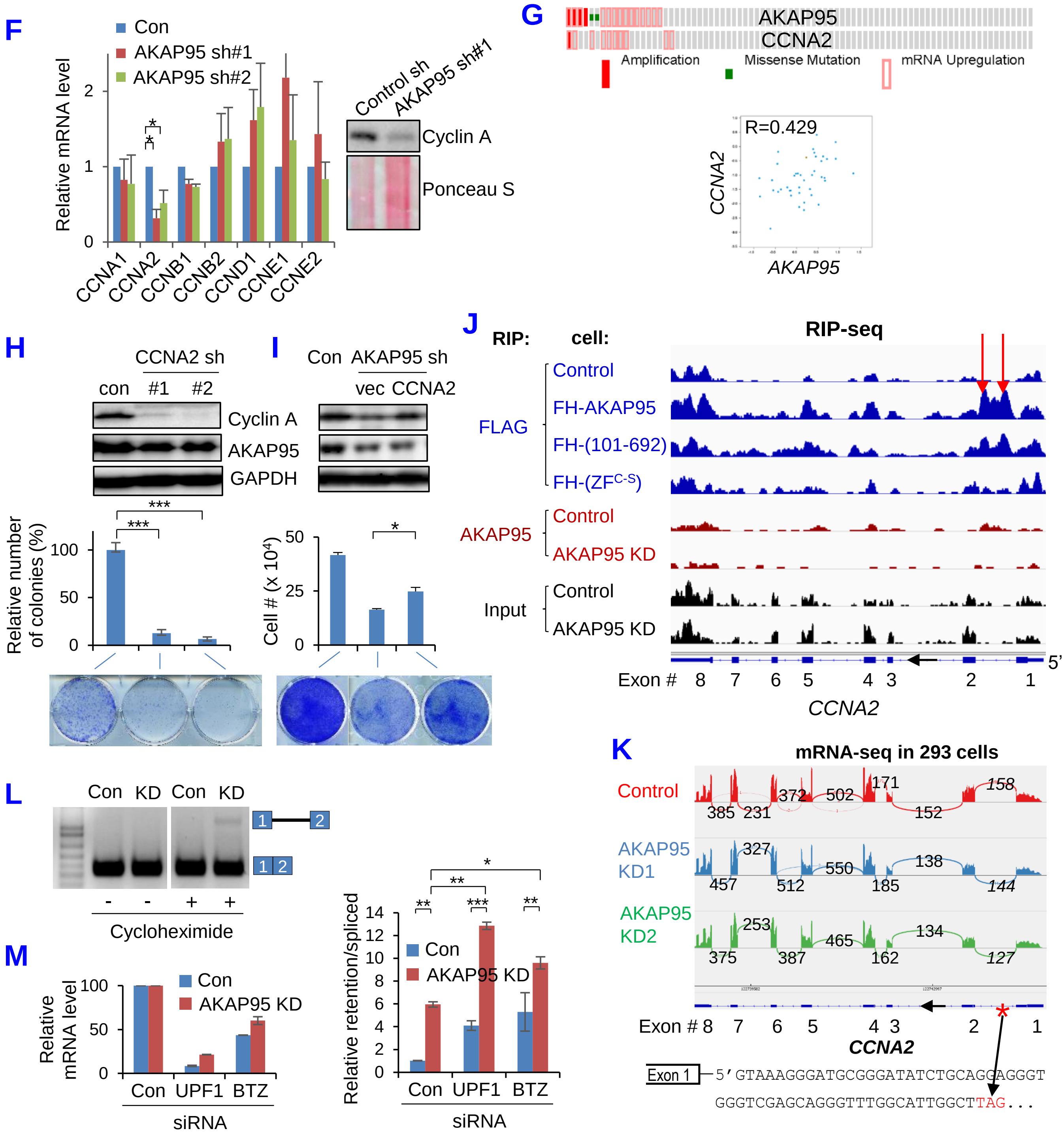

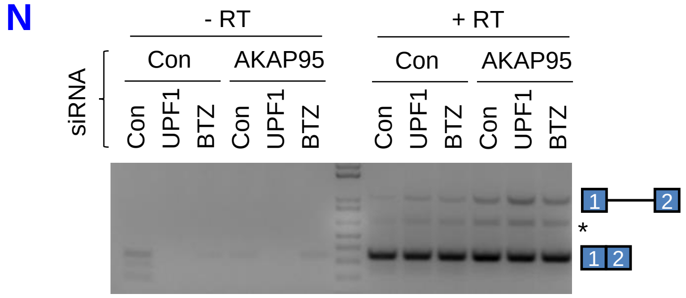

293 cells

	exon 1-2	Avg	**Exon 1-2/Avg**
Control	158	282	**0.56**
KD 1	144	330	**0.44**
KD 2	127	272	**0.47**

MDA-MB-231 cells

	exon 1-2	Avg	**Exon 1-2/Avg**
Control	435	400	**1.09**
KD	290	286	**1.01**

Figure S1, continued 2

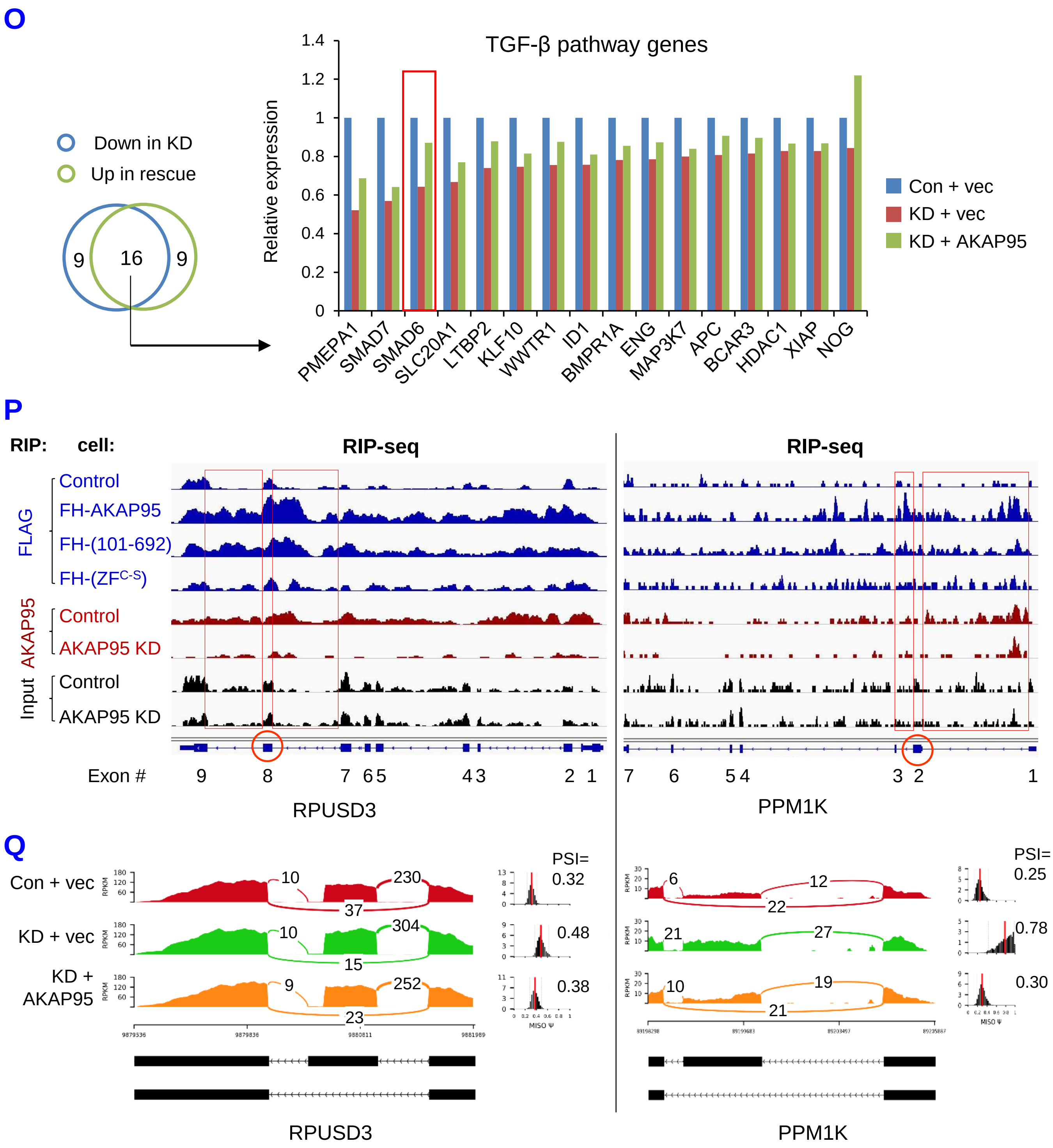

Figure S2

A

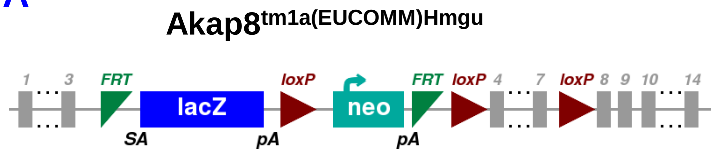

B

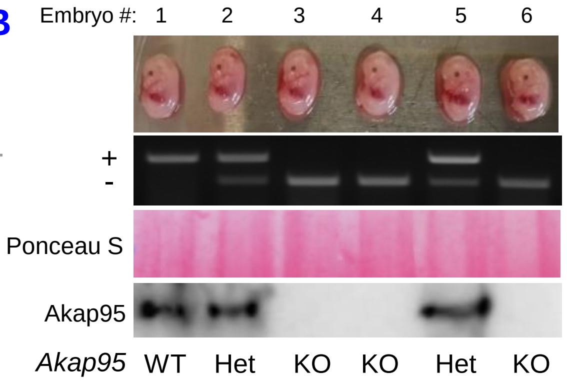

C

Enriched in genes down in KO

	GS follow link to MSigDB	NES	NOM p-val	FDR q-val
1	E2F_TARGETS	3.62	0.000	0.000
2	G2M_CHECKPOINT	3.33	0.000	0.000
3	MYC_TARGETS_V1	2.44	0.000	0.000
4	MITOTIC_SPINDLE	2.28	0.000	0.000
5	MYC_TARGETS_V2	2.23	0.000	0.000
6	SPERMATOGENESIS	1.52	0.013	0.015
7	DNA_REPAIR	1.32	0.033	0.068
8	MTORC1_SIGNALING	1.00	0.447	0.498
9	FATTY_ACID_METABOLISM	0.74	0.967	0.952

Enriched in genes up in KO

	GS follow link to MSigDB	NES	NOM p-val	FDR q-val
1	EPITHELIAL_MESENCHYMAL_TRANSITION	-3.25	0.000	0.000
2	TNFA_SIGNALING_VIA_NFKB	-2.94	0.000	0.000
3	COAGULATION	-2.81	0.000	0.000
4	HYPOXIA	-2.53	0.000	0.000
5	MYOGENESIS	-2.40	0.000	0.000
6	P53_PATHWAY	-2.36	0.000	0.000
7	INFLAMMATORY_RESPONSE	-2.27	0.000	0.000
8	APOPTOSIS	-2.23	0.000	0.000
9	IL6_JAK_STAT3_SIGNALING	-2.22	0.000	0.000
10	INTERFERON_GAMMA_RESPONSE	-2.01	0.000	0.000

D

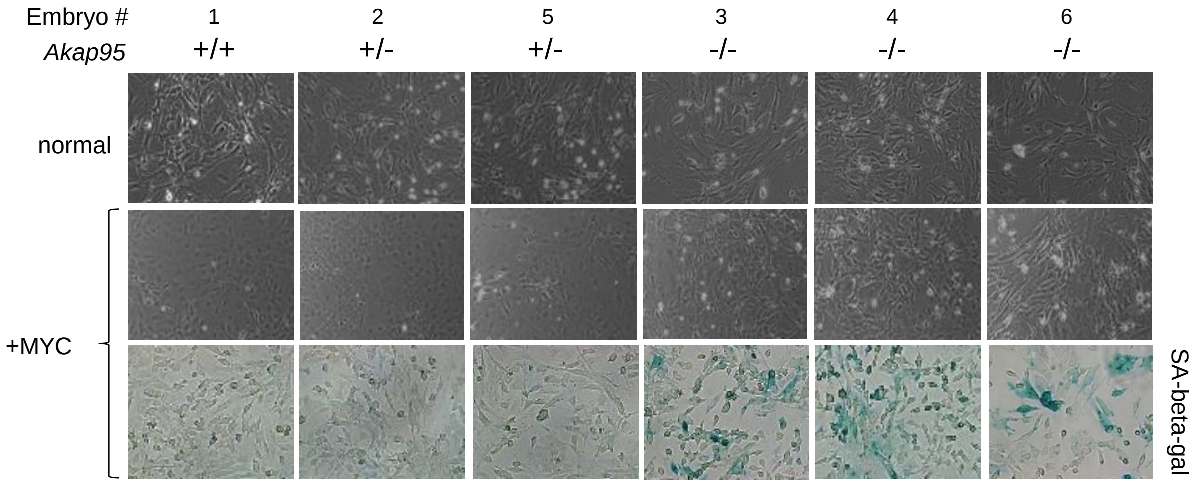

E

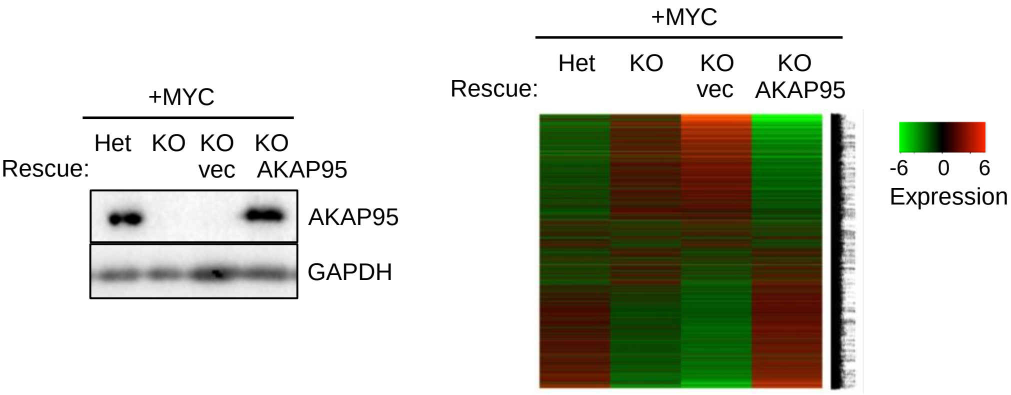

Figure S2, continued

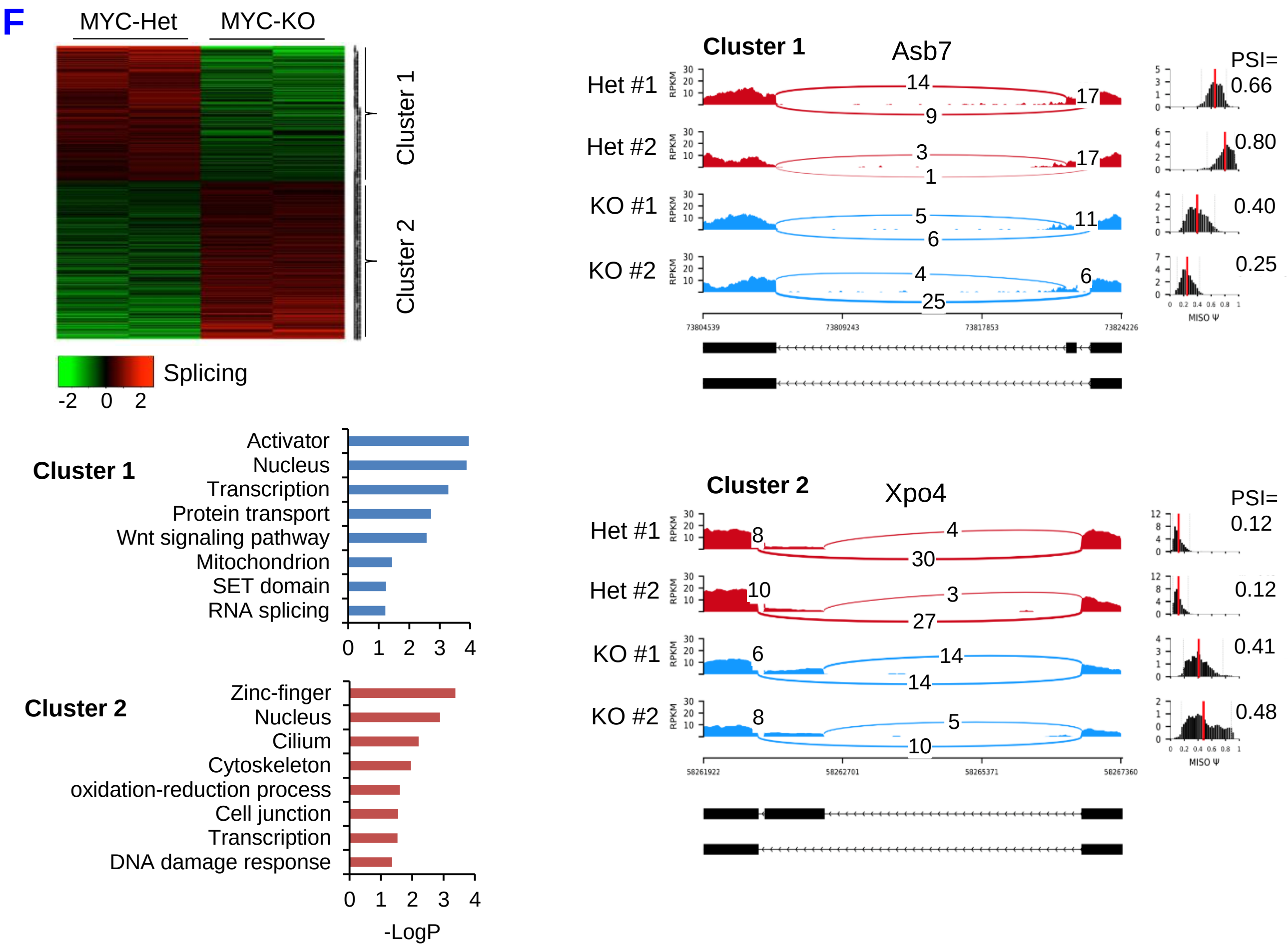

Figure S3

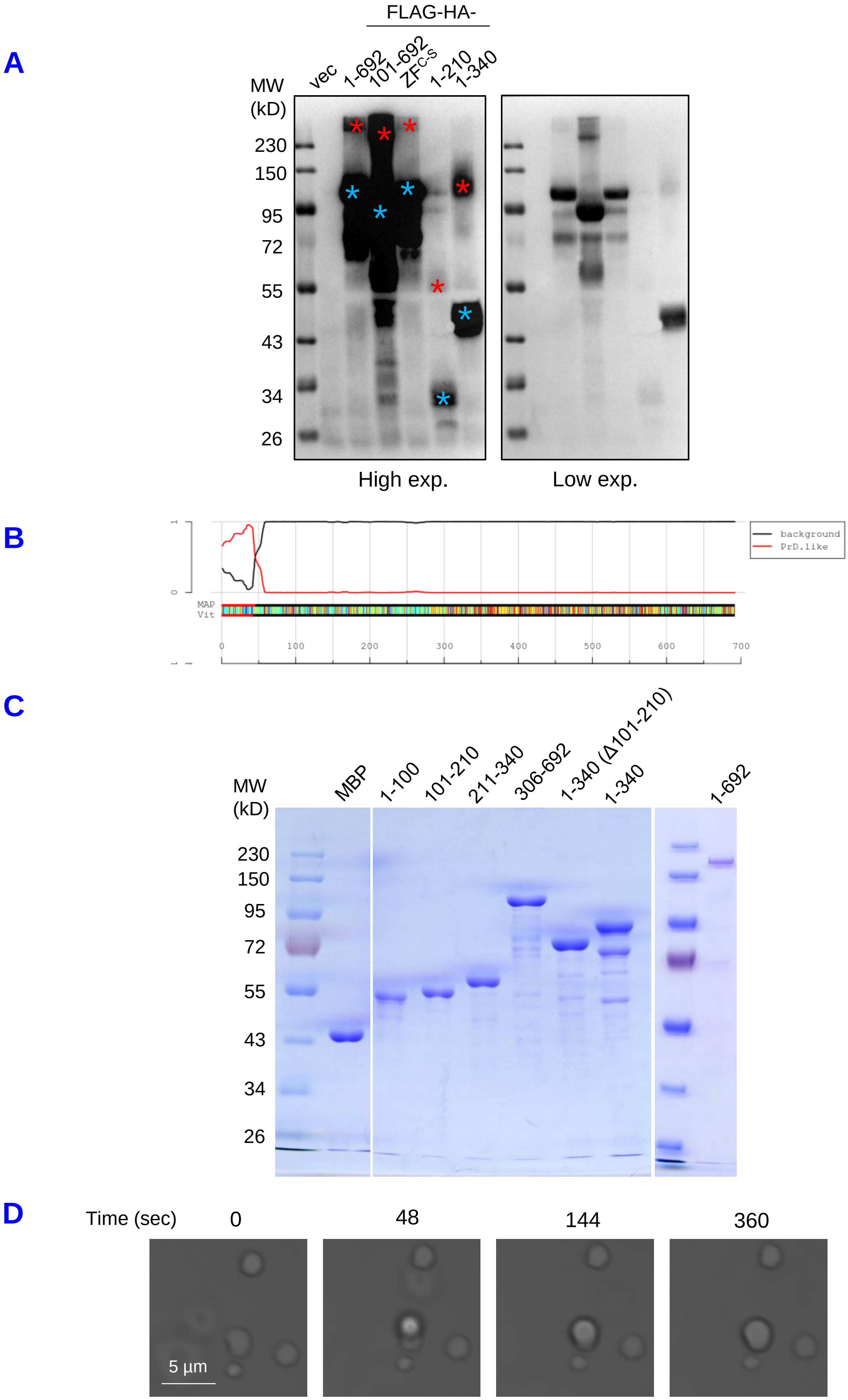
A
FLAG-HA-
vec
1-692
101-692
ZF C-S
1-210
1-340
MW
(kD)
230
150
95
72
55
43
34
26
High exp.
Low exp.
B
1
0
background
PrD.like
MAP
Vit
0
100
200
300
400
500
600
700
C
MW
(kD)
MBP
1-100
101-210
211-340
306-692
1-340 (Δ101-210)
1-340
1-692
230
150
95
72
55
43
34
26
D
Time (sec)
0
48
144
360
5 µm

Figure S4

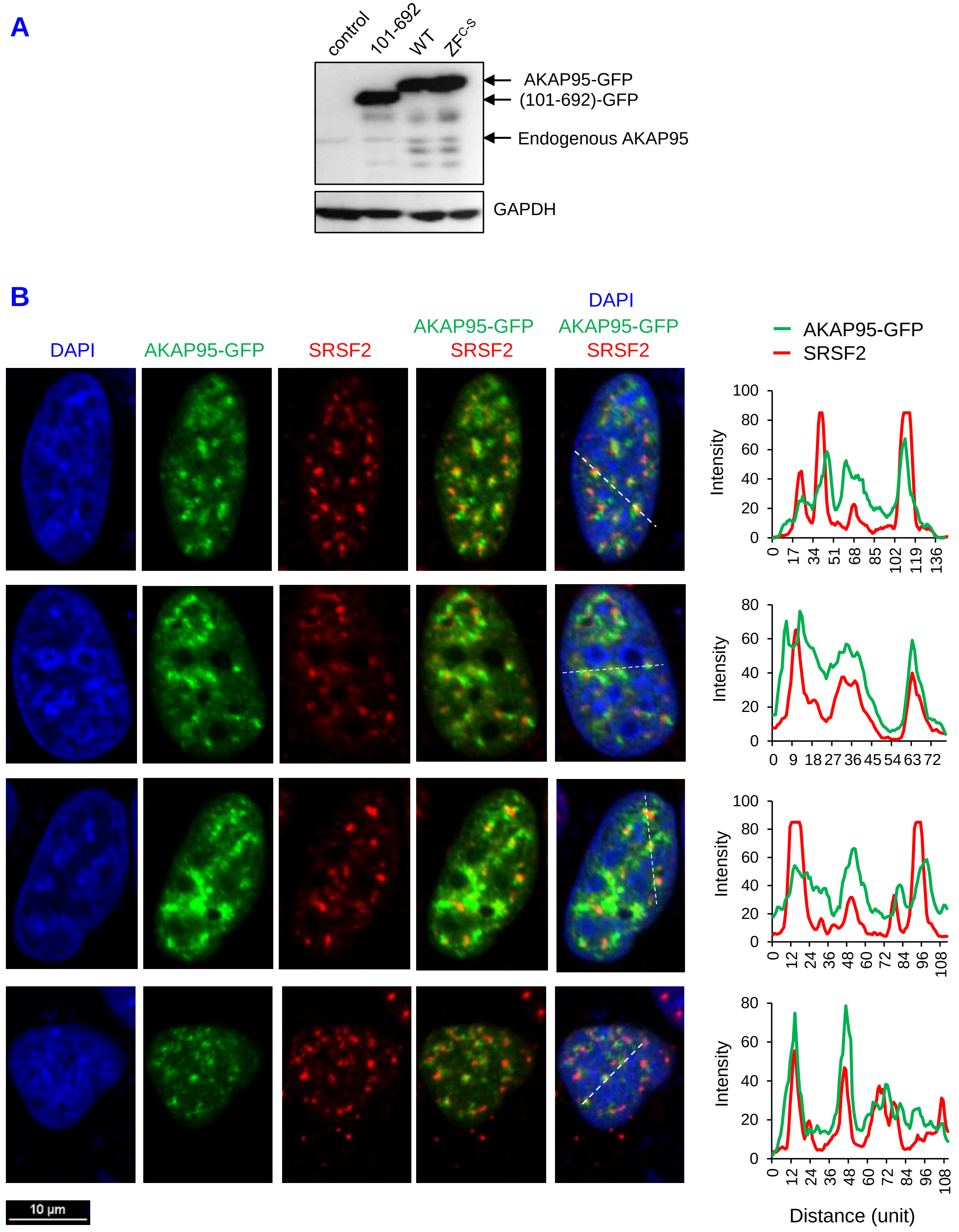
A
control
101-692
WT
ZF^{C-S}
AKAP95-GFP
(101-692)-GFP
Endogenous AKAP95
GAPDH
B
DAPI
AKAP95-GFP
SRSF2
AKAP95-GFP SRSF2
DAPI AKAP95-GFP SRSF2
AKAP95-GFP
SRSF2
Intensity
0 20 40 60 80 100
0 17 34 51 68 85 102 119 136
Intensity
0 20 40 60 80
0 9 18 27 36 45 54 63 72
Intensity
0 20 40 60 80 100
0 12 24 36 48 60 72 84 96 108
Intensity
0 20 40 60 80
0 12 24 36 48 60 72 84 96 108
Distance (unit)
10 μm

Figure S5

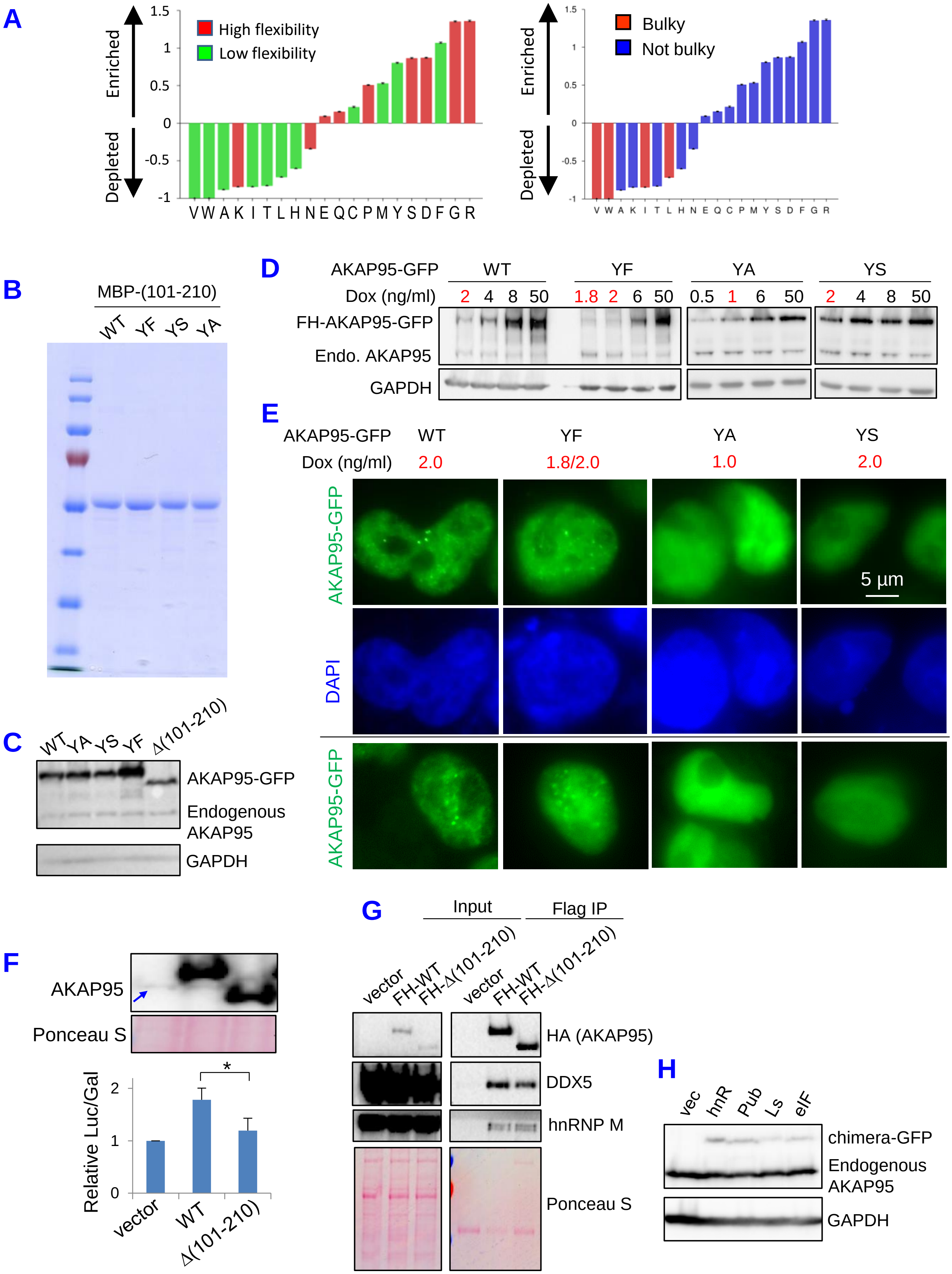
A
Enriched
Depleted
1.5
1
0.5
0
-0.5
-1
🟥 High flexibility
🟩 Low flexibility
V W A K I T L H N E Q C P M Y S D F G R
🟥 Bulky
🟦 Not bulky
B
MBP-(101-210)
WT
YF
YS
YA
C
WT
YA
YS
YF
Δ(101-210)
AKAP95-GFP
Endogenous AKAP95
GAPDH
D
AKAP95-GFP
WT
YF
YA
YS
Dox (ng/ml)
2 4 8 50
1.8 2 6 50
0.5 1 6 50
2 4 8 50
FH-AKAP95-GFP
Endo. AKAP95
GAPDH
E
AKAP95-GFP
WT
YF
YA
YS
Dox (ng/ml)
2.0
1.8/2.0
1.0
2.0
AKAP95-GFP
DAPI
AKAP95-GFP
5 µm
F
AKAP95
Ponceau S
Relative Luc/Gal
2
1
0
*
vector
WT
Δ(101-210)
G
Input
Flag IP
vector
FH-WT
FH-Δ(101-210)
vector
FH-WT
FH-Δ(101-210)
HA (AKAP95)
DDX5
hnRNP M
Ponceau S
H
vec
hnR
Pub
Ls
eIF
chimera-GFP
Endogenous AKAP95
GAPDH

Figure S6

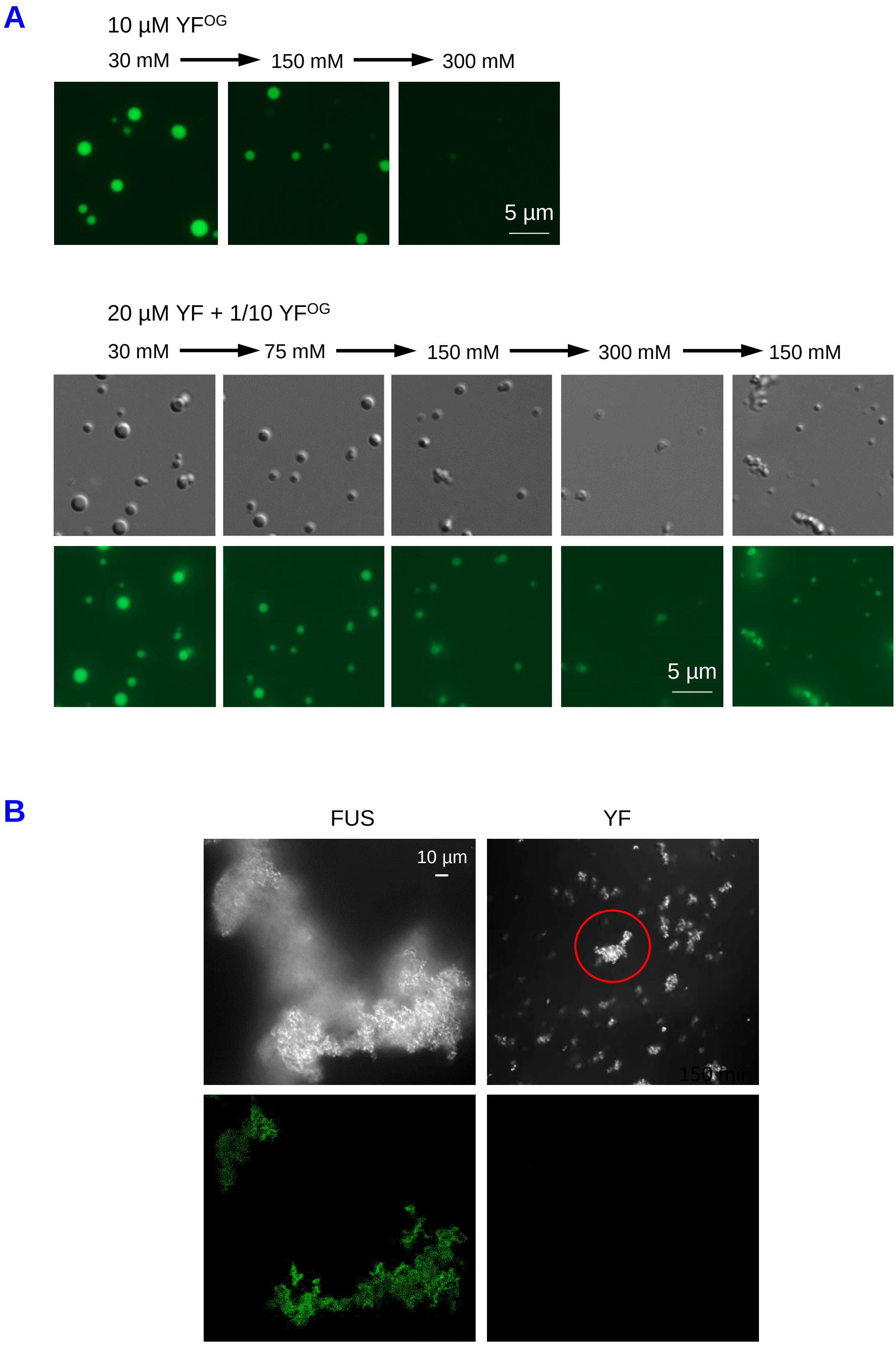
A
10 µM YF^OG
30 mM
150 mM
300 mM
5 µm
20 µM YF + 1/10 YF^OG
30 mM
75 mM
150 mM
300 mM
150 mM
5 µm
B
FUS
YF
10 µm
150 min

Figure S7

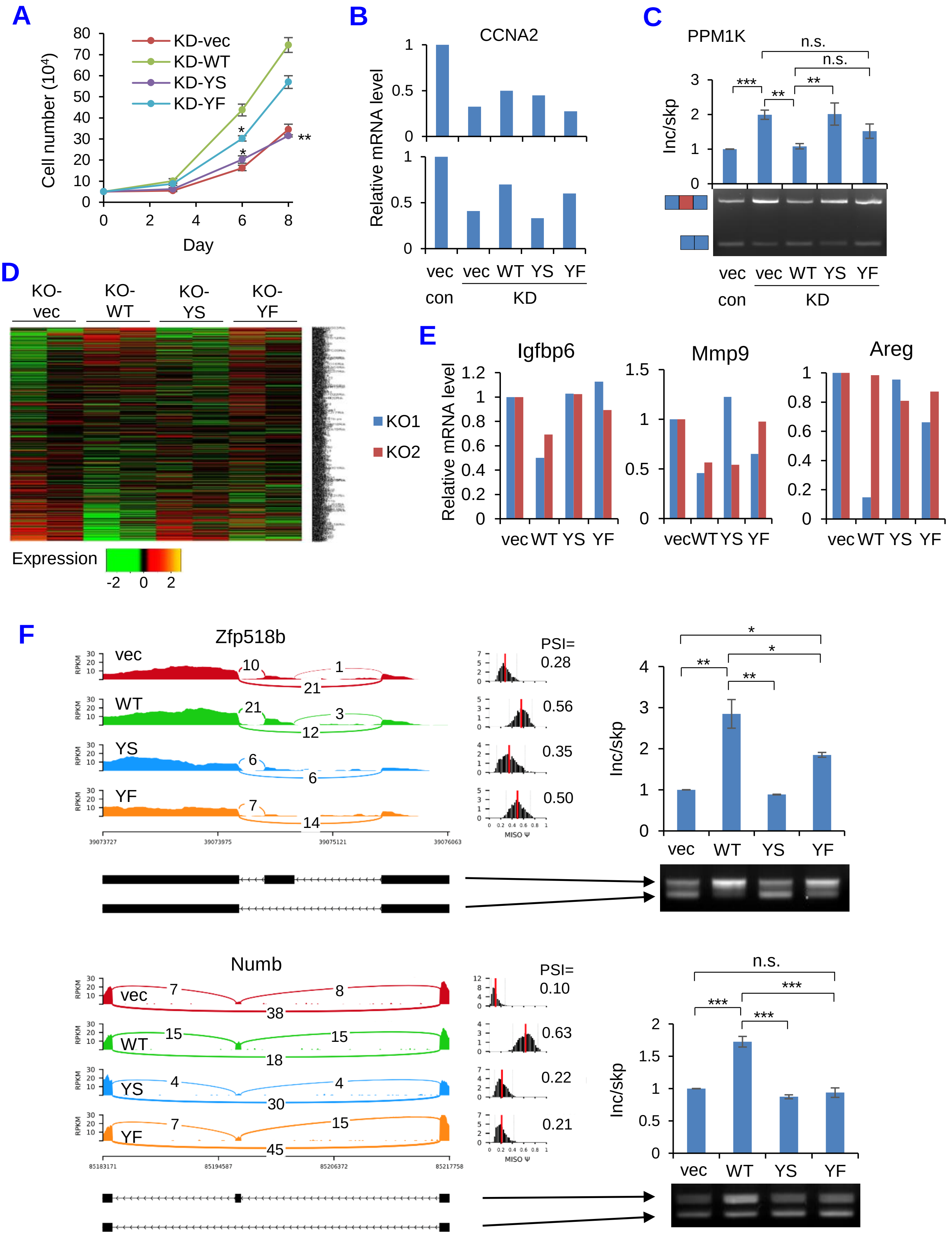
A
Cell number (10⁴)
Day
KD-vec
KD-WT
KD-YS
KD-YF
*
*
**
B
CCNA2
Relative mRNA level
vec
con
vec WT YS YF
KD
C
PPM1K
Inc/skp
n.s.
n.s.
***
**
**
vec
con
vec WT YS YF
KD
D
KO-vec
KO-WT
KO-YS
KO-YF
Expression
-2 0 2
E
Igfbp6
Mmp9
Areg
Relative mRNA level
KO1
KO2
vec WT YS YF
F
Zfp518b
vec
WT
YS
YF
RPKM
PSI=
0.28
0.56
0.35
0.50
MISO Ψ
39073727
39073975
39075121
39076063
Inc/skp
*
*
**
**
vec WT YS YF
Numb
PSI=
0.10
0.63
0.22
0.21
85183171
85194587
85206372
85217758
n.s.
***
***
***
Inc/skp
vec WT YS YF

Figure S7, continued